

POLITECNICO DI MILANO

*Department Of Electronics, Information and Bioengineering*

Master of Science in Biomedical Engineering



# DESIGN AND DEVELOPMENT OF AN ELECTRONIC CIRCUIT FOR A SENSORY-FEEDBACK LOWER-LIMB NEUROPROSTHESIS

Supervisor: Prof.ssa Alessandra Laura Giulia PEDROCCHI, Politecnico di Milano

Co-supervisor: Prof. Stanisa RASPOPOVIC, ETH Zürich

Tutor: Dr. Giacomo VALLE, ETH Zürich

Dr. Francesco Maria PETRINI, ETH Zürich

Candidate:

Chiara BASLA

Identification number: 916221

Academic Year 2019-2020



*I would like to thank Professor Alessandra Pedrocchi for making this experience possible and for her guidance; Professor Stanisa Raspopovic, Dr. Giacomo Valle and Dr. Francesco Petrini for having supervised me in these months with many teachings, useful advice and having increased my knowledge and interest in the research field. I would like to also thank my family and Michele for always believing in me and for all their support and Francesca and Silvia for always being very close to me.*



---

# Contents

---

<b>List of Figures</b>	<b>iii</b>
<b>List of Tables</b>	<b>vii</b>
<b>Acronyms</b>	<b>x</b>
<b>Glossary</b>	<b>xi</b>
<b>Abstract</b>	<b>xiii</b>
<b>Sommario</b>	<b>xxiii</b>
<b>1 Introduction</b>	<b>1</b>
1.1 Lower limb amputation . . . . .	1
1.2 Transfemoral amputation . . . . .	2
1.3 Peripheral Neuropathy . . . . .	3
1.4 Sensory Feedback restoration . . . . .	3
<b>2 MYLEG device</b>	<b>7</b>
2.1 Novelties . . . . .	10
2.2 Achievements . . . . .	11
2.3 Aim of the thesis . . . . .	11
<b>3 Materials and Methods</b>	<b>13</b>
3.1 Hardware design . . . . .	13
3.1.1 Power line . . . . .	14
3.1.2 Analog circuit . . . . .	19
3.1.3 Inertial Measurement Unit . . . . .	22
3.1.4 Bluetooth module . . . . .	24
3.1.5 Microcontroller . . . . .	26
3.2 PCB design . . . . .	27
3.3 Extra IMU . . . . .	31
3.3.1 Knee angle algorithm . . . . .	36

---

3.4	Reprogramming . . . . .	40
3.5	Synchronisation . . . . .	41
3.6	Software implementation . . . . .	48
<b>4</b>	<b>Validation</b>	<b>51</b>
4.1	Assessment of MYLEG functioning . . . . .	52
4.2	Assessment of MYLEG repeatability . . . . .	54
4.3	Assessment of MYLEG accuracy . . . . .	55
4.3.1	Comparison with the original board . . . . .	58
4.3.2	Two IMUs angle estimation . . . . .	61
4.3.3	Accuracy of the entire system . . . . .	63
<b>5</b>	<b>Exploitation</b>	<b>73</b>
<b>6</b>	<b>Conclusions</b>	<b>77</b>
	<b>Appendix A PCB schematic</b>	<b>81</b>
	<b>Appendix B Bill of materials</b>	<b>95</b>
B.1	Ankle box . . . . .	96
B.2	Thigh box . . . . .	97
	<b>Appendix C Technical Checklist</b>	<b>98</b>
C.1	General Safety Measures . . . . .	99
C.2	Requirements Related to Energy Storage and Electric Components . .	100
C.3	Requirements Related to Start-up and Shut-down . . . . .	101
C.4	Requirements Related to the Device Shape . . . . .	102
	<b>Appendix D Risk analysis</b>	<b>103</b>
	<b>Appendix E Firmware flowchart</b>	<b>107</b>
	<b>Bibliography</b>	<b>109</b>

---

# List of Figures

---

1	Global description of the MYLEG system used with a transfemoral amputee . . . . .	xv
2	Simplified schematic of the electronic circuits for data acquisition and transmission . .	xvi
3	(a) top and (b) bottom layers of the designed PCB for data acquisition and transmission	xvii
4	(a) knee angle algorithm; (b) shank and thigh angle calculated by the boards; (c) complementary filter formulas; (d) complementary filter schematic . . . . .	xviii
5	(a) Knee angle comparison between the data obtained using a gold standard 3D capture motion system (blue line) and the MYLEG device (red line) at 4 different velocities (100 % corresponds to the subject's self-selected comfortable walking speed); (b) knee angle comparison between the data obtained using a gold standard 3D capture motion system (blue line) and the MYLEG device (red line) at 3 different inclinations (0 % = ground level walking, + 15 % = inclined walking, - 15 % = declined walking); (c) force distribution comparison between the data obtained using force plates (blue line) and the MYLEG device (red line) at 3 different inclinations (0 % = ground level walking, + 15 % = inclined walking, - 15 % = declined walking). . . . .	xx
6	Descrizione generale del dispositivo MYLEG . . . . .	xxv
7	Schematico semplificato dei circuiti elettronici per l'acquisizione e la trasmissione di dati	xxvi
8	(a) layer superiore ed (b) inferiore del circuito stampato per l'acquisizione e la trasmissione dei dati . . . . .	xxvii
9	(a) algoritmo per il calcolo dell'angolo del ginocchio; (b) angolo della gamba e della coscia calcolati delle schede elettroniche; (c) formule per il calcolo dell'angolo del ginocchio; (d) filtro complementare . . . . .	xxviii
10	(a) Confronto dell'angolo del ginocchio tra l'andamento calcolato con un sistemi di acquisizione del movimento (linea blu) e quello stimato dal sistema MYLEG (linea rossa) a 4 diverse velocità (100 % corrisponde alla velocità di deambulazione scelta dal soggetto); (b) confronto dell'angolo del ginocchio tra l'andamento calcolato con un sistemi di acquisizione del movimento (linea blu) e quello stimato dal sistema MYLEG (linea rossa) a 3 diverse inclinazioni (0 % = piano, + 15 % = salita, - 15 % = discesa); (c) confronto della distribuzione delle forze tra l'andamento calcolato con piattaforme di forza (linea blu) e quello stimato dal sistema MYLEG (linea rossa) a 3 diverse inclinazioni (0 % = piano, + 15 % = salita, - 15 % = discesa). . . . .	xxxii
1.1	Principle of working of a neuroprosthesis for sensory-feedback restoration with invasive approach [1] . . . . .	4
2.1	Global description of the MYLEG system . . . . .	8
2.2	Remapped sensation at the amputee's stump . . . . .	9
2.3	Linear mapping between force and stimulation's intensity . . . . .	10
3.1	Simplified schematic of the electronic circuit for data acquisition and transmission . .	13
3.2	MCP73871 Li-Polymer Battery Charge Management Controller schematic . . . . .	15

---

3.3	LF33CPT-TR Voltage Regulator schematic . . . . .	17
3.4	(a) analog circuit present in the original board; (b) new circuit designed on the PCB . . . . .	19
3.5	Performance comparison between the original analog circuit (blue line) and the one obtained by reducing the input voltage but keeping the same values for $R_C$ and $V_B$ (red line) . . . . .	20
3.6	Performance comparison between the original analog circuit (blue line) and those obtained by keeping $R_C = 47 \text{ k}\Omega$ and decreasing $V_B$ . . . . .	21
3.7	LSM9DS1 Inertial Measurement Unit schematic . . . . .	23
3.8	RN4678-V/RM100 Bluetooth Dual Mode Module schematic . . . . .	26
3.9	STM32F103RBT6 medium-density performance line ARM-based MCU schematic . . . . .	27
3.10	(a) top and (b) bottom layers of the designed PCB for data acquisition and transmission . . . . .	28
3.11	(a) top and (b) bottom GND planes . . . . .	29
3.12	(a) top and (b) bottom traces, pads and vias . . . . .	30
3.13	(a) 3D printed case and (b) cover designed in SOLIDWORKS to accommodate the electronic board . . . . .	31
3.14	Angle measured by the original board while performing different activities . . . . .	32
3.15	Updated description of the MYLEG system after introducing a new electronic circuit at the thigh level . . . . .	33
3.16	Updated schematic after introducing a new IMU on the thigh of the patient for a more accurate estimate of the knee angle . . . . .	33
3.17	(a) top and (b) bottom thigh PCB . . . . .	34
3.18	2.4 GHz Transceiver Breakout - nRF24L01+ from Sparkfun . . . . .	34
3.19	2.4 GHz Transceiver Breakout - nRF24L01+ schematic . . . . .	35
3.20	Correct positioning of the electronic boards around the patient's leg . . . . .	37
3.21	(a) knee angle algorithm; (b) shank and thigh angle calculated by the boards; (c) complementary filter . . . . .	38
3.22	(a) original board reprogramming method; (b) new reprogramming method through externally accessible pins . . . . .	41
3.23	On-purpose made cable to connect the PCB to the ST-LINK programmer . . . . .	42
3.24	Different methods of wireless synchronization: (a) unidirectional broadcast; (b) sender-to-receiver broadcast; (c) receiver-to-receiver broadcast . . . . .	44
3.25	(a) synchronization circuit in microcontroller schematic; (b) synchronization pin schematic . . . . .	45
3.26	On-purpose made cable for synchronizing two devices. (a) when the synchronization pins are connected they are pulled High; (b) when the black cable is connected to GND they are pulled Low. . . . .	45
3.27	Data post-processing for synchronization of multiple devices . . . . .	46
3.28	Data post-processing for removing the delay accumulated over time; (a) raw force data as acquired by the electronic boards; (b) linear trend of the accumulated delay; (c) force data after removing the calculated offset . . . . .	47
4.1	(a) Knee angle, (b) force distribution and (c) corresponding stimulation calculated by MYLEG system during one entire walking cycle . . . . .	52
4.2	Collected data when moving the electronic board (a) along the y-axis, (b) around the z-axis and (c) pressing one force sensor of the sensorized insole . . . . .	54
4.3	Assessment of IMU repeatability moving the electronic board between two known points . . . . .	55
4.4	Assessment of IMU repeatability at 3 different velocities using the complementary filter coefficient of the original board . . . . .	56
4.5	Assessment of IMU repeatability at 3 different velocities after increasing the complementary filter coefficient to remove the excessive noise . . . . .	56
4.6	Percentage error in angle estimation while assessing repeatability . . . . .	57
4.7	Comparison between motion capture system measured and MYLEG system estimated trends for (a) knee angle and (b) force distribution. Graphical representation of the parameters used for validation. . . . .	58
4.8	Comparison of the new MYLEG system and the original board in estimating the shank angle: experimental setup . . . . .	59

---



---

4.9	Schematic of the circuit implemented on ODR0ID-C2 to synchronize the real trend from a motion capture system with the collected data from MYLEG system . . . . .	59
4.10	Comparison of the shank angle estimation between a motion capture system (blue line), the new MYLEG system (yellow line) and the original board (green line). . . . .	60
4.11	Daily-activities in which the presence of the thigh IMU removes (a) false negatives (the patient is not stimulated even if the knee angle is changing) and (b) false positive (the patient is stimulated although his knee is straight). The green line is considered representative of the behaviour of the original circuit while the blue line represents the angle calculated by the new MYLEG system. . . . .	62
4.12	(a) comparison of the knee (red line) and shank (green line) angles estimated by MYLEG system with the knee flexion recorded by a 3D motion capture system (blue line); (b) increased trend reliability of the knee angle with compared to the shank one . . .	63
4.13	Experimental setup . . . . .	64
4.14	Vicon Plug-In Gait marker configuration for calculating lower limb joint kinematics and kinetics . . . . .	64
4.15	Comparison between the data obtained using a gold standard 3D capture motion system integrated with force plates (blue line) and the MYLEG device (red line) both for the knee angle and the force distribution over 5 steps . . . . .	65
4.16	(a) Knee angle comparison between the data obtained using a gold standard 3D capture motion system (blue line) and the MYLEG device (red line) during comfortable walking; (b) amplitude difference and (c) trend reliability during self-selected speed walking . .	66
4.17	(a) Force distribution comparison between the data obtained using force plates (blue line) and the MYLEG device (red line) during comfortable walking, (b) time difference between peaks and (c) difference in peaks' amplitude ratio during self-selected speed walking . . . . .	68
4.18	(a) Knee angle comparison between the data obtained using a gold standard 3D capture motion system (blue line) and the MYLEG device (red line) at 4 different velocities (100 % corresponds to the subject's self-selected comfortable walking speed); (b) amplitude difference between the peaks of the two trends at different velocities; (c - d) trend reliability between knee angle data at different velocities during the entire walking cycle and the swing phase respectively. . . . .	69
4.19	(a) Knee angle comparison between the data obtained using a gold standard 3D capture motion system (blue line) and the MYLEG device (red line) at 3 different inclinations (0 % = ground level walking, + 15 % = inclined walking, - 15 % = declined walking); (b) trend reliability between the knee angle data at different inclinations during the swing phase; (c) amplitude difference of the overall trends at different inclinations. . .	70
4.20	(a) Force distribution comparison between the data obtained using force plates (blue line) and the MYLEG device (red line) at 3 different inclinations (0 % = ground level walking, + 15 % = inclined walking, - 15 % = declined walking); (b) difference in the peaks' ratio between knee angle trends at different inclinations; (c) time difference between the peaks at different inclinations. . . . .	71
4.21	(a) Synchronization process between 3D motion capture system and MYLEG system; (b) time delay between the knee angle data obtained using a gold standard 3D capture motion system and the MYLEG device . . . . .	72
5.1	Peroneal, plantar and tibial nerve to be targeted to obtain a somatotopic sensation on the dorsum, under the toes and on the heel respectively . . . . .	74
5.2	Two electronic boards placed over the foot of a diabetic subject to measure the exerted forces and the ankle joint angle. . . . .	74
5.3	Electrode placement and corresponding sensations when stimulating plantar, tibial and peroneal nerve. . . . .	75
5.4	Capability of an healthy subject to distinguish between (a) different locations, (b) different stimulation intensities and (c) different locations and intensities combined together. . . . .	76
5.5	Exploitation results for (a) touch, (b) proprioception and (c) the combination of the two. . . . .	76

---



---

# List of Tables

---

3.1	Polymer Li-Ion rechargeable battery pack characteristics . . . . .	15
3.2	MCP73871 Li-Polymer Battery Charge Management Controller characteristics . . . . .	15
3.3	LF33CPT-TR Voltage Regulator characteristics . . . . .	17
3.4	MMBT3906LT1G General Purpose PNP Transistor characteristics . . . . .	20
3.5	Data collected from 5 subjects (S1-S5) using the original board to understand the range of $R_{\text{INSOLE}}$ during walking . . . . .	22
3.6	LM4040CIM3-2.5/NOPB Shunt Voltage Reference characteristics . . . . .	22
3.7	LSM9DS1 Inertial Measurement Unit characteristics . . . . .	23
3.8	Comparison between different possible Bluetooth modules . . . . .	24
3.9	STM32F103RBT6 medium-density performance line ARM-based MCU characteristics	26
3.10	Design Rules imposed in Altium designer . . . . .	28
3.11	Reflow process temperature profile . . . . .	30
3.12	2.4 GHz Transceiver Breakout - nRF24L01+ characteristics . . . . .	35
3.13	Pros and cons of via-cable and wireless synchronization . . . . .	44
4.1	Raw data collected when aligning the IMU with z-, x- and y-axis respectively. . . . .	53
6.1	Comparison between original and new electronic circuit characteristics . . . . .	77



---

# Acronyms

---

**BLE** Bluetooth Low Energy. 25

**BR/EDR** Basic Rate/Enhanced Data Rate. 25

**DPN** Diabetic Peripheral Neuropathy. 3

**I2C** Inter-Integrated Circuit. 23

**IC** Integrated Circuit. 29

**IMU** Inertial Measurement Unit. xvi, 7, 13, 14, 22, 24, 31, 32, 39

**LLA** Lower Limb Amputation. xiii, 1

**MCU** MicroController Unit. 27, 32

**PCB** Printed Circuit Board. 14, 16

**PN** Peripheral Neuropathy. 3, 74

**RFCOMM** Radio Frequency COMMunication. 25, 48

**SCL** Serial CLock. 23

**SDA** Serial DAta. 23

---

**SMT** Surface Mounted Technology. 22

**SPI** Serial Peripheral Interface. 34

**SPP** Serial Port Profile. 25

**THT** Through Hole Technology. 22

**UART** Universal Asynchronous Receiver/Transmitter. 25

---

# Glossary

---

**dps** degree per second. 23

**GND** ground pin connect to the negative terminal of the power supply. 16

**mg** milli-g where g is the acceleration from Earth gravity. 23

**VBAT** voltage provided from the battery to the battery charger. 16

**VBUS** the voltage provided by plugging the micro USB 2.0 connector to an external plug for charging the battery. 15





---

# Abstract

---

## Introduction

Lower Limb Amputation (LLA) is a major problem all around the world affecting 200 thousand new people every year. 54% of lower limb amputations are caused by vascular diseases and 45% by traumas [2, 3]. The main problems that an amputee patient has to deal with in his everyday life are slow and asymmetric walking [4], increased risk of falls [5], low embodiment and phantom limb pain [6] and increased metabolic cost [7]. Depending on the level of amputation, it is possible to distinguish between transtibial and transfemoral amputations and the higher the level of amputation the more disabling the condition [4, 8, 9].

However, amputation is not the only pathological condition causing problem in walking due to lack of efficient and natural sensory feedback. Peripheral neuropathy refers to the condition that result when nerves that carry messages to and from the brain and spinal cord from and to the rest of the body are damaged or diseased. This causes tingling and burning pain, ulcers, infections and, most importantly for this project, lack of sensations at the extremities [10]. Diabetes is the major cause of peripheral neuropathy [11] and almost half of the people with diabetes have peripheral neuropathy [12].

In addition to being extremely disabling conditions for the patient, diabetes and amputations have an enormous impact on the economy of each country [13–15].

---

What these two pathological conditions have in common is that both amputation and peripheral neuropathy break the sensory communication between the brain and the lower limbs causing balance and walking problems. Very sophisticated lower limb prostheses have been developed to improve the control of the patient on his prosthetic leg and to restore motion function [16, 17]. However, very little research has been conducted in trying to restore sensory function [18, 19] and, among these very few studies, non-invasive approaches have been only developed for transtibial amputation [20–22].

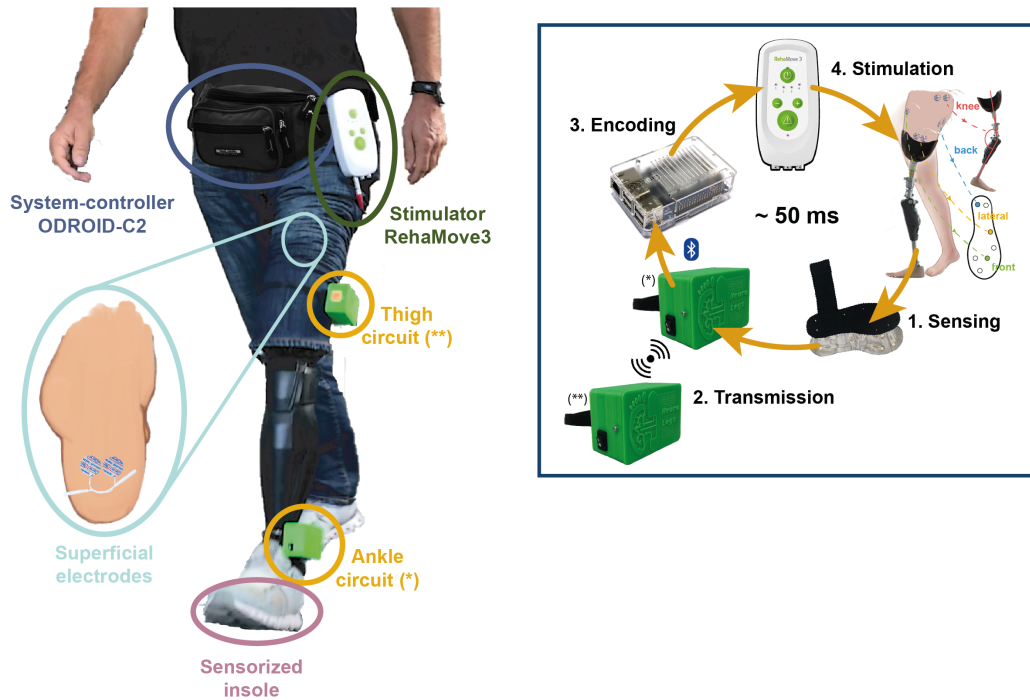
The MYLEG system from the Neuroengineering Laboratory at ETH Zürich aims at restoring sensory feedback to transfemoral amputees and diabetic patients using electrical stimulation. In this context, this master thesis project focuses on the design, the development and the testing of an electronic system used to provide patients with both tactile and proprioceptive feedback in real-time to boost the confidence, mobility and agility of the user while performing any type of walking activity.

## Materials and Methods

The final version of MYLEG real-time sensory-feedback device is shown in Figure 1 and it is constituted of 4 parts:

1. sensing: a custom-made sensorized insole measures the force exerted by the subject on his foot and records pressure information;
2. transmission: two electronic circuits conditions the force sensors, collects data from IMUs to measure knee flexion, samples the data and send it via Bluetooth to a system-controller;
3. encoding: the system-controller itself converts raw data coming from the electronic circuits into stimulation parameters and drives the electrical stimulation;
4. stimulation: a portable stimulator provides the stimulation using surface skin electrodes.

The readouts of the insole’s force sensors and the angle calculated from IMUs’ data are used to directly drive the electrotactile stimulation on the stump of the amputee or on



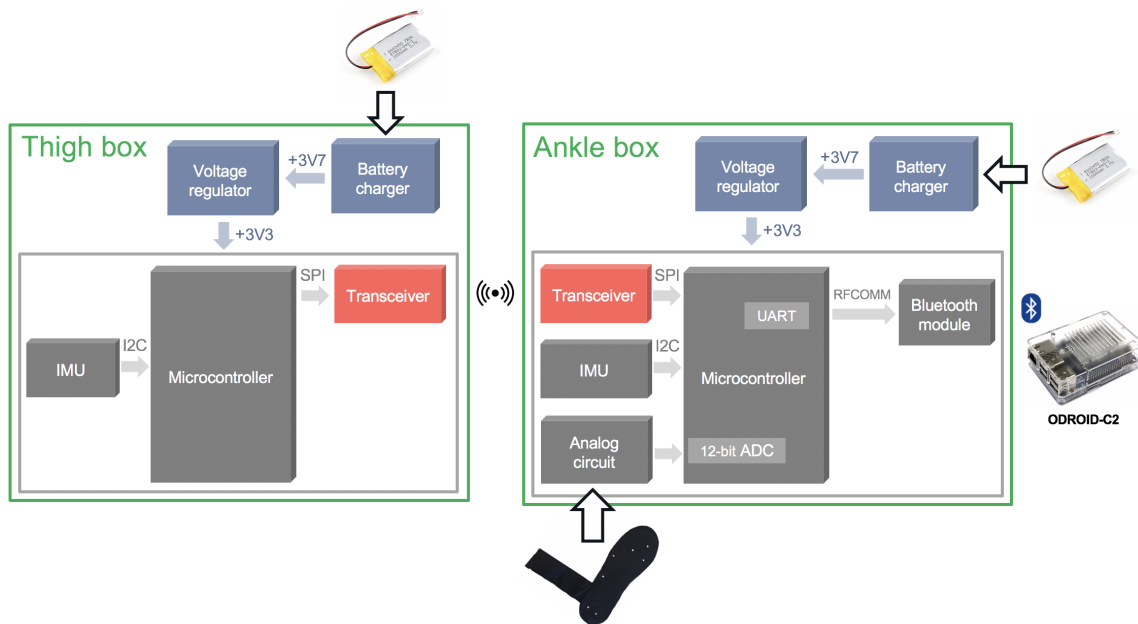
**Figure 1:** Global description of the MYLEG system used with a transfemoral amputee

the impaired foot of a diabetic patient. The algorithm that controls the stimulation is implemented on the system-controller and is written in C++. The intensity of the stimulation is obtained as a linear mapping of the exerted force and the estimated knee angle. Information regarding both the intensity of the pressure applied on the foot sole and the location of this pressure are taken from the sensorized insole and used to drive the stimulator.

The fundamental requisites of the device are the light weight and the small size of the electronic circuits, an improved communication between the different parts of the system to avoid disconnections, the ease of reprogrammability of the electronic boards, the possibility to synchronize multiple devices together and an accurate feedback on the proprioception of the knee. These were, in fact, the biggest limitations reported by the operators and/or the end-users while performing experiments with the first version of the MYLEG device.

To fulfil these requirements, two electronic circuits for data acquisition and transmission have been designed and developed. The two circuits are attached to the patient's leg according to Figure 1 and the schematic is shown in Figure 2.

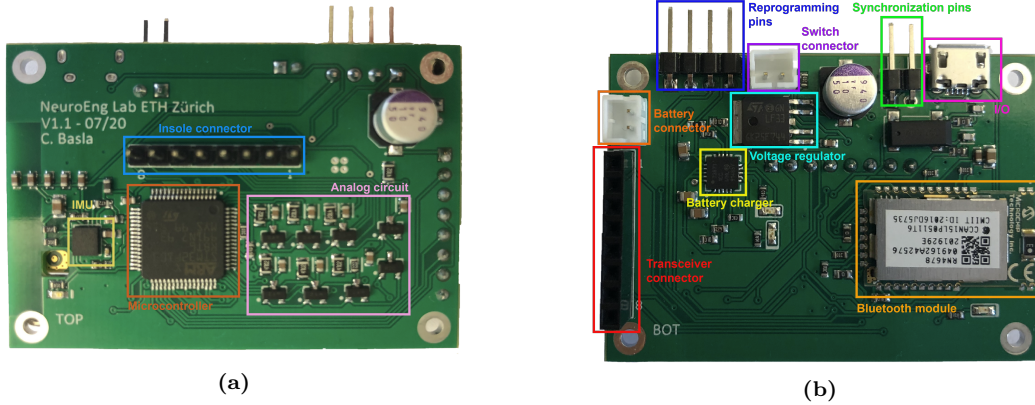
The circuit attached to the ankle of the subject consists of a lithium-ion rechargeable



**Figure 2:** Simplified schematic of the electronic circuits for data acquisition and transmission

battery that provides the input voltage that, after being regularized, powers all the other components. An analog circuit conditions the signals coming from the insole's force sensors to obtain a voltage output. These analog data are converted into digital signals by the ADC integrated in the microcontroller. An Inertial Measurement Unit (IMU) detects position, linear acceleration and angular rate of the foot and is used to measure the angle described by the shank. All these collected data are sent to the system controller through a Bluetooth module and then used to drive the stimulation. Figure 3 shows the final PCB that has been designed using Altium Designer, printed and manually assembled. The main components described above are highlighted and all the supplementary components and connections have been added according to the specifications that can be found in the datasheets.

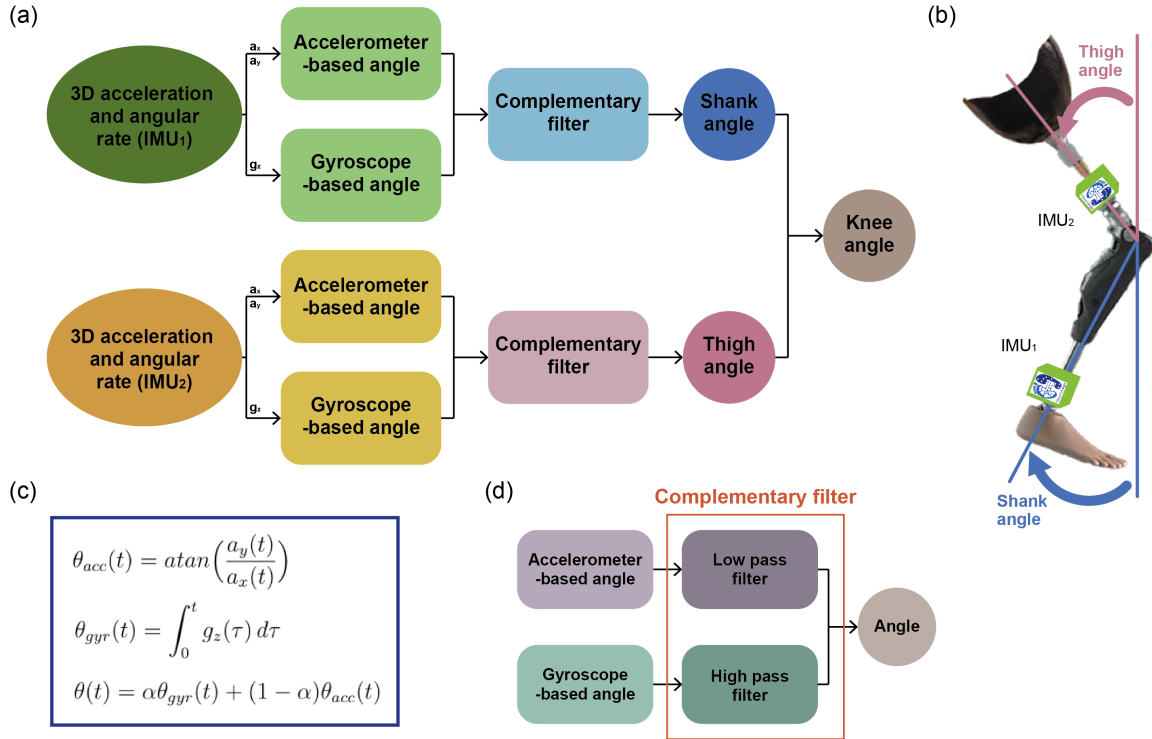
Analysis on the power dissipation of each component has been carried out to prevent overheating and burning of some parts, paying particular attention to their positioning over the PCB layers. In order to obtain a more reliable connection, a latest version Bluetooth module has been integrated. Its higher data rate and lower sensitivity allows for a faster discovery by the system controller and a reduction of the number of packets lost during the communication.



**Figure 3:** (a) top and (b) bottom layers of the designed PCB for data acquisition and transmission

In order to provide the subject with a very accurate feedback on the proprioception of his knee, another PCB has been designed to be attached over the thigh of the patient. In fact, inertial measurement data can be used to calculate hinge joint angles when at least one IMU is attached to each side of the joint. The circuit of the second board is similar to the one described above but simpler; it just comprises the power line and one IMU. For establishing the communication, the two boards have been equipped with a transceiver which is a device able to both transmit and receive information in the radio frequency spectrum. Data are sent from the box on the thigh to that on the ankle and then all the raw data are sent to the system controller via Bluetooth.

The algorithm implemented on the system controller to calculate the knee angle has been developed based on a complementary filter as described in Figure 4. Data from the accelerometer and the gyroscope of each IMU are used separately to calculate the angle and then combined together. The complementary filter applies a low-pass filter to the accelerometer data since they are affected by a high-frequency noise and a high-pass filter to the gyroscope data to remove the low-frequency drift. The coefficient of the filter has been obtained empirically in order to maximise the accuracy in reproducing the knee angle. Shank and thigh angle are calculated independently and then the knee angle is obtained as the sum of the two. The obtained angle is used to drive a directly proportional stimulation [18] so that a higher flexion of the knee corresponds to a higher intensity of the stimulation.



**Figure 4:** (a) knee angle algorithm; (b) shank and thigh angle calculated by the boards; (c) complementary filter formulas; (d) complementary filter schematic

Another priority of the system is the possibility to synchronize multiple devices together. Applying one device on each leg of the patient allows to perform gait analysis in absence of force platforms or 3D motion cameras by comparing the healthy leg with the prosthetic one. Two synchronization methods have been investigated: via cable and wirelessly. The main issues related to synchronization is the clock drift that is the delay that accumulates over time due to the slightly different timing of the microcontrollers of the two systems. To avoid this problem, the former method can be only used when the time of usage of the device is limited so that the drift between the clocks remains negligible; on the other hand, a wireless synchronization can face this problem by sending periodical synchronization packets allowing for a longer usage of the device. However, since at the moment the device utilization is limited to experiments, a synchronization via cable has been adopted. An on-purpose made synchronization cable has been developed and allows to complete the process in less than 30 seconds. However, while performing the validation tests on the device, a non-negligible drift has been measured even during short experiments. This delay has been demonstrated to be linear over time and a technique to quantify the accumulated delay and remove the

---

offset between the collected data has been implemented.

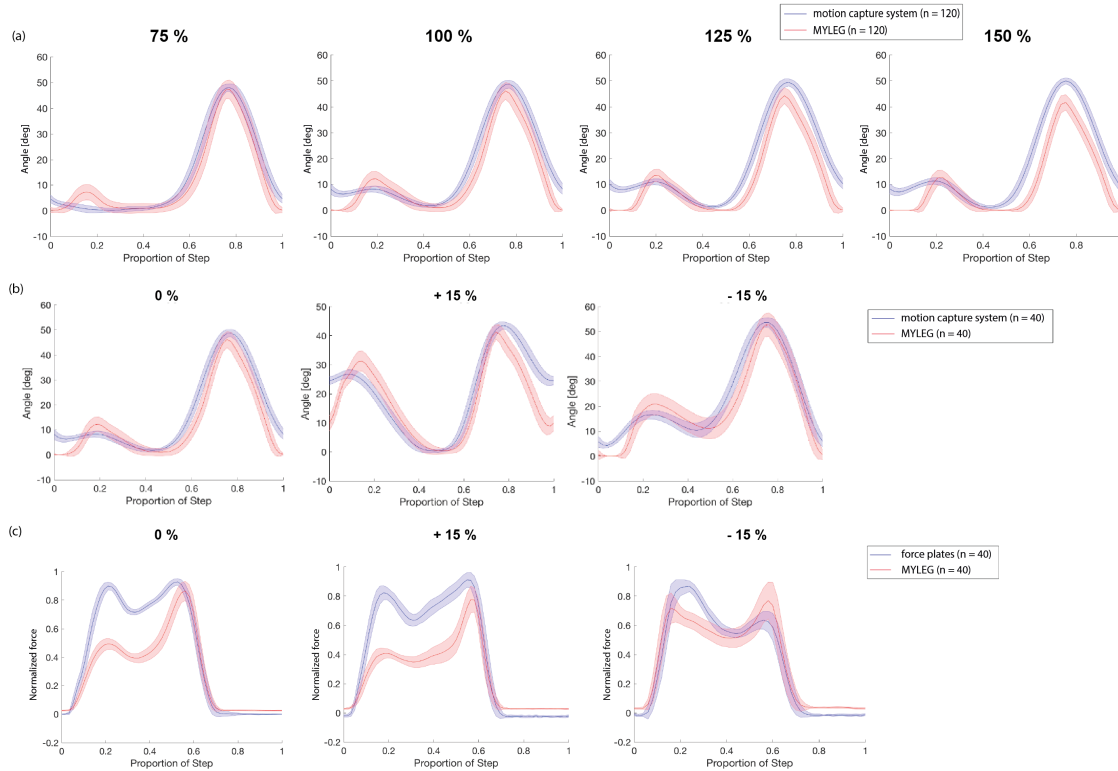
## **Validation**

The validation of MYLEG system has been performed comparing the estimated angle and force trends to that computed by a 3D motion capture system and force plates. Parameters of interest are the time delay to understand if the subject perceives a real-time stimulation, the amplitude accuracy and the trend reliability which represents the capability of the system to accurately reproduce the angle and force trends. This is extremely important since the subject is provided with a stimulation that has the same shape of that of the measured variables.

Firstly, a graphical comparison between the output of the original circuit and that of the ankle board of the new MYLEG system allows to demonstrate a reduced time delay and an increased amplitude accuracy and trend reliability of the latter system denoting that considering only one board already improves the joint angle estimate. Subsequently, the real need of the circuit applied to the thigh of the subject has been investigated. In particular, the second IMU plays a fundamental role in some daily-life activities, such as sitting down and standing up, in which the original board provides the subject with a misleading stimulation. Moreover, being able to provide the subject with information about the knee angle instead of just shank oscillations allows to better discriminate between swing phase, in which the knee is bent, and stance phase during which the knee is straight but the shank moves forwards.

In order to assess the accuracy of MYLEG system, data have been collected from one 23-years-old male healthy subject in the GRAIL room at Balgrist University Hospital in Zürich which is equipped with a treadmill, due force plates and the Vicon Nexus Motion Capture system. The experimental protocol consists of 2 over ground walking tasks, namely level walking at 4 different velocities and inclined walking at 3 different inclinations of the treadmill (ground level, inclined and declined walking). For the analysis, data have been post-processed and the real and estimated trends for angle and force have been extracted. Each full trial has been segmented into steps that

have been subsequently superimposed. Each distribution was tested for normality with single sample Kolmogorov-Smirnov goodness-of-fit hypothesis test and, since all distributions were found to be not normal, a Kruskal–Wallis test was performed.



**Figure 5:** (a) Knee angle comparison between the data obtained using a gold standard 3D capture motion system (blue line) and the MYLEG device (red line) at 4 different velocities (100 % corresponds to the subject’s self-selected comfortable walking speed); (b) knee angle comparison between the data obtained using a gold standard 3D capture motion system (blue line) and the MYLEG device (red line) at 3 different inclinations (0 % = ground level walking, + 15 % = inclined walking, - 15 % = declined walking); (c) force distribution comparison between the data obtained using force plates (blue line) and the MYLEG device (red line) at 3 different inclinations (0 % = ground level walking, + 15 % = inclined walking, - 15 % = declined walking).

Focusing on level ground walking at the subject’s self-selected comfortable speed, an equally distributed amplitude difference of approximately 10 % has been measured over the entire walking cycle; trend reliability has been demonstrated to be significantly higher ( $p \ll 0.001$ ) during the swing phase than in the stance and this could be associated to vibration of the boards when the foot hit the treadmill during the heel strike. Considering the force estimation, great accuracy has been demonstrated in predicting the timing of the force peaks. However, higher difference in the ratio between the two peaks has been shown due to the uneven distribution of the force sensors under the foot sole. Comparing the self-selected comfortable speed results to



---

the other tested velocities, a slight percentage increase in the peaks' amplitude difference has been noticed as the velocity increases while trend reliability over the entire walking cycle shows a significant difference at all 4 velocities. However, this result does not hold any longer if only the swing phase is considered guaranteeing an accuracy of around 80 % at each velocity. Inclined walking analysis brings to similar results to that described above confirming that the joint angle algorithm is able to precisely replicate also patterns that are extremely different from that of the normal ground level walking. A non-significantly different percentage error in the amplitude accuracy has been obtained for all the 3 inclined tasks.

## **Conclusion**

Two functioning PCBs have been designed, printed, assembled and tested in different scenarios encountering no problems related to the electronics. The main issues associated with the original board has been overcome obtaining a lighter, smaller, faster and longer-lasting device. A fully portable and comfortable design has been achieved allowing for real-time restoration of sensory feedback in different pathological populations. In fact, the implementation of a two-leg simultaneous stimulation system allows to enlarge the target population not only to amputees but also diabetic patients as well as any other pathological condition that causes asymmetric walking and in which, often, both feet and/or legs are involved. In future work, the newly implemented MY-LEG device will be tested both with amputees and diabetic patients to evaluate the success of non-invasive sensory restoration.

The highly promising results described above not only confirms the capability of MY-LEG system to provide accurately and in real-time sensory feedback to the patient but also gives the possibility to use MYLEG device for clinical monitoring and data collection during everyday life activities. In particular, the possibility to compare joint angle trends and force distributions over both legs provides an accurate method for evaluating subject's walking pattern, discovering abnormalities and asymmetries and keeping track of improvements or onset of walking-related issues over time.



---

# Sommario

---

## Introduzione

Ogni anno nel mondo 200 mila persone si sottopongono ad amputazione degli arti inferiori. Il 54 % delle amputazioni è causato da malattie vascolari e il 45 % da traumi [2, 3]. I principali problemi che un paziente amputato deve affrontare nella sua vita quotidiana sono: deambulazione lenta e asimmetrica [4], aumento del rischio di cadute [5], low embodiment, phantom limb pain [6] e aumento del consumo metabolico [7]. A seconda del livello di amputazione, è possibile distinguere tra amputazione transtibiale e transfemorale e ad un maggior livello di amputazione corrisponde una condizione maggiormente disabilitante [4, 8, 9].

L'amputazione, tuttavia, non è l'unica condizione patologica che causa problemi nel camminare a causa della mancanza di un feedback sensoriale efficiente e naturale. Neuropatia periferica si riferisce alla condizione che si verifica quando i nervi che trasportano l'informazione dal cervello e dal midollo spinale verso il resto del corpo e viceversa sono danneggiati. Ciò causa formicolio e bruciore, ulcere, infezioni e, aspetto più importante per questo progetto, mancanza di sensazioni alle estremità [10]. Il diabete è la principale causa di neuropatia periferica [11] e quasi la metà delle persone con diabete ne soffre [12].

Oltre ad essere condizioni estremamente invalidanti per il paziente, diabete e amputazione hanno un enorme impatto sull'economia di ciascun paese [13–15].

---

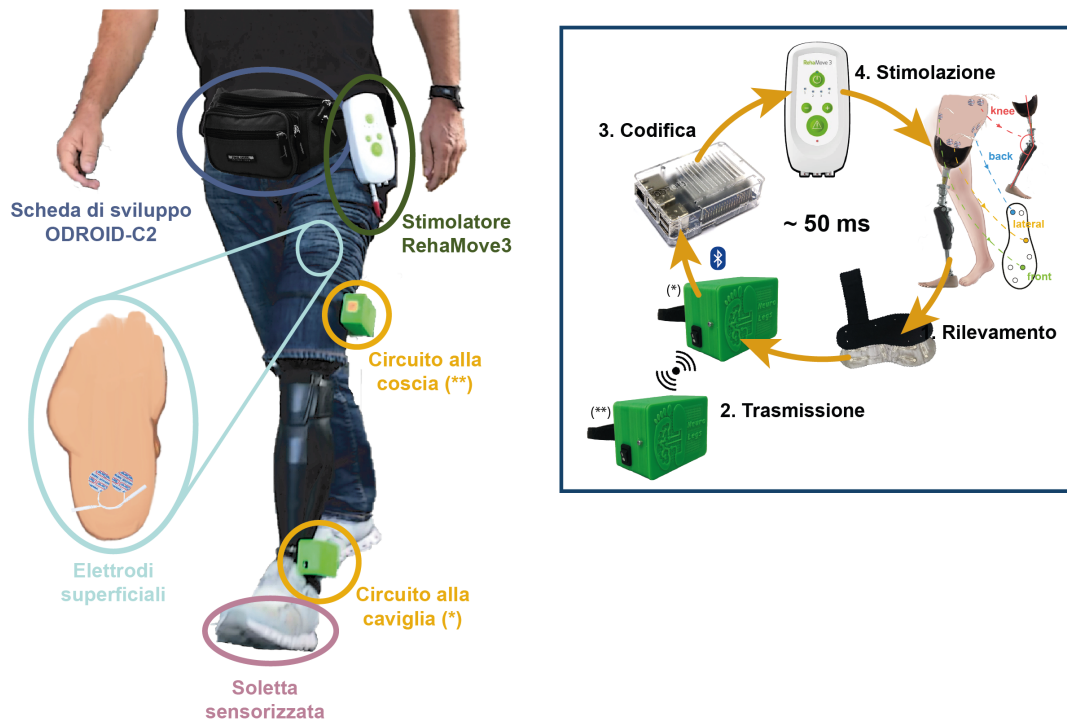
Ciò che accomuna queste due condizioni patologiche è l'interruzione della comunicazione sensoriale tra il cervello e gli arti inferiori causando problemi di equilibrio e deambulazione. Protesi molto sofisticate sono state sviluppate per migliorare il controllo del paziente sulla propria gamba protesica e per ripristinarne la funzione motoria [16, 17]. Tuttavia, pochissime ricerche sono state condotte nel tentativo di ripristinare la funzione sensoriale [18, 19] e, tra questi pochissimi studi, approcci non invasivi sono stati sviluppati solo per amputazione transtibiale [20–22].

Il sistema MYLEG del Laboratorio di Neuroingegneria dell'ETH di Zurigo mira a ripristinare il feedback sensoriale ad amputati transfemorali e a pazienti diabetici mediante stimolazione elettrica. In tale contesto, questo progetto di tesi si concentra sulla progettazione, lo sviluppo e la validazione di un sistema elettronico utilizzato per fornire ai pazienti un feedback sia tattile che propriocettivo in tempo reale per aumentare la fiducia, la mobilità e l'agilità dell'utente durante l'esecuzione di qualsiasi tipo di attività motoria.

## **Materiali e metodi**

La versione definitiva del dispositivo per sensory-feedback MYLEG è mostrato nella Figura 6 e comprende 4 parti:

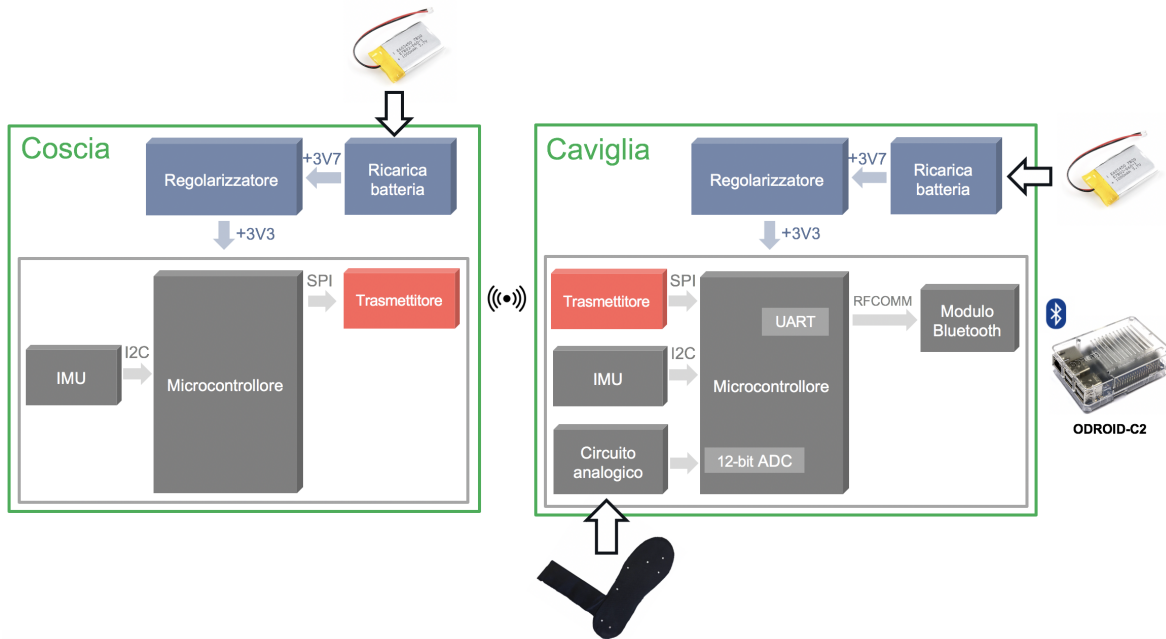
1. rilevamento: una soletta sensorizzata misura la forza esercitata dal soggetto sul piede e registra informazioni di pressione;
2. trasmissione: due circuiti elettronici condizionano i sensori di forza, raccolgono dati da due IMU per misurare la flessione del ginocchio, campionano i dati e li inviano tramite Bluetooth ad una scheda di sviluppo;
3. codifica: la scheda di sviluppo stessa converte i dati provenienti dai circuiti elettronici in parametri di stimolazione e guida la stimolazione elettrica;
4. stimolazione: uno stimolatore portatile fornisce la stimolazione utilizzando elettrodi superficiali.



**Figura 6:** Descrizione generale del dispositivo MYLEG

La lettura dei sensori di forza della soletta e l'angolo calcolato con i dati degli IMU vengono utilizzati per guidare la stimolazione elettrotattile sul moncone dell'amputato o sul piede di un paziente diabetico. L'algoritmo che controlla la stimolazione è implementato sulla scheda di sviluppo ed è scritto in C ++. L'intensità della stimolazione è ottenuta come una mappatura lineare della forza esercitata sulla soletta e della stima dell'angolo del ginocchio. Informazioni riguardanti sia l'intensità che la posizione della pressione vengono prese in considerazione per controllare lo stimolatore.

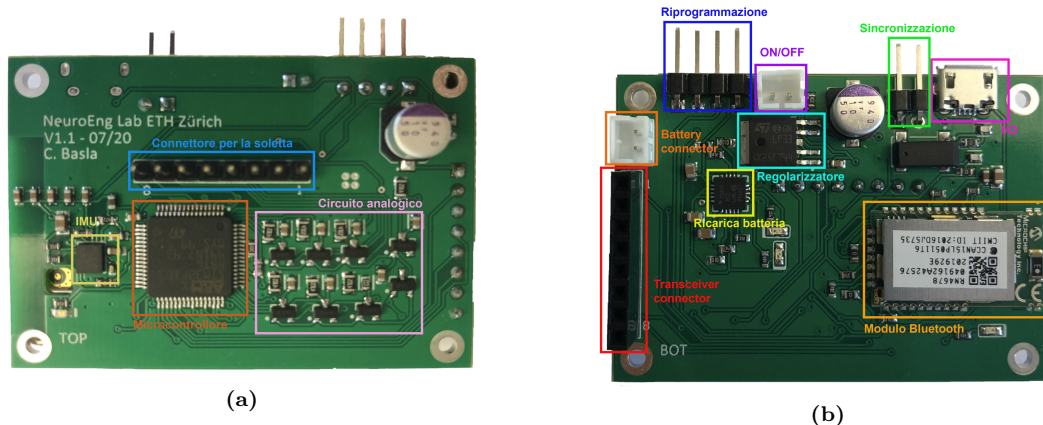
Requisiti fondamentali del progetto sono la leggerezza e le ridotte dimensioni dei circuiti, una migliore comunicazione tra le diverse parti del sistema per evitare disconnessioni, la facilità di riprogrammazione delle schede elettroniche, la possibilità di sincronizzare più dispositivi insieme e la restituzione di un feedback accurato sulla flessione del ginocchio. Rappresentano queste, infatti, le maggiori limitazioni riportate da operatori e/o utenti durante gli esperimenti eseguiti con la prima versione del sistema MYLEG. Per soddisfare tali requisiti, due circuiti elettronici per l'acquisizione e la trasmissione dei dati sono stati progettati e sviluppati. I due circuiti sono attaccati alla gamba del paziente secondo la Figura 6 e il loro schematico è mostrato in Figura 7.



**Figura 7:** Schematico semplificato dei circuiti elettronici per l'acquisizione e la trasmissione di dati

Il circuito attaccato alla caviglia del paziente è costituito da una batteria agli ioni di litio ricaricabile che fornisce la tensione di ingresso che, dopo essere stata regolata, alimenta tutti gli altri componenti. Un circuito analogico condiziona i segnali provenienti dai sensori di forza della soletta per ottenere una tensione in uscita. Questi dati analogici vengono convertiti in segnali digitali dall'ADC integrato nel microcontrollore. Un'unità di misura inerziale (IMU) rileva la posizione, l'accelerazione lineare e la velocità angolare del piede e viene utilizzata per misurare l'angolo descritto dalla gamba. Tutti i dati raccolti vengono inviati alla scheda di sviluppo tramite un modulo Bluetooth e quindi utilizzati per controllare la stimolazione. La figura 8 mostra la PCB finale che è stata progettata utilizzando Altium Designer, stampata e assemblata manualmente. I principali componenti sopra descritti sono stati evidenziati e tutti i componenti e collegamenti aggiuntivi sono stati introdotti secondo le specifiche che si possono trovare nelle schede tecniche.

Un'analisi sulla dissipazione di potenza di ciascun componente è stata eseguita per evitare il surriscaldamento di alcune parti, prestando particolare attenzione al loro posizionamento su entrambi i lati della PCB. Per ottenere una connessione più affidabile, un modulo Bluetooth di ultima generazione è stato introdotto. La maggiore velocità

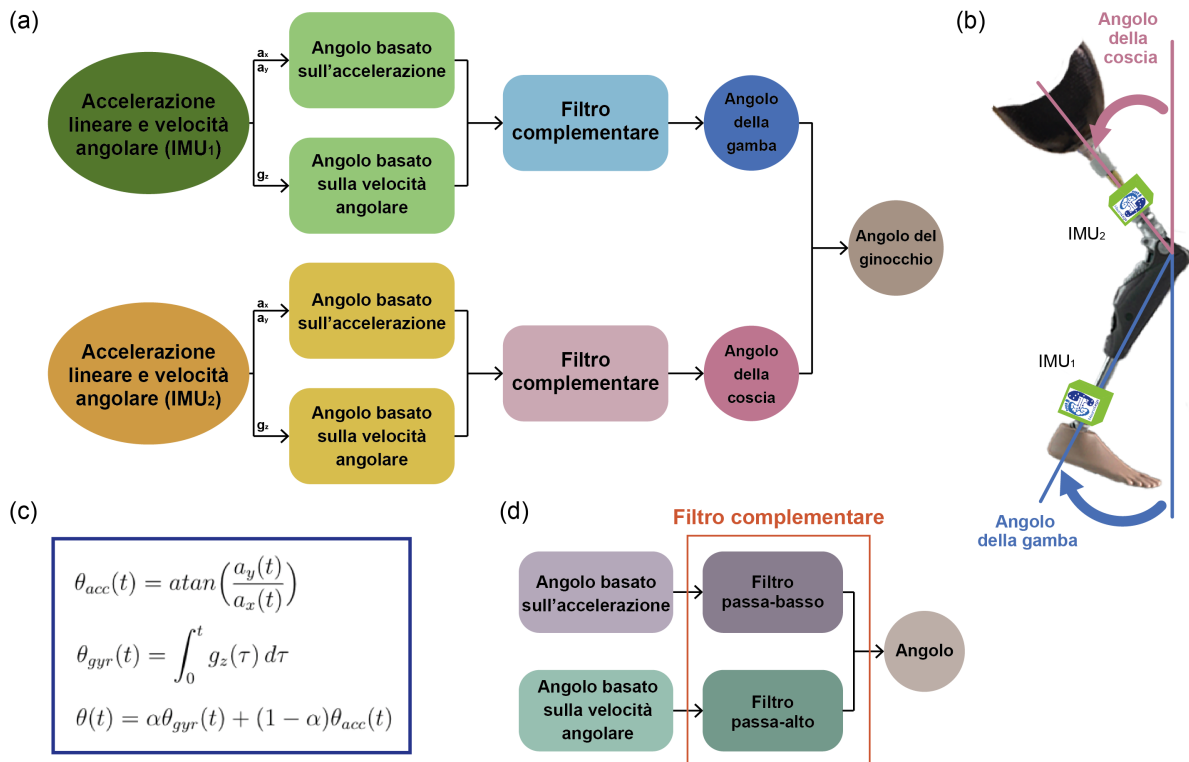


**Figura 8:** (a) layer superiore ed (b) inferiore del circuito stampato per l'acquisizione e la trasmissione dei dati

di trasmissione dei dati consente una più rapida connessione con la scheda di sviluppo e una riduzione del numero di pacchetti persi durante la comunicazione.

Per fornire al soggetto un feedback accurato sulla propriocezione del ginocchio, un'altra PCB da applicare sulla coscia del paziente è stata progettata. Infatti, i dati raccolti da sensori inerziali possono essere utilizzati per calcolare l'angolo del ginocchio quando almeno una IMU è attaccata a ciascun lato dell'articolazione. Il circuito della seconda scheda è simile a quello sopra descritto ma più semplice, comprendendo solamente la linea di alimentazione e una IMU. Per stabilire la comunicazione, i due circuiti sono stati dotati di un ricetrasmittitore, ovvero un dispositivo in grado sia di trasmettere che di ricevere informazioni nello spettro delle radiofrequenze. I dati vengono trasmessi dalla scatola sulla coscia a quella sulla caviglia e successivamente inviati alla scheda di sviluppo tramite Bluetooth.

L'algoritmo implementato per calcolare l'angolo del ginocchio è stato sviluppato sulla base di un filtro complementare come descritto nella Figura 9. I dati dell'accelerometro e del giroscopio di ciascuna IMU vengono utilizzati separatamente per calcolare l'angolo e quindi combinati insieme successivamente. I dati dell'accelerometro sono processati con un filtro passa-basso poiché influenzati da rumore ad alta frequenza mentre quelli del giroscopio utilizzano un filtro passa-alto per rimuovere l'errore a bassa frequenza. Il coefficiente del filtro è stato ottenuto empiricamente al fine di massimizzare l'accuratezza nella stima dell'angolo del ginocchio. Gli angoli della gamba e della coscia



**Figura 9:** (a) algoritmo per il calcolo dell'angolo del ginocchio; (b) angolo della gamba e della coscia calcolati dalle schede elettroniche; (c) formule per il calcolo dell'angolo del ginocchio; (d) filtro complementare

vengono calcolati indipendentemente e successivamente sommati per ottenere l'angolo del ginocchio. L'angolo così ottenuto viene utilizzato per generare una stimolazione direttamente proporzionale [18] in modo che una maggiore flessione del ginocchio corrisponda ad una maggiore intensità della stimolazione.

Un'altra priorità del sistema è la possibilità di sincronizzare più dispositivi insieme. Il posizionamento di un dispositivo su ciascuna gamba del paziente consente di eseguire l'analisi del cammino anche in assenza di piattaforme di forza o sistemi 3D di acquisizione del movimento, confrontando l'andamento della gamba sana con quella protesica. Due metodi differenti di sincronizzazione sono stati valutati: via cavo e wireless. La principale problematica legata alla sincronizzazione è rappresentata dal ritardo accumulato nel tempo a causa della temporizzazione leggermente diversa dei microcontrollori dei due sistemi. Per questo motivo, il primo metodo può essere impiegato solo quando il tempo di utilizzo del dispositivo è limitato, in modo tale che l'errore accumulato tra i clock rimanga trascurabile, mentre una sincronizzazione wireless è in



---

grado di affrontare questo problema inviando pacchetti di sincronizzazione periodici che permettono l'utilizzo del dispositivo per un tempo maggiore. Tuttavia, poiché al momento l'utilizzo del dispositivo è limitato alla fase sperimentale, una sincronizzazione via cavo è stata adottata. Un cavo di sincronizzazione è stato appositamente realizzato per consentire di completare il processo in meno di 30 secondi. Tuttavia, durante l'esecuzione dei test di validazione sul dispositivo, un offset non trascurabile tra i due microcontrollori è stato misurato anche durante brevi esperimenti. Questo ritardo può, tuttavia, essere considerato lineare nel tempo ed una tecnica per quantificare il ritardo accumulato e rimuovere l'offset tra i dati raccolti è stata implementata.

## **Validazione**

La validazione del sistema MYLEG è stata eseguita confrontando l'angolo e l'andamento della forza stimati dal dispositivo con quello calcolato da un sistema 3D di acquisizione del movimento e da piattaforme di forza. I parametri di interesse, presi in considerazione durante l'analisi dei tracciati, sono il ritardo temporale per capire se il soggetto è in grado di percepire una stimolazione in tempo reale, l'accuratezza nel replicare l'ampiezza delle curve reali e l'affidabilità del trend che rappresenta la capacità del sistema di riprodurre accuratamente l'andamento dell'angolo e della forza. Ciò è estremamente importante poiché il soggetto viene fornito con una stimolazione che ha la stessa forma di quella delle variabili misurate.

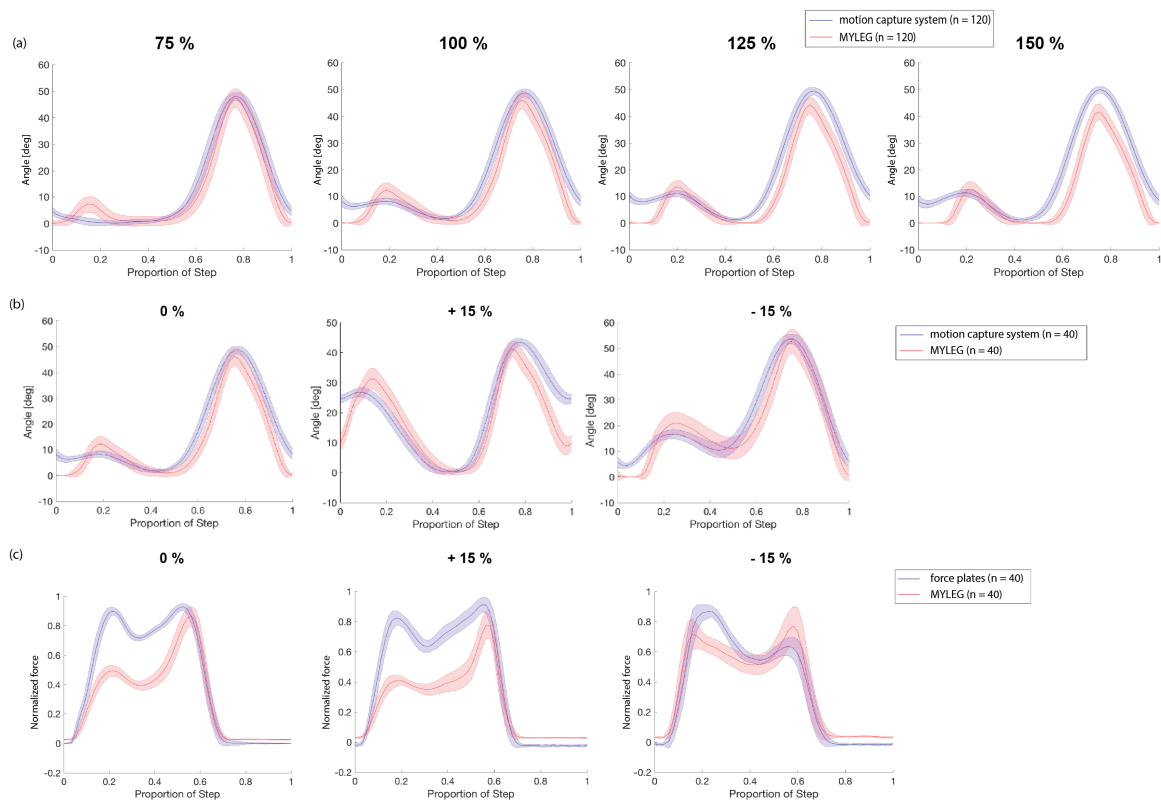
In primo luogo, un confronto grafico dei dati collezionati della scheda inferiore del nuovo sistema MYLEG con quelli del circuito originale dimostra una riduzione del ritardo e una maggiore accuratezza dell'ampiezza e dell'affidabilità del trend permettendo di affermare che, anche considerando un solo circuito, la stima dell'angolo articolare risulta migliorata. Successivamente, la reale necessità del circuito applicato sulla coscia del soggetto è stata indagata. In particolare, la seconda IMU svolge un ruolo fondamentale in alcune attività della vita quotidiana, come alzarsi e sedersi, in cui il circuito originale fornisce al soggetto una stimolazione fuorviante. Inoltre, essere in grado di fornire al soggetto informazioni sull'angolo del ginocchio anziché solo sulle oscillazioni della gamba consente di discriminare meglio tra fase di swing, in cui il ginocchio è piegato, e fase

---

di stance (appoggio) durante la quale il ginocchio è teso ma la gamba si muove in avanti.

Per valutare l'accuratezza dell'intero sistema MYLEG, un soggetto sano di sesso maschile di 23 anni è stato sottoposto ad una serie di esperimenti nella stanza GRAIL del Balgrist University Hospital di Zurigo, la quale è dotata di un tapis roulant, due piattaforme di forza e il sistema Vicon Nexus per l'acquisizione del movimento. Il protocollo sperimentale richiede al soggetto di camminare in piano a 4 diverse velocità e successivamente a 3 diverse inclinazioni (piano, salita e discesa). Per l'analisi, i dati sono stati processati e le curve reali e stimate sono state estratte sia per l'angolo che per la forza. I singoli passi sono stati individuati da ciascuna prova e passi alla stessa velocità o inclinazione sono stati successivamente sovrapposti. Ogni distribuzione è stata testata per la normalità con il test di ipotesi di Kolmogorov-Smirnov a campione singolo e, poiché tutte le distribuzioni sono risultate non normali, il test di Kruskal-Wallis è stato eseguito per confrontare le singole prove tra di loro.

Concentrandosi sulla camminata in piano alla velocità considerata confortevole dal soggetto, una differenza di ampiezza equamente distribuita sull'intero ciclo di deambulazione di circa il 10 % è stata misurata; inoltre, è stato dimostrato che l'affidabilità del trend è significativamente maggiore ( $p \ll 0,001$ ) durante la fase di swing rispetto alla stance e ciò potrebbe essere associato alla vibrazione dei circuiti nel momento in cui il piede colpisce il tapis roulant durante l'heel strike. La stima della forza è caratterizzata da una grande accuratezza nella previsione della tempistica dei picchi di forza. Tuttavia, una maggiore differenza nel rapporto tra i due picchi è stata evidenziata ed è dovuta ad una distribuzione non uniforme dei sensori di forza all'interno della soletta sensorizzata. Confrontando i risultati ottenuti alla velocità selezionata dal paziente con le altre velocità testate, l'errore percentuale nell'approssimazione dell'ampiezza dei picchi aumenta leggermente all'aumentare della velocità mentre l'affidabilità del trend sull'intero ciclo di camminata mostra una differenza significativa a tutte e 4 le velocità. Tuttavia, questo risultato non è più valido se si considera solamente la fase di swing, la quale garantisce una precisione di circa l'80% ad ogni velocità. L'analisi della camminata inclinata ha permesso di ottenere risultati simili a quanto sopra descritt-



**Figura 10:** (a) Confronto dell'angolo del ginocchio tra l'andamento calcolato con un sistemi di acquisizione del movimento (linea blu) e quello stimato dal sistema MYLEG (linea rossa) a 4 diverse velocità (100 % corrisponde alla velocità di deambulazione scelta dal soggetto); (b) confronto dell'angolo del ginocchio tra l'andamento calcolato con un sistemi di acquisizione del movimento (linea blu) e quello stimato dal sistema MYLEG (linea rossa) a 3 diverse inclinazioni (0 % = piano, + 15 % = salita, - 15 % = discesa); (c) confronto della distribuzione delle forze tra l'andamento calcolato con piattaforme di forza (linea blu) e quello stimato dal sistema MYLEG (linea rossa) a 3 diverse inclinazioni (0 % = piano, + 15 % = salita, - 15 % = discesa).

to confermando che l'algoritmo utilizzato per il calcolo dell'angolo del ginocchio è in grado di replicare con precisione anche andamenti del cammino estremamente diversi da quello della normale camminata in piano. Per tutti e 3 i trial inclinati, l'errore percentuale nella stima dell'ampiezza non è risultato significativamente differente.

## Conclusione

In conclusione, durante il progetto di tesi, sono state progettate, stampate, assemblate e testate in diversi scenari due PCB senza riscontrare problemi legati all'elettronica. I principali problemi associati alla scheda originale sono stati superati ottenendo un dispositivo più leggero, di dimensioni minori, permettendo una connessione più rapida e veloce e garantendo una maggiore durata della batteria. Il dispositivo è confortevole

---

e facilmente indossabile e consente il ripristino in tempo reale del sensory-feedback in diverse popolazioni patologiche. Infatti, l'implementazione di un sistema di stimolazione simultanea per entrambe le gambe consente di allargare la popolazione target non solo ad amputati ma anche a pazienti diabetici e, in generale, a qualsiasi altra condizione patologica che causa una deambulazione asimmetrica e in cui, spesso, entrambi i piedi e/o le gambe sono coinvolti. In sviluppi futuri, il nuovo dispositivo MYLEG sarà testato sia con amputati che con pazienti diabetici per valutarne il successo nel ripristino sensoriale con approccio non invasivo.

I risultati altamente promettenti sopra descritti non solo confermano la capacità del sistema MYLEG di fornire un sensory-feedback accurato e in tempo reale al paziente, ma introducono anche la possibilità di utilizzare il dispositivo MYLEG per il monitoraggio clinico e la raccolta dati durante attività di vita quotidiana. In particolare, la possibilità di confrontare l'andamento degli angoli articolari e la distribuzione della forza su entrambe le gambe fornisce un metodo accurato per valutare la deambulazione del soggetto, scoprire anomalie e asimmetrie e tenere traccia nel tempo dei miglioramenti o dell'insorgenza di problemi legati al cammino.

# Introduction

---

## 1.1 Lower limb amputation

Lower Limb Amputation (LLA) is the removal of a part or multiple parts of the lower limb. It represents an enormous problem all around the world. In fact, over 150 thousand people undergo amputations of their lower extremity in the United States every year [23] and, currently, there are approximately 300 thousand individuals affected by LLA in Europe [24]. Amputations secondary to vascular disease account for the 54 % of the total cases, and of these, over two thirds have been diagnosed with diabetes. Another relevant cause is peripheral artery disease [2]. An additional 45 % of the prevalent cases is associated to traumas such as car or motorbike accidents while cancer only accounts for the remaining less than 2 % [3]. With respect to upper limb amputations, LLA has a higher prevalence accounting for the 69 % of all the persons living with the loss of a limb [25]. Among these, over one half amputations are major [3] i.e. above the ankle level.

LLA is an extremely disabling condition for the patient obliging him to face many difficulties during his everyday life and causing not only physical problems in interfacing with the surrounding environment but also and not less important psychological disorders. Lower limb amputees are very slow in walking [4] and they risk very dangerous falls [5]. Moreover, they are exhausted and physiologically stressed after very

few steps and very scared and careful in doing stairs walking since any of them have experienced serious falls during the rehabilitation phase. The highly asymmetric and irregular walking pattern causes not physiological distribution of the load, overloading of the healthy leg, back pain, osteoarthritis [26] and an increase in the cognitive burden [27] and metabolic cost while walking together with a 120 % higher probability of heart attack [7]. 50 to 80 % of amputee patients are affected by phantom limb pain [6] which is a transient or persistent pain in the missing limb requiring them to assume morphine-based drugs. This has a series of other adverse consequences, such as tiredness, impossibility to work or to drive, that force the patient to prefer not to take the drugs. Moreover, another very common problem is the low embodiment being the prosthesis perceived as an external object. This causes the abandonment of the prosthesis [28] and the need for more care.

## 1.2 Transfemoral amputation

Depending on the level of the amputation, it is possible to distinguish between transtibial and transfemoral amputation corresponding to a loss of the lower limb above the ankle level and above the knee level respectively. A more disabling condition is associated to a higher level of the amputation with a reduced walking speed and an increase energy cost [9]. This relates to a greater length of the prosthesis and to the lack of control at the knee joint which determine a higher asymmetric walking pattern [4]. Another major problem is the impossibility for transfemoral amputees to wear the prosthesis by themselves [8]. In fact, according to Christensen and colleagues [29] only the 50 % is able to don the prosthesis alone, much lower if compared to the 83% of those with transtibial amputations. Transfemoral amputations also cause a higher rate of prosthesis abandonment, accounting for the 76% of all the patients that do not use the prosthesis [8], and a higher rate of falls [8].

Houghton et al. [30] demonstrated that an extremely limited number of above-knee amputees takes part in satisfactory rehabilitation (33 %) if compared to through-knee amputees (62 %) and that the former group relies significantly more on wheelchairs than the latter.

## 1.3 Peripheral Neuropathy

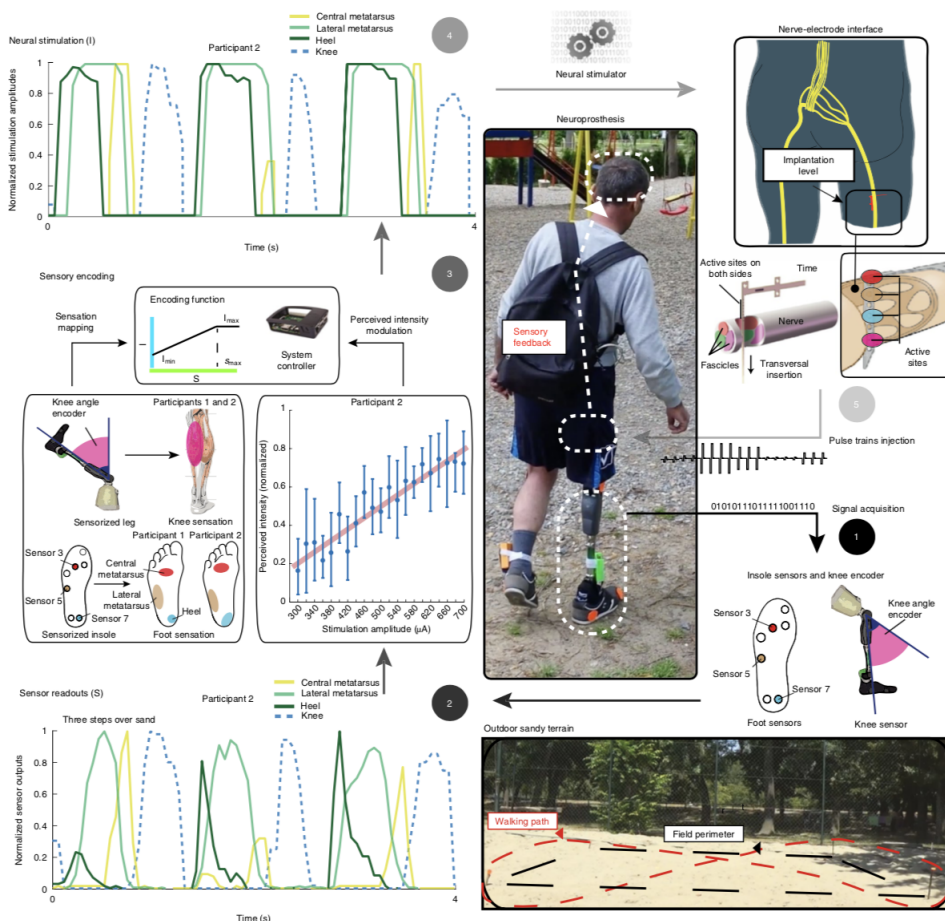
Peripheral Neuropathy (PN) refers to the damage of the nerves that carry information from the brain and the spinal cord to the rest of the body and vice versa. This pathological condition is commoner than is usually thought affecting 2 to 7 % of people all around the world [31]. However, the incidence of PN increases if more vulnerable subgroups are considered such as people over 65 years old. The main cause of peripheral neuropathy is diabetes. Diabetic Peripheral Neuropathy (DPN) accounts for the one-third of all the PN cases [11] and almost half of the people with diabetes is affected by peripheral neuropathy [12]. Other frequent etiologies are chemo-induced PN which has gained importance due to the risen prevalence of tumours and autoimmune or infectious diseases such as lupus or rheumatoid arthritis [32] and alcoholic PN which interests the 46.3% of the chronic alcohol users [33]. Moreover, there are many cases in which the causes of the PN remain unknown. This is referred to as Idiopathic PN and accounts for approximately the 25 % of all the cases [31].

The most common problems associated with PN are tingling, burning pain and lack of sensations at the extremities. In particular, DPN-related loss of plantar cutaneous sensation causes ulcers and infections that contribute to over 90% of the non-traumatic lower limb amputations [10]. Another consequence that contributes to generate an abnormal walking pattern in people with PN is the reduced lower-extremity strength [34]. Therefore, this pathological population is affected by a higher rate of falls and reduced walking speed [35].

## 1.4 Sensory Feedback restoration

What amputation and peripheral neuropathy have in common is the fact that they both break the sensory communication between the central nervous system and the lower limb's extremities causing balance and walking problems. Very sophisticated lower limb prostheses have been developed to improve the control of the patient on his prosthetic leg and to restore motion function [16]. For example, Hargrove et al. [17] developed a real-time control algorithm for integrating electromyographic (EMG)

data and historical information from prior gait strides to a powered prosthetic leg. However, very little research has been conducted in trying to restore sensory function. Among these very few studies, both invasive and non-invasive approaches have been investigated. Invasive technologies have been developed both for transfemoral [18] and transtibial [19] amputees and have shown huge benefits both in the walking pattern (i.e. increased walking speed, increased fall prevention, increased agility) and mental health (i.e. increase self-reported confidence and embodiment and reduced pain) [1]. Invasive approach is able to restore a somatotopic (i.e. at the phantom site) and homologous (i.e. of the same or similar type) sensation. It does not require any training of the subject since the information is naturally conveyed to the central nervous system, but it requires a surgical intervention for the electrodes' implantation.



**Figure 1.1:** Principle of working of a neuroprosthesis for sensory-feedback restoration with invasive approach [1]

On the other hand, non-invasive studies to restore sensory feedback have been up to



now only developed for transtibial amputation [20–22], which, due to the longer stump, is a less disabling condition with respect to above-knee amputation. Vibrotactile [21] or electrocutaneous [22] feedback have been used to give back to the patient information about the pressure applied on his prosthetic foot and positive results in standing balance, stability and postural control have been shown. In case of non-invasive stimulation, the perceived sensation is non-homologous since usually vibration or tingling are felt by the subject and non-somatotopic, thus remapped, since the nerves in the stump of the patient are deep and superficial electrodes are not able to directly target them. This requires some training time to create an association between the part of the body in which the sensation is felt and the corresponding location in the prosthesis.



# MYLEG device

---

MYLEG system is an electronic device designed and developed at the Neuroengineering Laboratory, ETH Zürich to restore sensory feedback while walking using electrical stimulation in order to perceive foot and knee sensations. The target users are amputees, diabetic patients and all subjects that suffer from peripheral neuropathy causing ulcers and reduced sensations under the feet. The final goal is to boost confidence, mobility and agility of the user while performing any type of walking activity.

The first prototype of the entire system can be divided into 4 different parts illustrated in Figure 2.1:

1. sensing: a custom-made sensorized insole with 7 force sensors distributed on the foot sole that captures the force exerted by the subject on his prosthetic foot and record pressure information;
2. transmission: an electronic board that conditions the signals coming from the insole's force sensors, acquires the data from an Inertial Measurement Unit (IMU), samples the data and send it via Bluetooth to a system-controller;
3. encoding: the system-controller itself (implemented on ODROID-C2) that manages the encoding algorithm to transduce the acquired data into stimulation parameters;

4. stimulation: a portable stimulator RehaMove 3 that provides the proper sensory feedback to the user through TENS (Transcutaneous Electrical Nerve Stimulation) using surface skin electrodes.



**Figure 2.1:** Global description of the MYLEG system

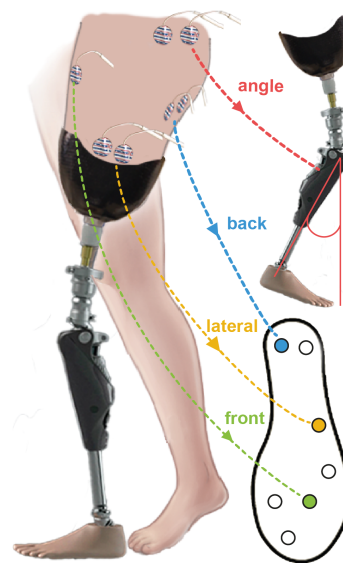
The different parts of the device communicate together as described below:

- the sensorized insole is directly plugged into the electronic circuit through 8-pins female and male connectors;
- the electronic board communicates to the system controller via Bluetooth;
- the system controller is connected with an USB cable to the stimulator.

A laptop needs to be used for starting the device but can be disconnected as soon as all the communications have been installed or used to check the trends of the collected data in real time. The system controller ODROID-C2 is connected to the experimenter's personal laptop via WiFi.

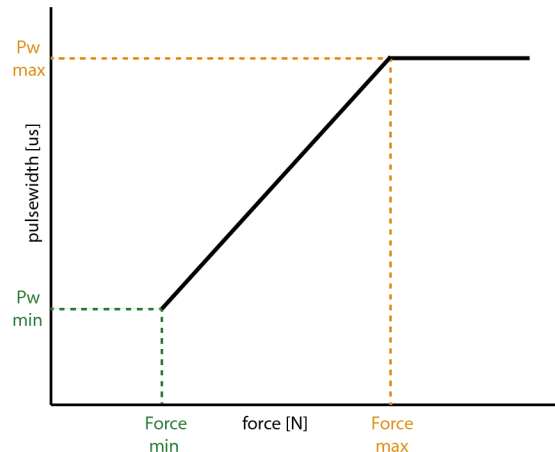
The readouts of three of the insole's force sensors are used to directly drive the electro-tactile stimulation on the stump of the amputee or on the impaired foot of a diabetic patient. Information regarding both the intensity of the pressure applied on the foot sole and the location of this pressure are taken from the sensorized insole and used to drive the stimulator.

This former information is used to provide the subject with an electrotactile stimulation proportional to the applied force. The latter is used to give the patient the information of which part of the foot is touching the ground or an obstacle. Indeed, the electrodes are placed on the stump so that a stimulation on the frontal part of the leg corresponds to a pressure on the toe while a stimulation on the lateral and back part of the stump can be easily associate to a pressure under the central part of the foot and under the heel, respectively (Figure 2.2).



**Figure 2.2:** *Remapped sensation at the amputee's stump*

The algorithm that controls the stimulation is implemented on the ODROID-C2 and is written in C++. The intensity of the stimulation is obtained as a linear mapping of the exerted force (Figure 2.3): a minimum force is required to start the stimulation, and a maximum threshold is set to avoid any painful sensation in the subject. The intensity of the stimulation is modulated in pulsewidth, while the frequency is kept constant at 50Hz and the amplitude at the value predetermined during a calibration phase.



**Figure 2.3:** *Linear mapping between force and stimulation's intensity*

## 2.1 Novelties

One of the most important peculiarities of MYLEG system is its non-invasiveness which overcomes all the issues related to the surgical intervention needed to implant the electrodes and the subsequent rehabilitation. Moreover, MYLEG system is the first non-invasive device to be implemented for transfemoral amputees. Some non-invasive sensory restoration devices have been developed for transtibial amputees by providing a remapped vibrotactile feedback. However, these implementations provide the subject with a sensation which turns on when the applied pressure overcomes a certain threshold. Instead, MYLEG system is able to provide a real-time modulated stimulation. In fact, data are transmitted from the insole to the stimulator with a latency of less than 50 ms to allow the subject to perceive a real-time stimulation that perfectly matches any of his movements. Therefore, the user can use this information to decide and optimize his walking strategy. This is a huge strength of the system. Moreover, the subject receives a stimulation which is modulated both in the location and in the intensity meaning that he is able to discriminate between the frontal, the medium and the back part of his foot and different levels of pressure instead of just knowing if the force is exerted or it is not. Another novelty is of course the high portability of the system which can be worn by the subject while walking both indoors and outdoors as the power and all the electronics are stored into a 3D-printed case and a small fanny bag. Finally but not less important, MYLEG system provides the subject with an information about the proprioception of his knee, producing a stimulation

proportional to the enclosure of the shank angle. This is extremely important for transfemoral amputees to improve balance and walking symmetry.

## 2.2 Achievements

MYLEG system has been already used for assessing improvements in gait with 3 transfemoral amputee subjects in different walking activities: ground-level walking, inclined walking and stair walking. The results show an increase of the overall confidence and trust in the prosthesis as well as their proprioceptive awareness of the prosthetic leg. Moreover, an increased symmetry between the healthy and the prosthetic leg has been demonstrated together with a more physiological distribution of the exerted forces.

## 2.3 Aim of the thesis

Although the system has been already used for experiments and promising results have been shown in restoring sensory feedback, many issues have been encountered during its usage, in particular related to the associated electronics.

First of all, the dimension and weight of the electronic board have been reported by all the amputee subjects as a major limitation of the system. In fact, the object is bulky and disturbs the patient while he is walking. Moreover, the subject is afraid of hitting the device against obstacles during his path. The goal is to develop a compact and lightweight solution so that the patient does not sense the device while performing the activities.

The second major problem is associated with the Bluetooth module embedded into the electronic board that needs to be replaced. In fact, newer versions that use less power and cost less are now available. This would allow to obtain more stable and more reliable connection, higher transmission range and speed improving the communication and transmission of data.

Moreover, the original board is attached to the ankle of the subject and, therefore, it only allows to quantify the swinging of the foot, but does not give the possibility to

get any information about vertical movements. In order to detect them and measure knee flexion two IMUs are necessary. In fact, inertial measurement data can be used to calculate hinge joint angles when at least one IMU is attached to each side of the joint.

Another priority is the possibility to synchronise many devices together. Applying one device on each leg of the patient allows to perform gait analysis in absence of force platforms or 3D motion capture systems by comparing the healthy leg with the prosthetic one.

Lastly, no easy way to reprogram the original board was present. In fact, the box needed to be dismantled in order to access the development board which is present inside. External and easily accessible pins have to be added in order to make the reprogramming process quicker and safer.

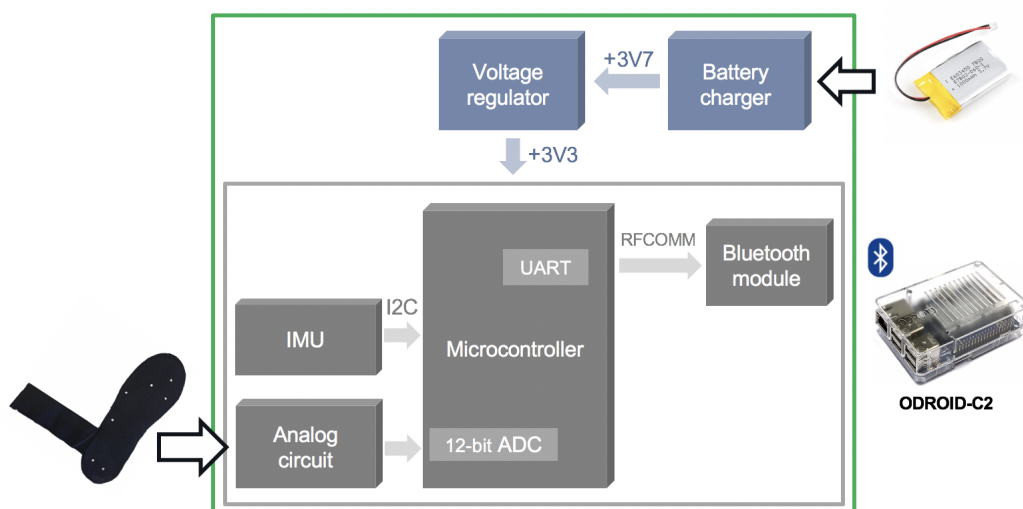
As described before, this master thesis is part of a much wider project developed by the Neuroengineering Lab at ETH Zürich and mainly focuses on the substitution of the electronic board for data acquisition and transmission and its later validation. The primary goal is not only to create a lighter circuit but also to improve the accuracy of the collected data and the communication with the other parts of the system.



# Materials and Methods

In this section, the new circuit that has been developed to acquire data from the custom-made sensorized insole and from an IMU and to transmit them to the system-controller is described pointing out the main changes that have been performed during its design and development in accordance to the aim of the thesis listed in Section 2.3.

## 3.1 Hardware design



**Figure 3.1:** Simplified schematic of the electronic circuit for data acquisition and transmission

A Lithium-ion rechargeable battery provides the input voltage that, after being regu-

larized, powers all the other components. The components used to acquire the data are an analog circuit which conditions the signals coming from the insole's force sensors to obtain a voltage output. These analogue data are converted into digital signals by the ADC integrated in the microcontroller. An Inertial Measurement Unit detects position, linear acceleration and angular rate of the foot and is used to measure the angle of the shank. All these collected data are sent to the system controller via a Bluetooth module and then used to drive the stimulation.

As asserted in Section 2.3, one of the major limitations of the original board was the size and the weight. In fact, it comprised a NUCLEO-103RB development board from STMicroelectronics which was used to control other components which were soldered on a stripboard. The development board and the commercially available modules used to acquire and send the data comprised numerous pins and connections, most of which were not used for the purpose of the device. Therefore, the idea is to embed onto a 2-layers Printed Circuit Board (PCB) only the actually needed parts. The so obtained board has reduced dimensions (55 x 37 x 1.6 mm) and it is very light (approx. 2 g). Moreover, the surface mounted components are smaller than the corresponding through-hole parts and the physical cables have been replaced with wires directly designed onto the PCB. All these changes allow to save space and to obtain a lighter circuit.

### **3.1.1 Power line**

The Polymer Li-ion Rechargeable Battery Pack from RS Pro (RS Pro Article: 1449405) is used to power the circuit. It is tested and approved to UN38.3 and it has internal protection against short circuits, overcharging and overheating. Tests have been applied to guarantee no fire and no explosion under extreme condition. The main specifications about this product can be found in Table 3.1. It is connected to the PCB through a rectangular connector from JST that prevents the detachment.

The MCP73871 Li-Polymer Battery Charge Management Controller from MICROCHIP

**Table 3.1:** Polymer Li-Ion rechargeable battery pack characteristics

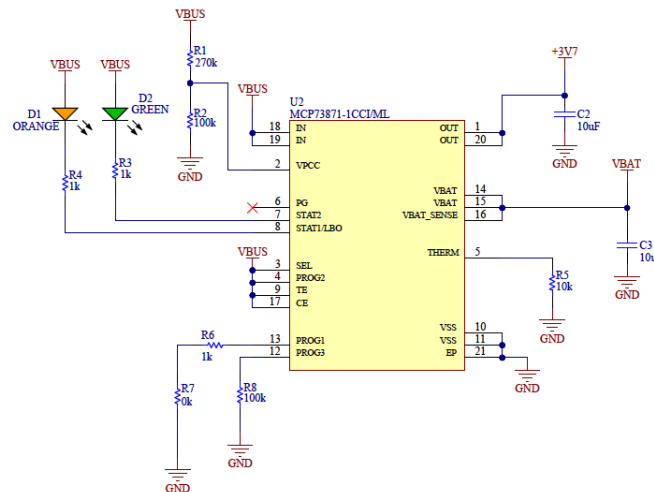
Parameters	Characteristics
Dimensions	53.5 x 35 x 10.4 mm
Nominal Voltage	3.7 V
Limited Charge Voltage	4.2 V
Discharge Cut-off Voltage	3.0 V

is used to recharge the Li-Ion battery when connected to an external plug using the 10118194-0001LF micro USB 2.0 connector from Amphenol ICC.

**Table 3.2:** MCP73871 Li-Polymer Battery Charge Management Controller characteristics

Parameters	Characteristics
Voltage regulation $V_{REG}$	4.1 V
Supply Voltage	$V_{REG} + 0.3 \text{ V}$ to 6 V
Low Battery Detection Threshold	3.2 V
Temperature range	-40 °C to 85 °C
Thermal Resistance	35 °C/W

The MCP73871-1CCI/ML version has been chosen to limit the regulation voltage  $V_{REG}$  at 4.1 V avoiding overcoming the limited charge voltage of the Li-Ion battery. In fact, when the battery voltage reaches  $V_{REG}$ , the battery charger enters in a constant voltage mode. The circuit schematic is shown in Figure 3.2.

**Figure 3.2:** MCP73871 Li-Polymer Battery Charge Management Controller schematic

A voltage divider at pin VPCC (pin 2) is used to reduce the battery charging current whenever the input voltage VBUS at pin IN (pins 18-19) drops below the established

threshold. Considering a  $V_{IN}$  of 5 V, two divider resistors of 100 k $\Omega$  and 270 k $\Omega$  have been chosen to set the Voltage Proportional Charge Control at 1.35 V according to Formula 3.1.

$$V_{VPCC} = \left( \frac{R_2}{R_2 + R_1} \right) * V_{IN} \quad (3.1)$$

Pin SEL (Pin 3) has been set High because a regular 5 V wall adapter is used to charge the Li-Ion battery. Pins CE (pin 17) and TE (pin 9) have been set High to enable device charge and disable internal timer respectively. Two LEDs have been added to signal the battery status. A green LED is connected to pin STAT2 (pin 7) which enters in Low status output when the charge is complete; an orange LED is connected to pin STAT1/LBO (pin 8) which turns into Low status output while the battery is charging. Pin VSS (pins 10-11) is the 0 V reference pin and it has been connected to the negative terminal of the battery (GND).

All the other connections have been design in accordance to the Typical Application Circuit that can be found in the datasheet of the component. In particular, some precautions have been taken into consideration during the placement of the components on the PCB: the battery pack has been placed as close as possible to the device's VBAT and VSS pins to minimize the voltage drop along the high current-carrying PCB traces; pins IN, OUT and VBAT have been bypassed to VSS with a 4.7  $\mu$ F ceramic capacitor. A 10 k $\Omega$  resistor has been placed between pin THERM and VSS to immediately suspend the charge cycle if a voltage outside some predefined thresholds is detected. The MCP73871-1CCI/ML replicates in output the battery voltage VBAT through the pin OUT (pins 1-20) which provides 3.7 V as input to a voltage regulator.

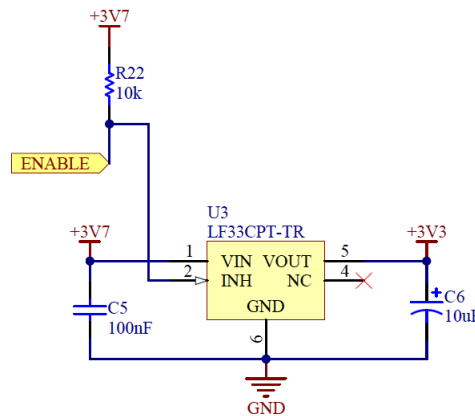
The LF33CPT-TR linear voltage regulator has been chosen to regularize the 3.7 V coming from the battery charger. A voltage regulator generates a fixed and stable output voltage of a pre-set magnitude (3.3 V in this case) that remains constant regardless of changes to its input voltage or load conditions.

The PPAK package consists in a 5 pins component whose schematic is shown in Figure 3.3: pin NC (pin 4) is not connected, pin GND (pin 3) is connected to the negative terminal of the battery, pin VIN (pin 1) is the input pin and receives the 3.7 V from

**Table 3.3:** *LF33CPT-TR Voltage Regulator characteristics*

Parameters	Characteristics
Package	PPAK
Output Voltage	3.3 V
Operating Input Voltage	3.3 V to 16 V
Temperature range	-40 °C to 125 °C

the battery charger, pin VOUT (pin 5) is the output pin and produces a fixed 3.3 V voltage which is used to power the other components of the circuit and pin INH (pin 2) controls the state of the circuit. In fact, it is connected to a switch and a pull-up resistor: when the switch is open, pin INH is driven High and no VOUT is generated meaning that the entire circuit is OFF; whenever the switch is closed, pin INH becomes Low and a 3.3 V output voltage is generated powering up the entire circuit.

**Figure 3.3:** *LF33CPT-TR Voltage Regulator schematic*

One very important aspect to be noticed is that the state of the circuit is controlled at the level of the voltage regulator meaning that the battery can be charged even when the circuit is OFF. A 100 nF ceramic capacitor between pin IN and pin GND and a 10  $\mu$ F electrolytic capacitor between pin OUT and GND have been added to avoid power surges, as suggested in the component's datasheet.

The choice of the component has been made taking into account its maximum power dissipation which is its maximum capability to transfer power loss without overheating. Knowing the thermal resistance junction-ambient  $\Theta_{JA}$ , the maximum operating junction temperature  $T_{JMAX}$  and the ambient temperature  $T_A$ , the maximum power

$P_{D_{MAX}}$  that the device is able to dissipate without overheating can be calculated using Formula 3.2.

$$P_{D_{MAX}} = \frac{T_{J_{MAX}} - T_A}{\Theta_{JA}} \quad (3.2)$$

Knowing that  $\Theta_{JA} = 100 \text{ }^\circ\text{C/W}$ ,  $T_{J_{MAX}} = 125 \text{ }^\circ\text{C}$  and considering an ambient temperature  $T_A$  of  $25 \text{ }^\circ\text{C}$ , the maximum power dissipation  $P_{D_{MAX}}$  is 1 W.

The power dissipation of a linear voltage regulator can be calculated using Formula 3.3.

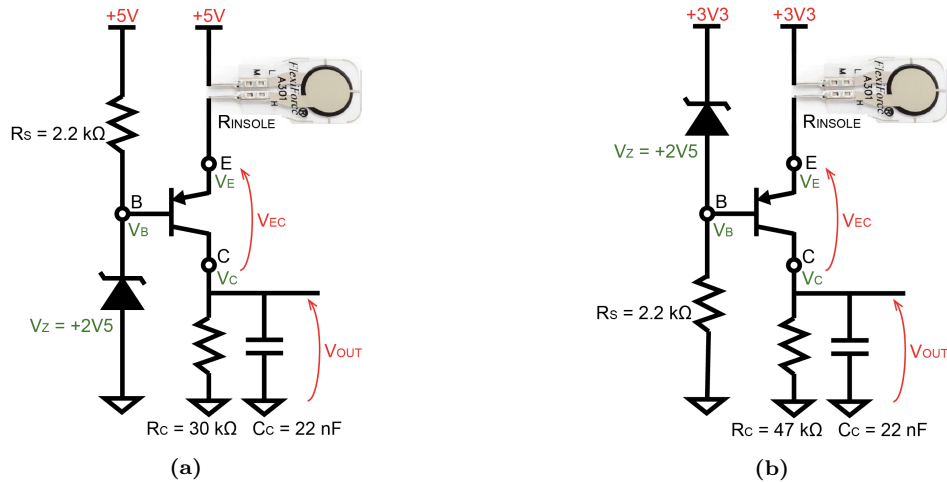
$$P_D = (V_{IN} - V_{OUT}) \cdot I_{OUT} \quad (3.3)$$

Knowing that  $V_{OUT} = 3.3 \text{ V}$  and, considering the worst case scenario,  $V_{IN} = 4.1 \text{ V}$  (i.e. maximum level at which the battery is charged) and  $I_{OUT} = 1 \text{ A}$  (i.e. maximum output current allowed by the component), the maximum reachable power dissipation is 800 mW.

In order to avoid the burning of the component, the actual power dissipation has to remain lower than the maximum computed value. This is verified by the previous calculations. However, a possible increase in the ambient temperature while the circuit is working has to be taken into account. In order not to reduce the maximum power dissipation below 800 mW, the ambient temperature can increase up to  $45 \text{ }^\circ\text{C}$ . This has been verified in the validation phase of the PCB in which no temperature increment has been demonstrated over a 12 hours continuous usage period.

In the original circuit, a  $V_{IN}$  of 5 V was provided to the voltage regulator. In fact, the battery voltage was increased to 5 V by a boost converter and then used to power the analog circuit. To avoid an excessive input voltage to the regulator which would have caused the overcoming of the maximum power dissipation, the boost converter has been removed and all the components have been powered with 3.3 V. The changes that had to be made to the analog circuit due to the reduction of the input voltage are described in Section 3.1.2.

A linear voltage regulator has been chosen instead of a buck converter because it has lower complexity requiring only the regulator and low value bypass capacitors, smaller size since heatsinking is not needed, lower cost and lower ripple and noise.



**Figure 3.4:** (a) analog circuit present in the original board; (b) new circuit designed on the PCB

### 3.1.2 Analog circuit

The analog circuit takes as input the values of the force sensors present in the custom-made sensorized insole and produces in output a corresponding voltage. The insole connector consists of the 61300811121 THT 8-pins male header from Würth Elektronik that perfectly matches the female socket present in the insole. The first pin is connected to 3.3 V while each of the other 7 pins is connected to one of the 7 force sensors embedded in the insole. A301 FlexiForce standard piezoresistive force sensor from Tekscan has been chosen in previous developments. It consists of a variable resistor and, thus, a conditioning circuit in the electronic board is necessary to convert its value from Ohms to Volts.

Numerous modifications to the original analog circuit have been performed since the 5 V voltage output from the boost convert has been removed and the circuit is now powered at 3.3 V. Figure 3.4 shows both the original circuit on the left and the new modified circuit on the right.

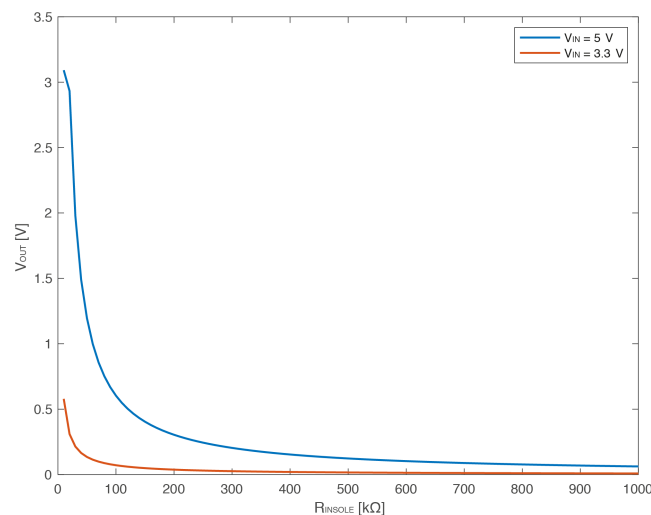
The MMBT3906LT1G General Purpose PNP Transistor from ON Semiconductor has been selected since it has the same electrical characteristics of the one used in the original circuit.

In order to understand the best value for  $R_C$  and  $V_B$ , Multisim software from National Instruments has been used to simulate the behaviour of the analog circuit. Multisim

**Table 3.4:** *MMBT3906LT1G General Purpose PNP Transistor characteristics*

Parameters	Characteristics
Reverse breakdown voltage	2.5 V
Minimum operating current	65 $\mu\text{A}$
Temperature range	-40 °C to 125 °C

software allows to take into account the specifications and the tolerances of each component by specifying its part number or by manually adding them. The behaviour of the original circuit has been taken as reference and a similar or improved performance has been researched. The simulation confirmed that keeping the same values of  $R_C$  and  $V_B$  as per the original board would have drastically reduced the performance of the circuit (Figure 3.5).

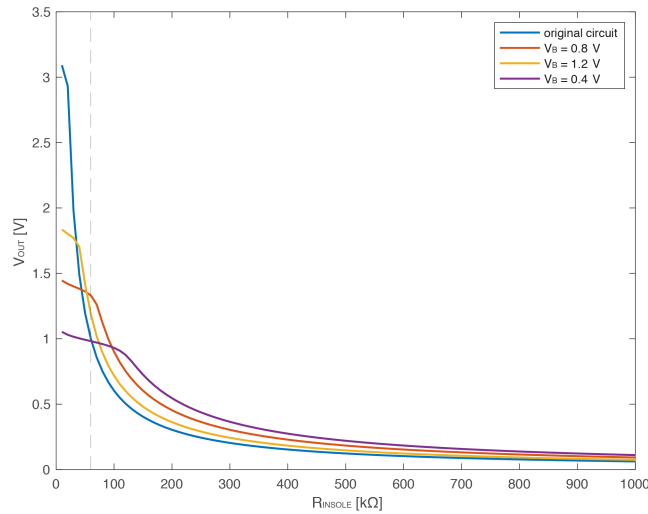


**Figure 3.5:** *Performance comparison between the original analog circuit (blue line) and the one obtained by reducing the input voltage but keeping the same values for  $R_C$  and  $V_B$  (red line)*

One way to get an identical performance to that of the original board would have been to increase  $R_C$  at 200 k $\Omega$ . In fact, by increasing  $R_C$  and considering the same  $R_{\text{INSOLE}}$  value, the voltage drop between the collector and the emitter decreases and the current flowing at the collector pin rises. However, this option has been rejected because the MCU datasheet specifies that the "the external input impedance to the ADC integrated in the microcontroller cannot exceed 50 k $\Omega$  in order to guarantee an error below 1/4 of LSB". Thus,  $R_C$  has been imposed to 47 k $\Omega$  and the analog circuit outcome when reducing the voltage at the base pin has been investigated. The different



trends at different  $V_B$  are shown in Figure 3.6. By reducing  $V_B$ , the range of the output values decreases, and the saturation region enlarges.



**Figure 3.6:** Performance comparison between the original analog circuit (blue line) and those obtained by keeping  $R_C = 47 \text{ k}\Omega$  and decreasing  $V_B$

At this point, understanding the range of values that  $R_{\text{INSOLE}}$  assumes while a person is walking wearing the insole, has been necessary to determine the best value of  $V_B$ . For doing this, data collected from 5 different subjects using the original board has been used. People with different weight and sex have been chosen to consider many different scenarios and 30 steps have been considered. The mean of the maximum digital values has been considered for each patient; it has been converted into the corresponding analog value considering that the ADC integrated in the microcontroller has 12 bits (Formula 3.4) and, using the curve predicted by Multisim simulator, the corresponding value of  $R_{\text{INSOLE}}$  has been calculated which corresponds to the minimum value reached during the walking.

$$\text{max analog value} = \frac{\text{max digital value} * 3.3V}{2^{12}} [V] \quad (3.4)$$

Data are shown in Table 3.5.

Considering an extra margin,  $R_{\text{INSOLE}} = 60 \text{ k}\Omega$  has been considered as the minimum possible value reached during walking. The dotted line in Figure 3.6 shows the lower limit of interest and, it can be easily notice that the red curve ( $V_B = 0.8 \text{ V}$ ) corresponds to the best performance among those considered. In fact, the purple curve

**Table 3.5:** Data collected from 5 subjects (S1-S5) using the original board to understand the range of  $R_{\text{INSOLE}}$  during walking

	S1	S2	S3	S4	S5
Max digital value	422	817	659	250	248
Max analog value [V]	0,34	0,658	0,53	0,201	0,200
Min $R_{\text{INSOLE}}$	170	90	110	300	300

saturates at  $R_{\text{INSOLE}}$  bigger than 60 k $\Omega$  and no changes in the output voltage would be perceivable between 60 and 120 k $\Omega$ ; the yellow curve has a slightly smaller range of output voltages. The fact that only the 45 % of the ADC range is used represents, of course, the bigger limitation of the analog circuit. However, a slightly improvement has been anyway obtained with respect to the original circuit.

In order to obtain a 0.8 V voltage at the base pin of the transistor, a Zener diode with a reverse breakdown voltage of 2.5 V has been used in an inverse configuration with respect to that in the original circuit. The LM4040CIM3-2.5/NOPB Micropower Voltage Reference Diode from Texas Instruments has been chosen because it comes both in THT and SMT packages and the former has been used to test the circuit on a breadboard before the design of the circuit on the PCB.

**Table 3.6:** LM4040CIM3-2.5/NOPB Shunt Voltage Reference characteristics

Parameters	Characteristics
Reverse breakdown voltage	2.5 V
Minimum operating current	65 $\mu\text{A}$
Temperature range	-40 $^{\circ}\text{C}$ to 125 $^{\circ}\text{C}$

An  $R_S$  of 2.2 k $\Omega$  generates a current  $I_S = \frac{3.7V}{2.2k\Omega} = 300\mu\text{A}$  flowing into the cathode of the diode and, since it is higher than its minimum operating current, it guarantees the operation of the component. A voltage of 0.8 V is therefore imposed at the base pin of the transistor.

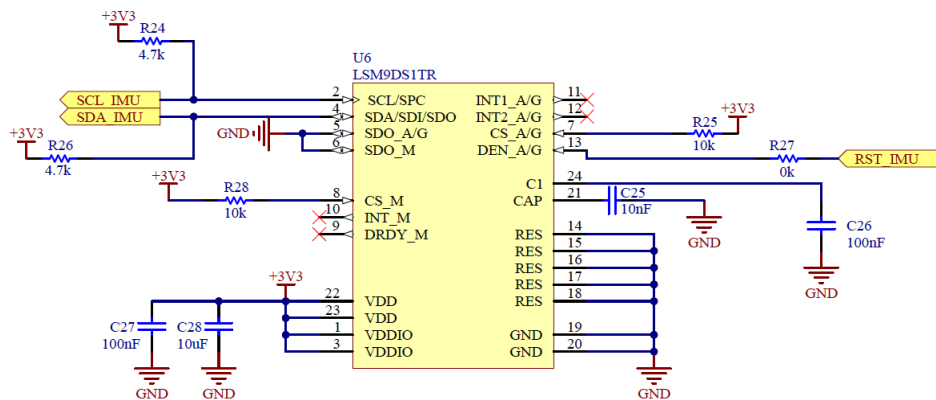
### 3.1.3 Inertial Measurement Unit

An Inertial Measurement Unit (IMU) is embedded into the circuit to detect the position of the foot, its linear acceleration and its angular rate. The LSM9DS1 module from

STMicroelectronics consists of a 3D digital linear accelerometer, a 3D digital gyroscope and a 3D digital magnetometer. The main module specifications are reported in Table 3.7. Inter-Integrated Circuit (I2C) interface is exploited by pulling pins CS\_A/G and CS\_M (pins 7 and 8) High. This protocol creates a synchronous serial communication so it requires two wires to transmit data between devices: Serial Data (SDA) to send and receive data between the master and the slave and Serial Clock (SCL) to carry the clock signal. Pins SDA/SDI/SDO and SCL/SPC (pins 4 and 2) are directly connected to the I2C1\_SDA and I2C1\_SCL pins (pins 62 and 61) of the microcontroller. Both SCL and SDA pins must be connected to 3.3 V through an external pull-up resistor so that, when the bus is free, both the lines are High. All the other connections have been designed as per the example circuit in the datasheet: 100 nF ceramic capacitors have been placed as close as possible to the supply pins of the component for power supply decoupling.

**Table 3.7:** *LSM9DS1 Inertial Measurement Unit characteristics*

Parameters	Characteristics
Supply voltage	1.9 to 3.6 V
Temperature range	-40 °C to 85 °C
Linear acceleration typical zero-g level offset accuracy	$\pm 90$ mg
Angular rate typical zero-rate level	$\pm 30$ dps



**Figure 3.7:** *LSM9DS1 Inertial Measurement Unit schematic*

### 3.1.4 Bluetooth module

After data has been collected from the insole and the IMU, they are sent to the system controller via Bluetooth to drive the stimulation. An old 2.1 version Bluetooth module was present on the original board, so it has been replaced with a newer version. The different components that have been compared before taking the final decision are shown in Table 3.8 in which all the main characteristics that have driven the choice are reported.

**Table 3.8:** Comparison between different possible Bluetooth modules

<b>Part Number</b>	RN41-I/RM	RN4678-V/RM100	RN4020-V/RM	NINA-B2222
<b>Mode</b>	BR/EDR	BR/EDR, BLE	BLE	BR/BDR, BLE
<b>Version</b>	2.1	5.0	4.1	4.2
<b>V<sub>IN</sub></b>	3.0 to 3.6 V	3.3 to 4.2 V	1.8 to 3.6 V	3.0 to 3.6 V
<b>Max operating temperature</b>	+ 85 °C	+ 70 °C	+ 85 °C	+ 85 °C
<b>Transmit power</b>	16.5 dBm	1.5 dBm	7.5 dBm	8 dBm
<b>Data rate</b>	300 Kbps	1 Mbps	1 Mbps	1 Mbps
<b>Antenna type</b>	integrated	integrated	PCB	integrated
<b>Sensitivity</b>	- 80 dbm	- 90 dBm	- 92.5 dBm	- 88 dBm
<b>Interfaces</b>	UART	UART	AIO, GPIO, SPI, UART	UART, GPIO
<b>RFCOMM</b>	yes	yes	no	yes

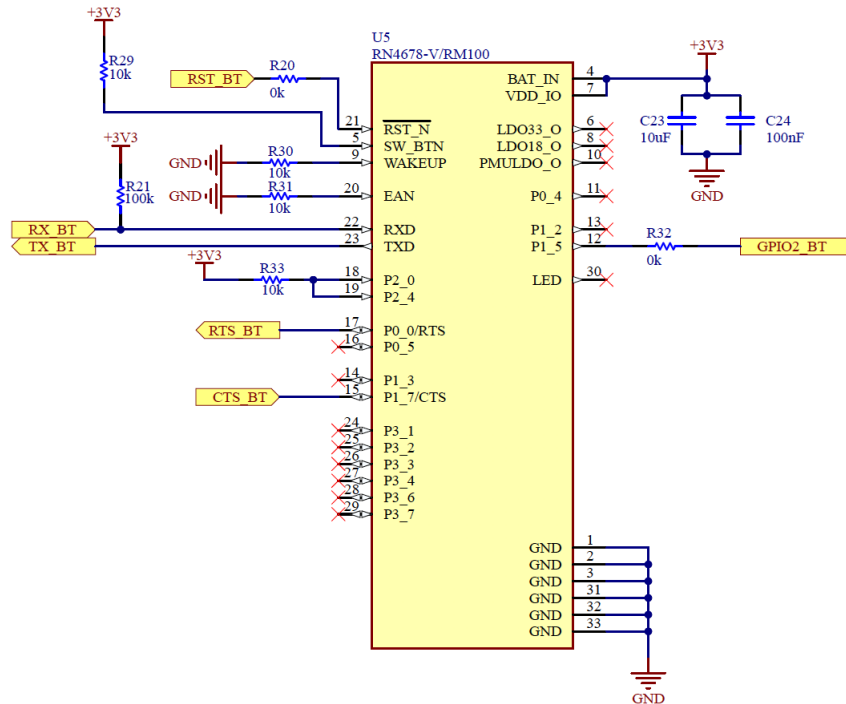
original module

new module

A Bluetooth v5.0 dual mode module has been chosen with respect to the 2.1 version of the previous component. Another characteristic that has been taken into account is the transmit power. The higher the transmit power, the longer the effective range but the higher the power consumption of your device. In the considered scenario, a reduced range is sufficient because the electronic board, placed at the ankle of the subject, and the system-controller, inserted into the fanny bag at the hip, are approximately 1 m apart. Instead, it is very important to reduce the power consumption of the system, thus a module with a lower transmit power has been chosen. The sensi-

tivity is the measure of the minimum signal strength a receiver can interpret, i.e. the lowest power level at which the receiver can detect a radio signal, maintain a connection, and still demodulate the data. The chosen module has a much higher receiver sensitivity with respect to the original one. The presence of the Radio Frequency COMMunication (RFCOMM) protocol was an initial requirement in order to maintain the same communication protocol with the system controller. RFCOMM is a simple transport protocol, which provides emulation of RS232 serial ports over the L2CAP protocol. The RN4678-V/RM100 supports the RFCOMM protocol in the BR/EDR Classic mode together with Serial Port Profile (SPP). BLE technology provides different services to emulate serial connections such as Transparent UART which is a private Generic Attribute Profile (GATT) service for serial data transfer between two BLE devices. This is not applicable to the considered circuit because the Bluetooth dongle attached to the system controller does not present the Low Energy operation mode.

Figure 3.8 shows the schematic of the Bluetooth module. The module is integrated with the microcontroller using a UART interface. Only two wires are needed to transmit data between two devices. Data flows from the Tx pin of the transmitting UART to the Rx pin of the receiving UART. This is why the RXD and TXD pins (pins 22 and 23) of the Bluetooth module have been directly connected to the TX and RX pins (pins 43 and 42) of the microcontroller respectively. Similarly, pins CTS and RTS (pins 15 and 17) have been connected to pins RTS and CTS (pins 44 and 45) of the microcontroller. These pins are used to enable the communication; in fact, the microcontroller has to set the CTS pin of the Bluetooth module Low to enable the transmission of data to the system controller. The module's CTS pin must be pulled high to pause the data flow. Pin SW\_BT (pin 5) pin WAKEUP (pin 9) have been set High and Low respectively to prevent the module to turn OFF or going into sleep mode. Imposing pins P2\_0, P2\_4 (pins 18 and 19) to High and pin EAN (pin 20) to Low sets the module in Operating mode. The status of pin P1\_5 (pin 12) can be read from the microcontroller to see if the module is connected to peer device (active low).



**Figure 3.8:** RN4678-V/RM100 Bluetooth Dual Mode Module schematic

### 3.1.5 Microcontroller

The same microcontroller which was present on the Nucleo development board (NUCLEO-F103RB) in the original board has been integrated into the circuit. It is the STM32F103RBT6 medium-density performance line ARM-based MCU from STMicroelectronics.

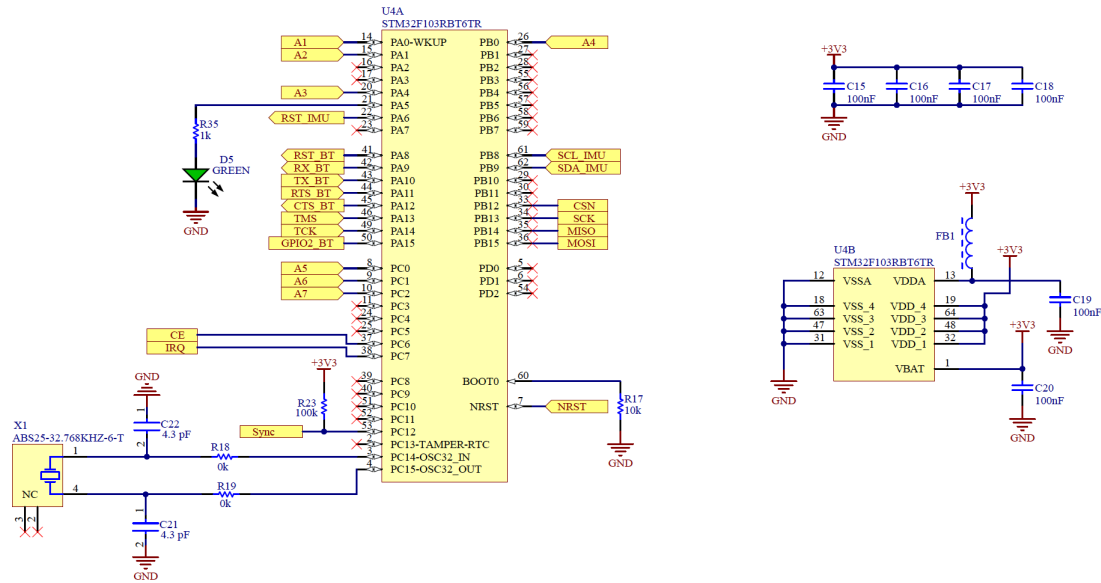
**Table 3.9:** STM32F103RBT6 medium-density performance line ARM-based MCU characteristics

Parameters	Characteristics
Package	LQFP64
Operating voltage	2 to 3.6 V
Temperature range	-40 °C to 125 °C
Number of 12-bit ADCs	2
Communication interfaces	I2C, SPI, UART, USB and CAN

The analog circuit output pins are connected to the 12-bit ADC (pins 8-10, 14-15, 20, 26), the Bluetooth module occupies one of the UART internal circuit (pins 41-45), the IMU is connected to SCL and SDA pins (pins 61-62). A green LED is attached to pin 21 and it is used as a general debugging LED while a blue LED is directly connected to 3.3 V and turns on whenever the circuit is powered. A ferrite board attached to pin 13 is used as low-pass filter to absorb high frequency noise currents and dissipate it as

heat.

Pins 33-36 and 37-38 are connected to a transceiver that will be introduced in Section 3.3, pins 7, 46 and 49 are used for reprogramming the microcontroller (see Section 3.4) while pin 53 is used for synchronisation between multiple devices (see Section 4.3.1).

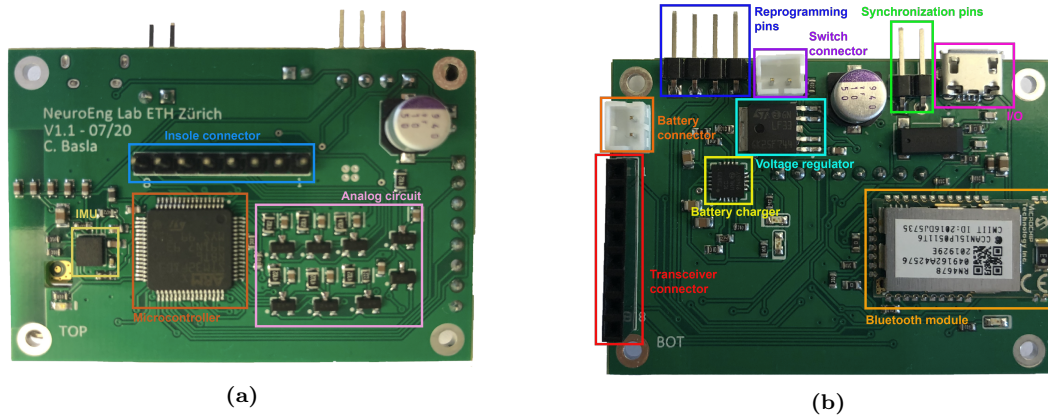


**Figure 3.9:** *STM32F103RBT6 medium-density performance line ARM-based MCU schematic*

## 3.2 PCB design

Figure 3.10 shows the final 2-layers PCB in which the main components have been highlighted. The PCB have been designed using Altium Designer 20.0.12 software. Because of space arrangement, the MCU and the components for data acquisition (insole connector, IMU and analog circuit) have been placed on the top layer of the PCB; power line components and the Bluetooth module have been embedded on the bottom layer. The position for battery and switch connectors, USB connector and external pins has been chosen to best fit the positioning of the board into a 3D printed box.

Footprints of the components have been taken from already existing libraries that have been downloaded from SnapEDA, a leading electronics design search engine that provides free symbols, footprints and 3D models for PCB design. Table 3.10 shows the Design Rules that define the requirements that the design has to follow. They



**Figure 3.10:** (a) top and (b) bottom layers of the designed PCB for data acquisition and transmission

cover every aspect of the design, such as routing widths, clearances, plane connection styles, routing via styles, and not met requirements can be monitored in the Design Rule Checker (DRC). Both designed rules for the entire board and for specific classes of nets have been imposed. Before finalizing the PCB, it has been verified that all the imposed rules respect the manufacturer’s PCB printing capabilities.

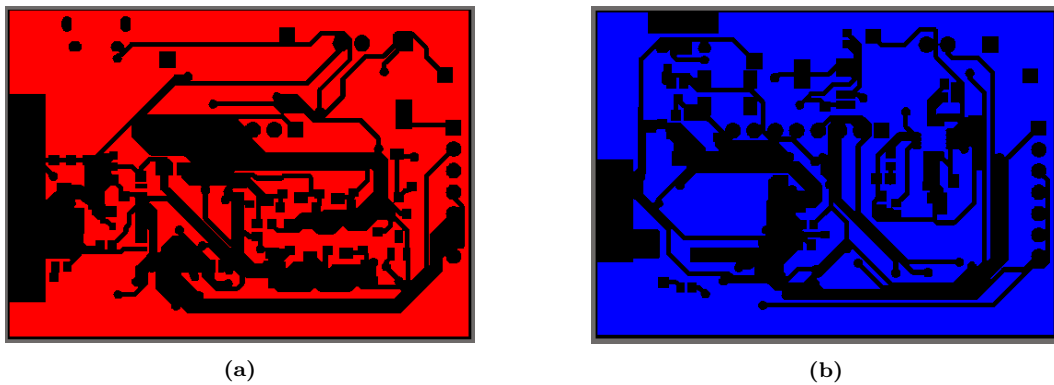
**Table 3.10:** Design Rules imposed in Altium designer

Rules	Constraints
Minimum electrical clearance	0.152 mm
Routing width	0.2 to 0.254 mm
Routing topology	Shortest
Routing corners	45 Degrees
Maximum routing vias diameter	1.3 mm
Solder mask expansion	0.102 mm
Past mask expansion	0 mm
Plane connect	Relief connect
Plane clearance	0.508 mm
Polygon connect	Direct connect
Hole size	0.3 to 3 mm
Hole to hole clearance	0.25 mm
Minimum solder mask silver	0.016 mm

Components have been placed so to minimize the length of the traces between them; in order to do so, vias between the two layers have been used. Whenever available, specifications in the components’ datasheet have been followed for their placement on the PCB layers.



A ground plane that connects all the GND pins of all the components has been poured on both layers. The ground plane is used to reduce the resistance of the return path by avoiding connecting ground pins with ordinary traces which actually are low-value resistors and can affect the functionality of a circuit. By reducing the resistance, it is possible to reduce the voltage drops between physically separated portions of the PCB. A single ground plane has been created by connecting it using GND-vias; extra vias have been added to make the GND plane lower in resistance and help minimizing cross talk. GND pour polygons are shown in Figure 3.11.

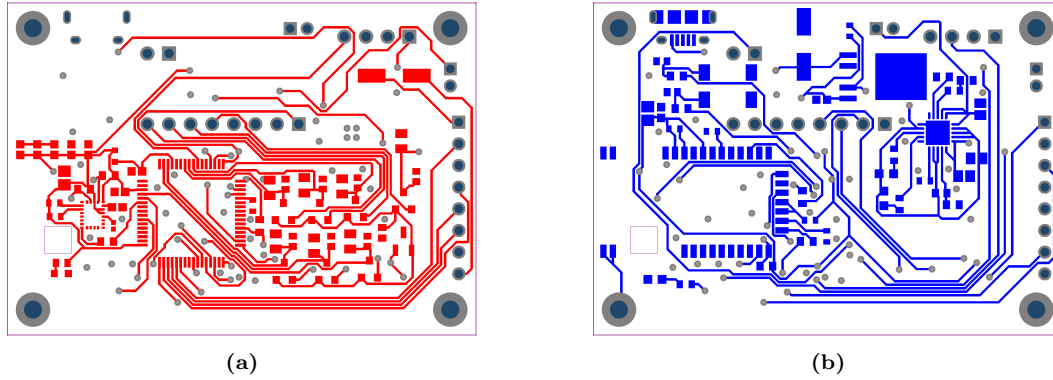


**Figure 3.11:** (a) top and (b) bottom GND planes

Thermal bridges have been avoided by directly connecting pads and vias to the poured polygon; dead copper not connected to any net has been avoided by moving the traces closer, whenever possible, or adding extra GND vias; finally, the components have been moved on the PCB in order to increase as much as possible the area of the polygon. Figure 3.12 shows the pads of the different components and the traces connecting them.

Another shrewdness that has been taken into account was the removal of tracks directly routing IC pads so that the soldering is more defined and short circuit are avoided. Moreover, no traces have been wired in the portion under the Bluetooth antenna as required in the component datasheet.

Some changes have been performed to the downloaded footprint. For example, too small solder masks between IC pads have been removed because they could not be produced. This has been done by placing a solder mask rectangle over the small pads



**Figure 3.12:** (a) top and (b) bottom traces, pads and vias

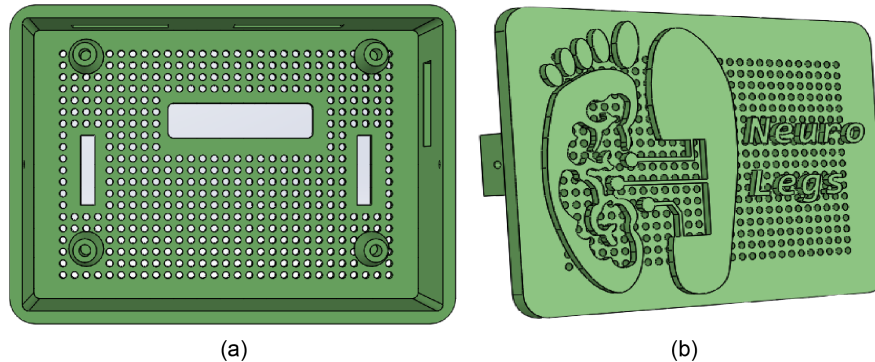
to connect the single small masks into one big area.

After the design finalization, the Gerber files have been downloaded from Altium Designer and sent to a German company, MULTI-CB, for printing. Two PCBs have been requested together with the SMD stencil for manual assembly. All the components have been purchased as described in the bill of materials (see Appendix B). After positioning the stencil over the PCB to perfectly match the pads, a thin layer of solder paste has been spread over the entire surface and all the components have been manually placed in the correct spot under the microscope. The ProtoFlow E reflow oven from LPKF Laser & Electronics was used for lead-free (ROHS) soldering of the PCB. The temperature profiles used during the reflow process are listed in Table 3.11. Component's datasheet has been checked to avoid exceeding the maximum recommended temperature. The same process was repeated for both the layers starting from the TOP layer since the Bluetooth datasheet suggests exposing the module to only one flow.

**Table 3.11:** Reflow process temperature profile

Step	Temperature [°C]	Time [s]
Warm up	160	
Preheat	160	20
Step 1	185	90
Step 2	227	60
Reflow	260	80
Cool time (open the oven)		90

A 3D printed case has been designed using SOLIDWORKS to enclosure the PCB, the battery and the transceiver. This allows for an easier and faster device setup, it protects the circuit from unwanted shocks that could break the electronics and avoids the presence of exposed parts preventing the subject from touching them. The case is composed of a 70 x 55 x 32 mm box and a 2 mm thick cover as shown in Figure 3.13. Internal supports have been designed to directly fix the PCB using self-tapping screws and holes were introduced to access the PCB external pins and connectors and for hosting the switch. Adobe Illustrator has been used for drawing the NeuroLegs logo that has been subsequently imported and extruded over the upper face of the lid.

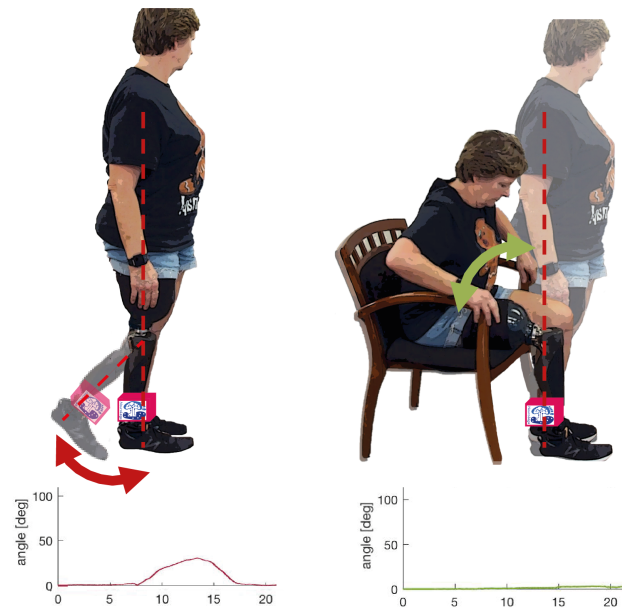


**Figure 3.13:** (a) 3D printed case and (b) cover designed in SOLIDWORKS to accommodate the electronic board

### 3.3 Extra IMU

As already introduced in Section 2.3, one limitation of the original circuit was the possibility to only measure the shank angle. This allows to quantify the swinging of the foot but does not allow to get information about any vertical movement or activity in which the ankle remains still. Figure 3.14 shows some common activities and the corresponding angle variation captured by the original circuit. An accurate angle is measured when the foot is moved back and forth, but a null angle is estimated for stand to sit activity because the board does not detect any acceleration.

This problem has been solved by attaching an IMU to the thigh of the patient. In fact, inertial measurement data can be used to calculate hinge joint angles when at least one IMU is attached to each side of the joint. This allows to properly estimate the knee

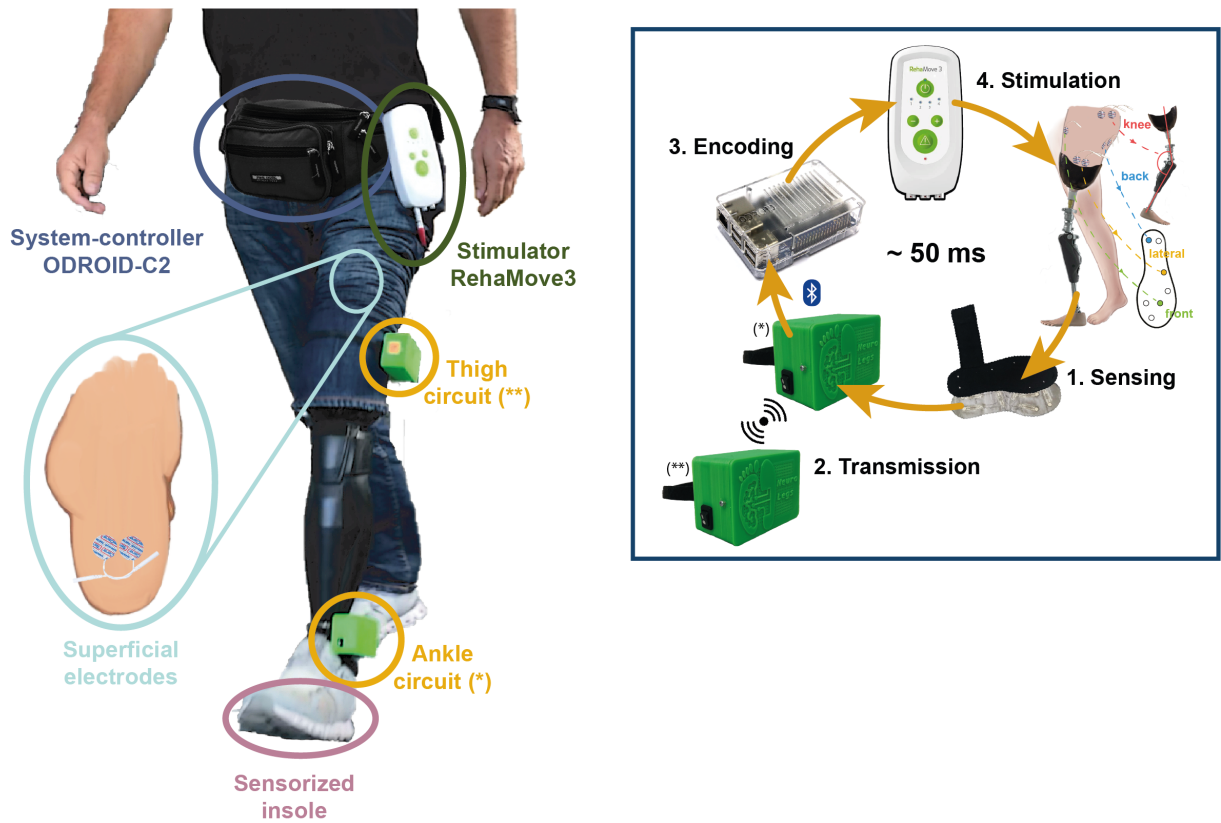


**Figure 3.14:** Angle measured by the original board while performing different activities

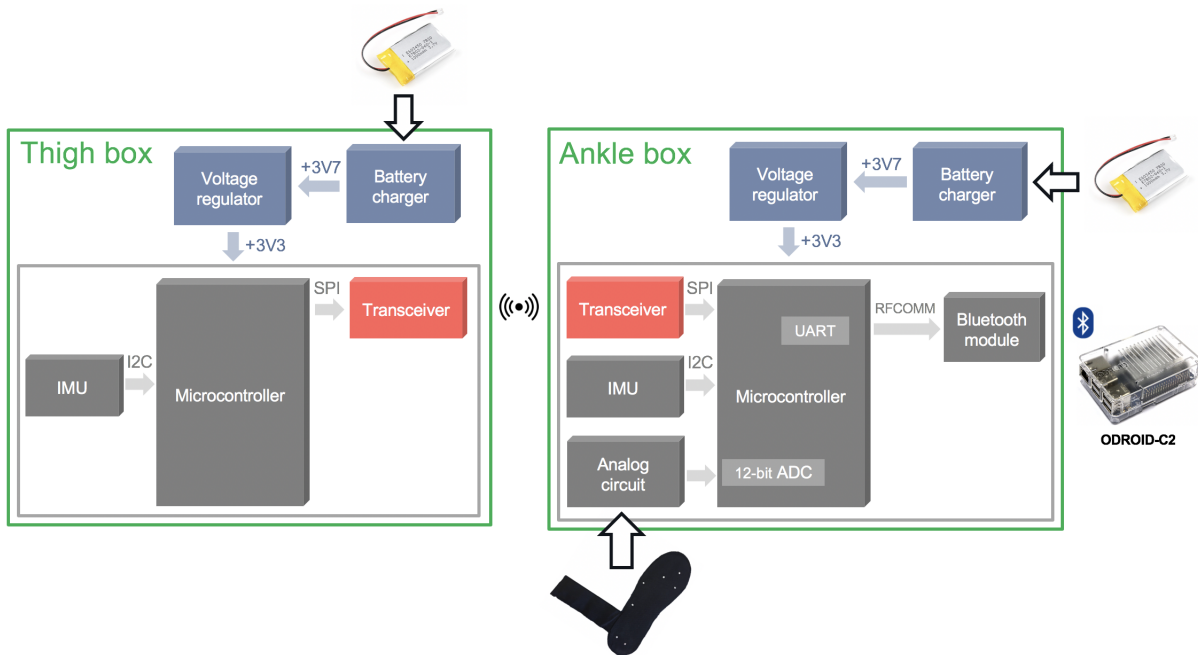
angle which is an information that transfemoral amputees are missing. Knowing if the prosthesis is straight or bent and understanding how much the knee is flexed helps the patient in improving his walking pattern but also in relying more on the prosthesis without the necessity of a continuous visual check of its position.

Another PCB has been developed for this purpose; its design is very similar to that of the ankle PCB but simpler. In fact, it comprises the power line (battery, battery charger and voltage regulator) that provides the 3.3 V input to the MCU and to the IMU embedded on the PCB. The exactly same components have been used when designing this PCB, so refer to Section 3.1 for the schematic and the electrical characteristics of the components. Moreover, the principle of functioning and the protocols of communication are identical to that of the other PCB.

Figure 3.15 shows the updated general description of MYLEG device after introducing the new electronic circuit at the thigh level, while the updated schematic of the two circuits is represented in Figure 3.16.

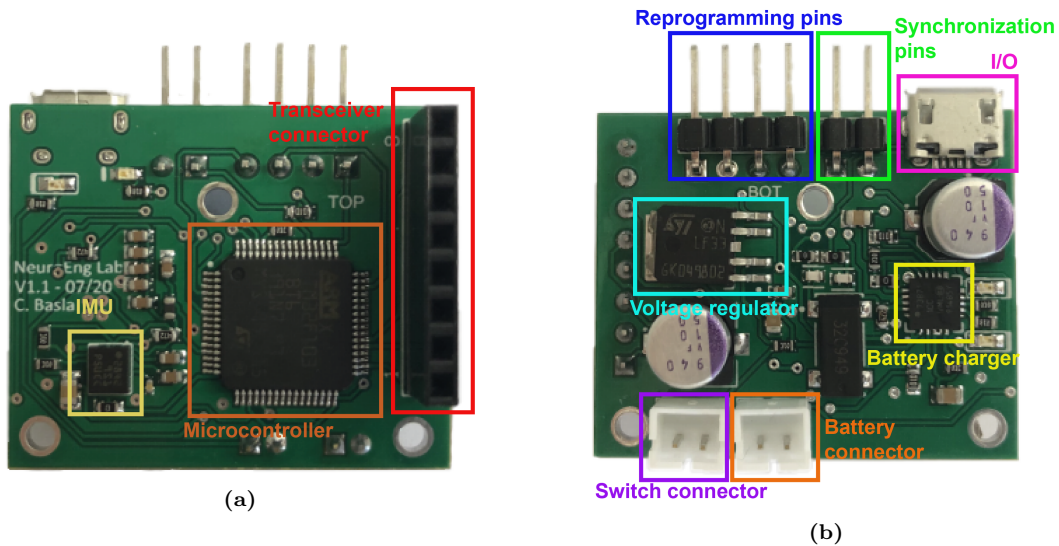


**Figure 3.15:** Updated description of the MYLEG system after introducing a new electronic circuit at the thigh level



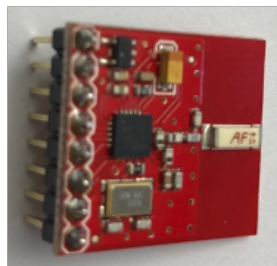
**Figure 3.16:** Updated schematic after introducing a new IMU on the thigh of the patient for a more accurate estimate of the knee angle

Figure 3.17 highlights the main components of the thigh PCB. Due to the reduced number of embedded parts, the size of the second PCB is smaller than the first one (34 x 28 x 1.6 mm).



**Figure 3.17:** (a) top and (b) bottom thigh PCB

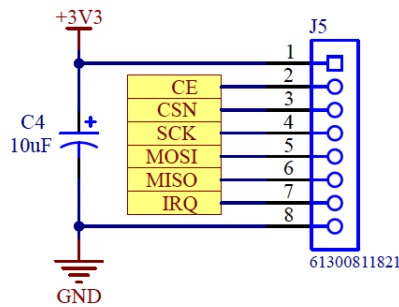
In order for the two PCBs to communicate, the nRF24L01 transceiver from Nordic Semiconductor has been used. Since it requires an external antenna and it would have been extremely complicated to design the antenna circuit directly on the PCB, the already available Transceiver Breakout - nRF24L01+ from Sparkfun (Figure 3.18) has been used.



**Figure 3.18:** 2.4 GHz Transceiver Breakout - nRF24L01+ from Sparkfun

The Sparkfun module comprises an on-board ceramic Antenna and installs a communication over the 2.4 GHz worldwide ISM frequency band which is the band reserved for unlicensed low-powered devices. It is an inexpensive yet reliable 2-way RF solutions, able to both transmit and receive data through the Serial Peripheral Interface (SPI)

protocol. SPI installs a master-slave relationship between the devices (in the considered circuit, the ankle PCB is the master and the thigh PCB is the slave) and requires 4 pins to properly work: MOSI (Master Output/Slave Input) through which the master sends data to the slave, MISO (Master Input/Slave Output) through which the slave sends data to the master, CLK which is the clock line and SS/CS (Slave Select/Chip Select) through which the master selects the slave to send data to. These pins are connected to the corresponding pins in the microcontroller (pins 33-36). Moreover, pin VCC is connected to the 3.3 V provided by the voltage regulator, GND is connected to the ground plane while pins CSN and CE can be connected to any digital pin of the microcontroller (in the circuit, pins 37 and 38). The transceiver schematic is shown in Figure 3.19 while the corresponding connections in the microcontroller can be seen in Figure 3.9.



**Figure 3.19:** 2.4 GHz Transceiver Breakout - nRF24L01+ schematic

The main electrical characteristics of the module are shown in Table 3.12.

**Table 3.12:** 2.4 GHz Transceiver Breakout - nRF24L01+ characteristics

Rules	Constraints
Frequency range	2400 to 2525 MHz
Data Rate	250 kbps, 1 Mbps, or 2 Mbps
Output Power	0 dBm, -6 dBm, -12 dBm or -18 dBm
Operating Supply Voltage	1.9 V to 3.6 V
Maximum Operating Current	13.5 mA
Communication Range	>100 m

Each transceiver communicates at a certain frequency, called channel. In order for two transceivers to communicate together, they have to transmit and receive data over the same channel. Multiple channels are necessary in order to create a unique association

between one ankle PCB and one thigh PCB. This allows for multiple devices (ankle PCB + thigh PCB) to be used simultaneously. In the nRF24L01 transceiver, each channel has a bandwidth of approximately 1 MHz so 125 channels can be set up for communicating at the same time. Among all these 125 channels, it is recommended to use the highest frequencies (2500 - 2525 MHz) to avoid noise from the external environment or other electronics. In particular, WiFi and Bluetooth are used during the functioning of the device and both these technologies use the lower frequencies to communicate (2400 - 2480 MHz).

The electrical specifications are imposed via software. A data rate of 250 kbps has been chosen since it is associated to a higher receiver sensitivity (-94 dBm) compared to the -82 dBm at 2 Mbps. This allows the receiver to decode a signal that is 10 times weaker. In addition, the output power has been set to 0 dBm to increase the strength of the signal.

Finally, the module is very sensible to the noise generated by the power supply. Even small ripples can deteriorate both the quality and the range of the signal. To solve this problem, a 10  $\mu$ F electrolytic capacitance has been placed on the PCB as close as possible to the VCC pin of the transceiver.

### 3.3.1 Knee angle algorithm

The algorithm for calculating the knee angle has been developed. Acceleration and angular rate are extracted for the two IMUs of the device and bound together using a complementary filter.

Each box provides the acceleration and the angular rate in 3 mutually perpendicular axes. It is important to place the electronic boards correctly around the patient's legs to obtain an accurate knee angle estimate since it is calculated as 2D angle over the sagittal plane. In particular, the two boxes have to be placed on the lateral, external part of the leg as aligned as possible. Moreover, both boxes have to be positioned with the z-axis in the mediolateral direction, the x-axis in the anteroposterior direction and the y-axis in the longitudinal direction [36]. Marks on the 3D case in which the PCB is collocated indicate its correct orientation. The correct positioning is shown in Figure 3.20.





**Figure 3.20:** *Correct positioning of the electronic boards around the patient's leg*

Since the local coordinate axes of the IMUs are independent and not aligned with any external meaningful axis [37], an initial calibration has to be performed in order to understand the relative position of the two IMUs. This can be done with static postures and/or calibration movements [37]. In the considered algorithm, the former method has been implemented. The subject is required to stand still with his legs straight for the first 3 seconds after the software booting. In this way, the relative angle between the two IMUs is calculated and used as an offset for the calculation of the knee angle. In fact, it is subtracted to any of the subsequent estimated angles.

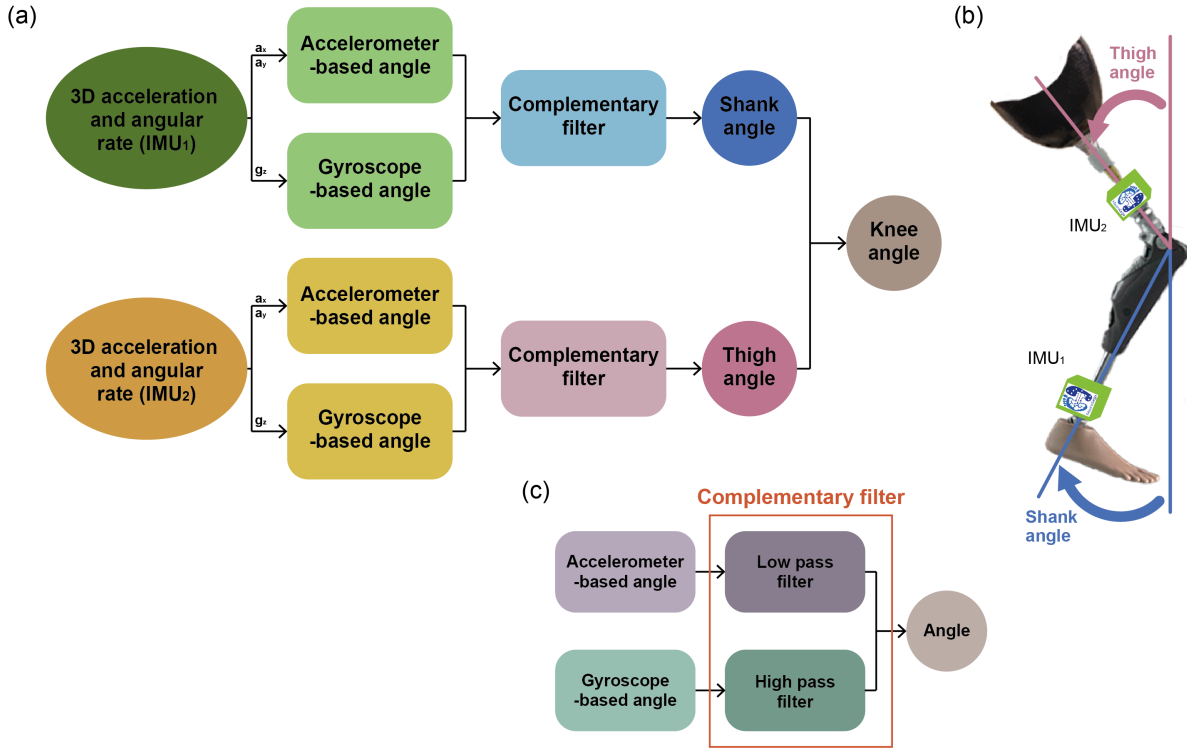
The implemented algorithm is illustrated in Figure 3.21.

The shank and the thigh angle as per Figure 3.21 (b) are calculated separately and then summed together to get the total knee angle.

For each of these two angles, accelerometer and gyroscope data are used individually. The angle from the accelerometer can be calculated considering the two acceleration on the sagittal plane (xy-plane) via a trigonometric calculation (Equation 3.5) [20]:

$$\theta_{acc}(t) = atan\left(\frac{a_y(t)}{a_x(t)}\right) \quad (3.5)$$

where  $a_y$  and  $a_x$  are the linear acceleration along the y- and x-axis respectively.



**Figure 3.21:** (a) knee angle algorithm; (b) shank and thigh angle calculated by the boards; (c) complementary filter

The same angle can be calculated using the gyroscope data with Equation 3.6 through a single integral of the angular velocity around the axis of rotation of the joint.

$$\theta_{gyr}(t) = \int_0^t g_z(\tau) d\tau \quad (3.6)$$

where  $g_z$  is the angular rate around the z-axis.

The single angles are then combined into a complementary filter (Figure 3.21 (c)).

$$\theta(t) = \alpha\theta_{gyr}(t) + (1 - \alpha)\theta_{acc}(t) \quad (3.7)$$

The filter applies a low-pass filter to the accelerometer data since they are affected by high-frequency noise and a high-pass filter to the gyroscope data in order to remove the low-frequency drift that accumulates over time.

Its time constant  $\tau$  can be calculated as

$$\tau = \frac{\alpha\Delta T}{1 - \alpha} \quad (3.8)$$

where  $\Delta T$  is the sampling time and  $\alpha$  is the filter coefficient. The filter coefficient  $\alpha$  has been chosen empirically in order to maximize the accuracy in the angle estimation performing a series of experiments in which the two electronic boards were moved by a well-known angle [38]. The obtained value is then kept fix for any further calculations. After several attempts, a filter coefficient  $\alpha$  of 0.98 has been selected, which correspond to a time constant  $\tau$  of 0.98 s considering  $\Delta T = 0.02$  s. The time constant  $\tau$  gives an indication on how much the algorithm relies on the gyroscope data and how much it relies on the accelerometer data. In particular, for data faster than the time constant, higher weight is associated with the gyroscope angle; on the contrary, the accelerometer angle plays a bigger role when the data changes slower [20]. In fact, the low-pass filter leaves unaltered the signals which are longer than the time constant while the high pass-filter filters them out. This means that gyroscope data are used in the short term while, on the long term, the estimation relies more on the accelerometer data.

Data from the magnetometer have been excluded from the calculation because they can suffer from external magnetic noise. In doing this, Seel and colleagues [37] got an equally accurate result.

Another method for calculating the knee angle would have been to apply a Kalman filter. It is based on a recursive model that searches for the best estimate of its variables using a series of measurements observed over time. Theoretically, it should be more accurate in predicting the angle than the complementary filter. This higher accuracy is however associated with a much higher computational cost due to the high complexity of the implementation that requires to tune multiple variables to converge into a very accurate result. Therefore, a very powerful microcontroller would be needed to run the algorithm. This has been avoided using the complementary filter which, as seen before, is very easy to develop and requires to control only one parameter (the filter coefficient  $\alpha$ ). Numerous papers have shown that the complementary filter is equally accurate in estimating joint angles. Gui et al. [39] calculated tilting measurements using Micro-Electro-Mechanical-System (MEMS) based IMU and obtained smooth and accurate enough results with both the filters either in static or dynamic tests. Another example

is Akintade and colleagues [40], which assesses that complementary filter estimation is highly repeatable and, therefore, suitable for joint angle tracking.

## 3.4 Reprogramming

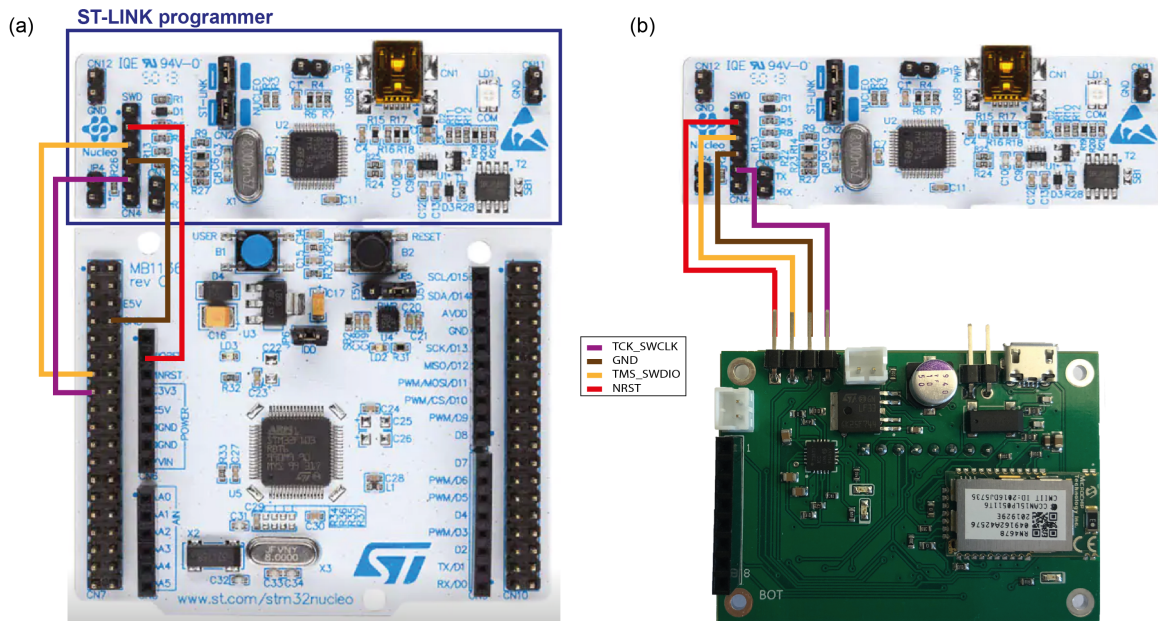
A feature that was missing in the original board is the possibility to easily and quickly reprogram its microcontroller. In fact, every time, the 3D printed box that encases the circuit had to be taken apart in order to directly access the NUCLEO-F103RB pins. Having some pins that come out of the box is pretty useful, in particular during the debugging and test of the device during which changes are continuously made to the code uploaded on the microcontroller of the boards.

The NUCLEO-F103RB development board integrates the ST-LINK debugger/programmer which can be detached from the main part of the board and used for programming the microcontroller (Figure 3.22 (a)). It can be connected to the laptop using a USB A-Male to Mini-B cable. 4 pins of the ST-LINK programmer have to be connected to the corresponding 4 pins of the NUCLEO-F103RB board as shown in Figure 3.22 (a). The connections have been found in the NUCLEO-F103RB user manual [41].

- NRST = reset
- GND
- TMS = Test Mode Select
- TCK = Test Clock

The same connections have been reproduced on the PCB bottom layer. The pins of the microcontroller (pins 7, 46 and 49; see Figure 3.9) are connected to a 4-pins male header that comes out of the board (Figure 3.22 (b)).

Figure 3.23 shows the on-purpose made cable that has been created to connect the PCB to the ST-LINK debugger/programmer using 2 4-pins female sockets.

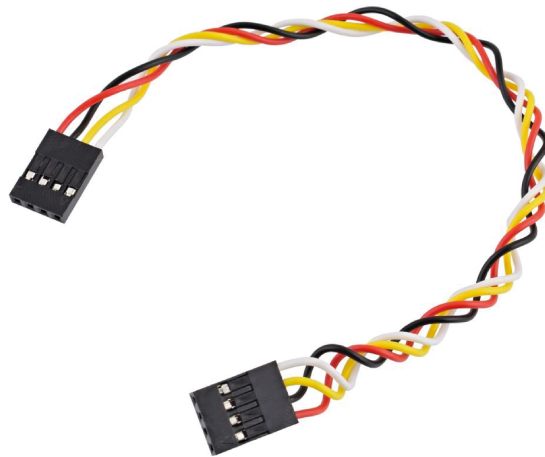


**Figure 3.22:** (a) original board reprogramming method; (b) new reprogramming method through externally accessible pins

### 3.5 Synchronisation

Being able to synchronize multiple devices together is fundamental for the purpose of the device. If performing experiments in a gait analysis laboratory, where force platforms and 3D capture motion systems track the movements of the subject, the walking pattern of the subject can be analysed to assess its nature and its main features (i.e. symmetry, step length, width and height, applied load, cadence). However, this cannot be done when MYLEG device is used outdoor or at home. This is the main reason why the possibility to synchronize multiple devices is a huge priority for the system. In fact, by applying one device on each leg of the patient, it is possible to compare the force distribution and joint angle values between the healthy and the prosthetic leg detecting abnormalities in the walking pattern. It is important to underline that the synchronization process is used for data post-processing and it is not necessary for the success of the experiment and does not bring any benefit to the patient, since each of the devices runs independently.

Different methods of synchronisation have been investigated; in particular, synchronisation via cable and wireless synchronisation have been considered.



**Figure 3.23:** *On-purpose made cable to connect the PCB to the ST-LINK programmer*

Synchronization via cable requires to connect the two devices via cable before the beginning of the experiment and send a synchronization packet from one board to the other one. This method is easily implementable since it just requires some external pins to connect the cable; moreover, the two devices are very close to each other while performing the synchronization and, thus, the propagation time of the packet can be considered negligible due to the extremely short distance; in addition, the physical connection of the cable make the synchronization highly reliable. One drawback of this method could be the extra time required to set up the cable but, for sure, the bigger disadvantage is the impossibility to deal with the clock drift between the microcontrollers of the two devices. The clock drift is the time delay that accumulates over time due to a slightly different timing of the two microcontrollers due to the inaccuracy of their internal oscillators. Since the cable cannot remain connected while the patient is walking, the synchronization byte can be only sent at the beginning of the experiment and no information can be obtained about the accumulated delay. This is instead one of the advantages of the wireless synchronization. In fact, if the two PCBs are connected wirelessly, periodic update packets can be sent making the delay that accumulates between two subsequent synchronization packets' transmission negligible. The other advantage is the fact that no setup is needed. On the other hand, wireless communication is less reliable since it could be disturbed by external sources of noise causing packet loss and it requires a non-negligible time to send the packets which introduces delay. In particular, the main source of error is associated

to the uncertainty in the communication latency and various broadcast modalities try to deal with it differently. The first example is unidirectional broadcast in which the sender transmits a synchronization packet to the receiver containing the time  $T_0$  at which the packet was sent. It is a one-way communication between the nodes which only requires to exchange one packet but does not consider the propagation time and, thus, it can be used only in case of high communication delay accuracy [42]. A second method is the sender-to-receiver synchronization, a two-way communication between the nodes in which, after receiving the synchronization packet, the receiver timestamps it with its own clock and send it back to the sender. Assuming symmetric delay on the channel, this approach compensates for the propagation time delay. In fact, being  $\theta$  the receiver-sender offset and  $\delta$  the one-way propagation delay, the difference between the sending time and receiving time can be formulate as

$$\begin{cases} t_1 - t_0 = \theta + \delta \\ t_2 - t_3 = \theta - \delta \end{cases} \quad (3.9)$$

and the receiver-sender offset  $\theta$  becomes

$$\theta = \frac{(t_1 - t_0) - (t_2 - t_3)}{2} \quad (3.10)$$

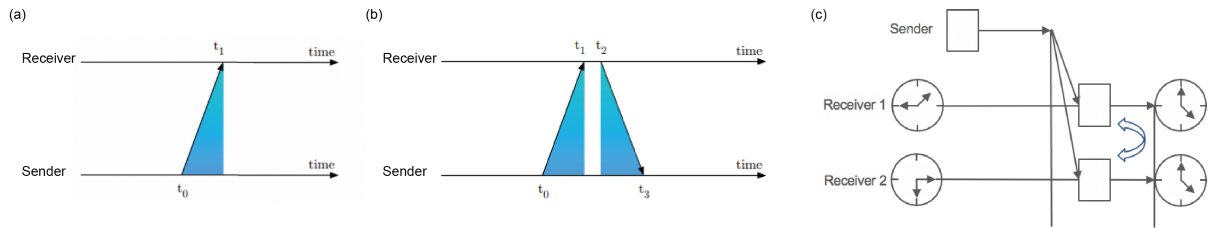
where  $t_0$ ,  $t_1$ ,  $t_2$  and  $t_3$  are represented in Figure 3.24 (b).

Another approach is the receiver-to-receiver synchronization in which a third party sends a synchronization packet to both the nodes and the receiving nodes exchange the arrival time of the packet among themselves and calculate the offset. This method assumes that the synchronization packet is received by all the nodes nearly at the same time and this is true when the transmission range is small and, moreover, it eliminates the uncertainty of the sender being the receiver uncertainty the only source of error [42–44].

Figure 3.24 shows the different methods of wireless synchronization that have been investigated.

Table 3.13 summarizes the main pros and cons of the two synchronization methods.

To sum up, cable connection represents an acceptable solution in case the device is



**Figure 3.24:** Different methods of wireless synchronization: (a) unidirectional broadcast; (b) sender-to-receiver broadcast; (c) receiver-to-receiver broadcast

**Table 3.13:** Pros and cons of via-cable and wireless synchronization

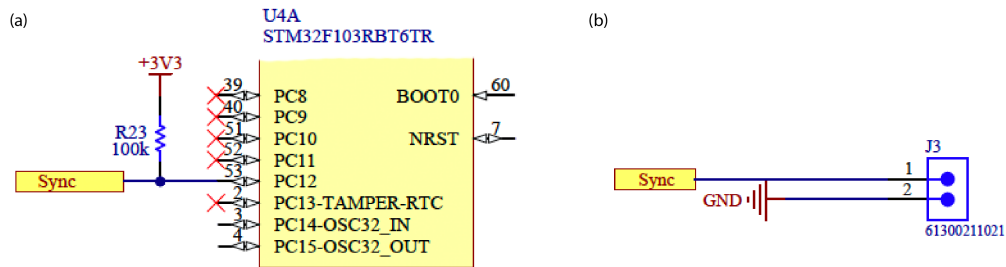
	Via-cable synchronization	Wireless synchronization
<b>Pros</b>	<ul style="list-style-type: none"> <li>• Easily implemented</li> <li>• Highly reliable</li> <li>• Negligible propagation time</li> </ul>	<ul style="list-style-type: none"> <li>• No cable obstruction</li> <li>• No extra time for set up</li> <li>• Possibility to manage clock drift</li> </ul>
<b>Cons</b>	<ul style="list-style-type: none"> <li>• Cumbersome</li> <li>• Impossibility to deal with clock drift</li> </ul>	<ul style="list-style-type: none"> <li>• Prone to external interference</li> <li>• Delay to send packets</li> </ul>

used in experiments for a limited amount of time. The setup is very easy and the drift between the clocks remains negligible. In case of more advanced applications or if the device needs to work for a long time, a wireless solution is required, and the clocks need to be resynchronized periodically. A receiver-to-receiver synchronization is not recommended since it requires a third-party component that broadcasts the beacon. A unidirectional broadcast is preferable to minimize the delay; however, the propagation time required to send a packet should be investigated.

Since the usage of MYLEG device is at the moment limited to experiments, synchronization via cable has been adopted. A 2-pin male header has been added on the bottom layer of the ankle PCB for the purpose. It comes out of the PCB so it can be easily accessed from the outside when the circuit is inserted into the 3D printed case. Figure 3.25 shows the schematic of the synchronization circuit: one pin is connected

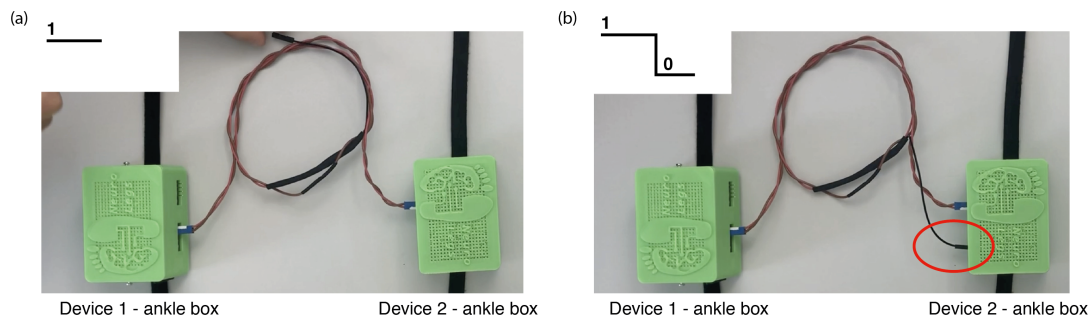


to GND (Figure 3.25 (b)) while the other one is connected to the microcontroller (pin 53) through a pull-up resistor as shown in Figure 3.25 (a).



**Figure 3.25:** (a) synchronization circuit in microcontroller schematic; (b) synchronization pin schematic

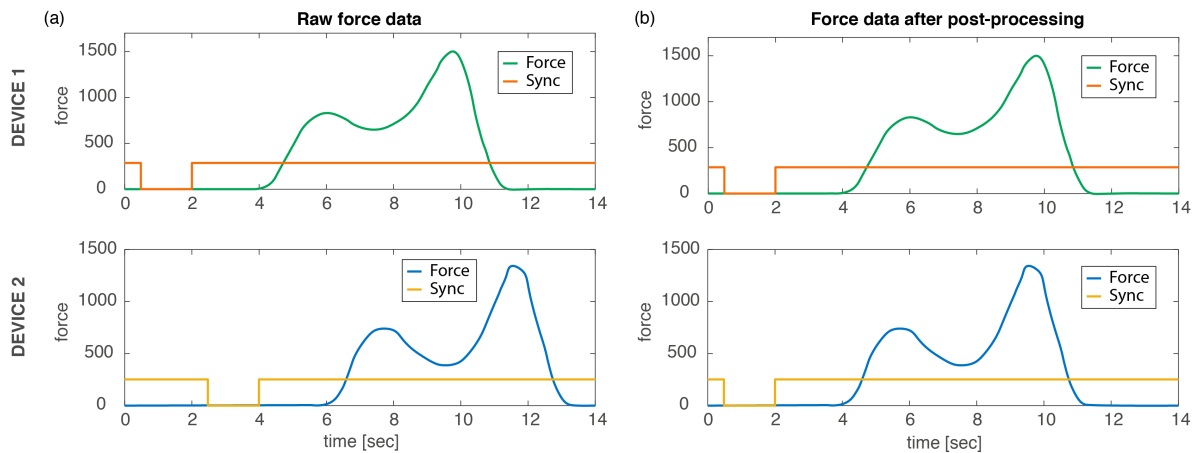
An on-purpose made cable has been created for the synchronization process. It comprises two 2-pins female sockets which have to be plugged into the two corresponding male headers on each device and a third black cable which has to be connected to any of the GND pins of any device. Firstly, the synchronization pins have to be connected so that the two PCBs share the same GND. At this point pin 53 of both the microcontrollers is still pulled High (Figure 3.26 (a)). Subsequently, the black cable has to be connected and pin 53 of both the microcontrollers turns Low (Figure 3.26 (b)). This sequence allows to create a changing status of the two pins in the exact same instant of time.



**Figure 3.26:** On-purpose made cable for synchronizing two devices. (a) when the synchronization pins are connected they are pulled High; (b) when the black cable is connected to GND they are pulled Low.

The digital value of the pins is recorded by the microcontrollers and sent to the system controller ODROID C2 via Bluetooth (together with the insole and IMUs data). This allows to synchronize the force and joint angle trends of the two devices by aligning the samples in which the digital value of the two synchronization pins is Low.

Figure 3.27 tries to explain the required data post-processing graphically.



**Figure 3.27:** Data post-processing for synchronization of multiple devices

Imagine connecting each device to one insole and, after performing the synchronization process, pressing on one force sensor of each insole simultaneously. Since the two devices run independently and they are started one after the other one (in this example, device 2 is started before device 1), by simply plotting their raw data, an offset between the two trends is present. This offset can be quantified and removed looking at the digital values of the synchronization pins. By aligning the samples during which the synchronization pins are pulled Low, the two trends synchronize one with the other.

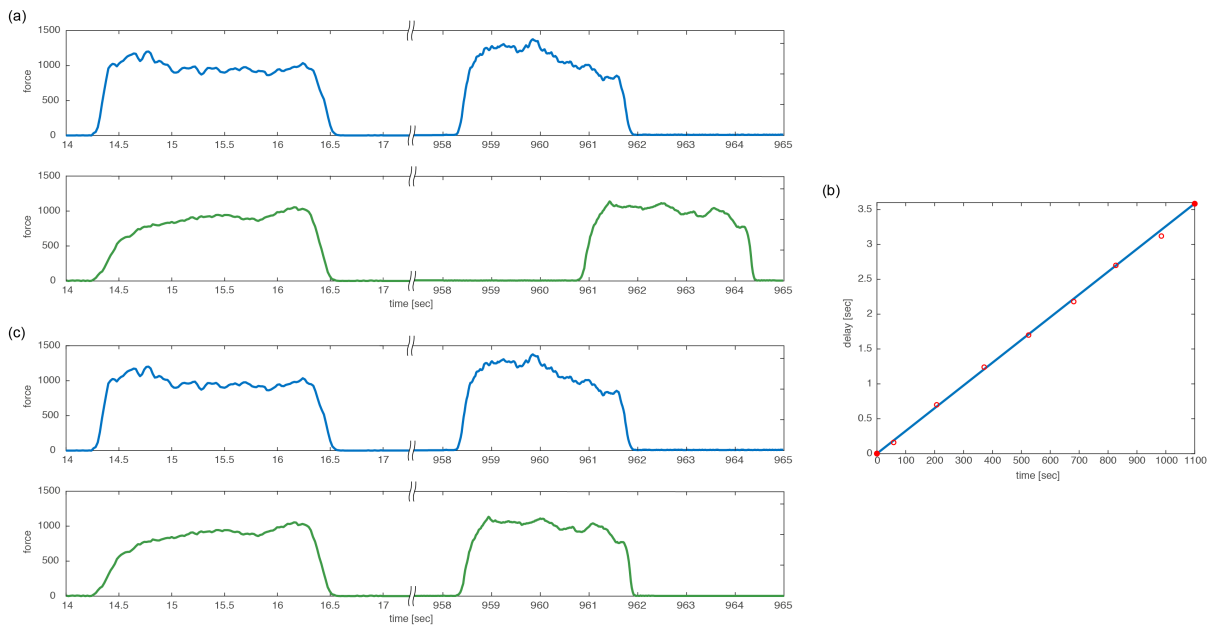
The setup of the process is very easy and requires very few time. It can be accomplished even before wrapping the boards around the subject's ankles placing the two boxes one beside the other one on a desk. The entire process lasts no more than 30 seconds.

As far as the problem of the clock drift between the microcontrollers of the two devices is concerned, the delay that accumulates over the time has been investigated by attaching one insole to each device and periodically pressing one force sensor of each insole simultaneously. The experiment was repeated 5 times, each trial lasted for 15 minutes and the force sensors were pressed approximately every 2 minutes.

By applying the synchronization process, the initial offset has been removed. However, an accumulated delay of approximately 3 seconds has been noticed after 15 minutes.

It corresponds to an error of the 0.3 % which is associated to the inaccuracy of the high-speed internal (HSI) oscillator of the STM32F103RBT6 microcontroller. In fact, the datasheet reports an accuracy that varies from -1,5 % to 2.2 % when the ambient temperature is between - 10 and +85 °C. The error lies in the admissible range, but it cannot be considered negligible in case of walking pattern analysis since the walking frequency is around 0.6 Hz. However, it has been noticed that the accumulated delay is linear over time as shown in Figure 3.28 (b). Because of this, it is possible to quantify the drift by simply knowing the initial and the final delay (red dots in Figure 3.28 (b)). Therefore, the synchronization process has to be repeated also at the end of the experiment before quitting the system. This allows to estimate the coefficient of the line between the two points and remove the offset that accumulates over time between the collected data.

Figure 3.28 (a) tries to explain the required data post-processing graphically.



**Figure 3.28:** Data post-processing for removing the delay accumulated over time; (a) raw force data as acquired by the electronic boards; (b) linear trend of the accumulated delay; (c) force data after removing the calculated offset

To conclude, synchronization problem has been solved post-processing the data coming from the two electronic boards. The delay could be reduced embedding into the PCBs an external crystal with a smaller jitter to increase the accuracy of the microcontrollers' timing.

## 3.6 Software implementation

As far as the software is concerned, both the firmware to be loaded on the microcontroller of the electronic board and the software for running the system-controller and driving the stimulation are needed for the device to properly function. Since the same system-controller is used and the stimulation control was not part of this thesis project, only minor changes have been made on the software uploaded on ODROID-C2. In particular, it was necessary to take into account that a higher number of bytes are now sent via Bluetooth because one more IMU has been introduced. For doing this, all the bytes are initially read into a single variable *bufferTemp* and then split and saved into many variables depending on their length.

---

```
1 int ReadDataPackage(int SerialHandleSensorsFoot)
2 {
3     for (int zz = 0 ; zz < 59 ; zz++){
4         read(SerialHandleSensorsFoot , bufferTemp+zz , 1);
5     }
6
7     memcpy(IMU1_gyro , bufferTemp+1, 6);
8     memcpy(IMU1_acc , bufferTemp+1+6, 6);
9     memcpy(IMU2_gyro , bufferTemp+1+6+6, 6);
10    memcpy(IMU2_acc , bufferTemp+1+6+6+6, 6);
11    ...
12 }
```

---

Although the Bluetooth module has been substituted with a newer version, the code for setting the communication remained unchanged because the same RFCOMM communication protocol is used.

Finally, the algorithm for calculating the knee angle has been implemented as described in Section 3.3.1.

---

```
1 int resetFlag = 0;
2 void ThreadGenerateYaw()
3 {
4     double alpha = 0.02;
5     double dt = 0.02;
6
7     for (auto i = 0 ; i < 3 ; i++) {
8         IMU1_accCal[i] = IMU1_acc[i] * 4/32768.0; // g+acc [g]
```

---

---

```

9     IMU1_gyrCal[i] = IMU1_gyro[i] * 500 * 3.14159265 / (32768.0 * 180); // [rad/s]
10 }
11
12 IMU1_angle_acc = atan2(IMU1_accCal[1], IMU1_accCal[0]); // accelerations on the xy-plane
13 IMU1_angle_gyr = IMU1_angle_compl + dt * IMU1_gyrCal[2]; // angular rate around the z-axis
14 IMU1_angle_compl = (1 - alpha) * IMU1_angle_gyr + alpha * IMU1_angle_acc;
15
16 if (resetFlag > 50 && resetFlag < 150)
17     IMU1_kneeYawOffset = IMU1_kneeYawOffset + IMU1_angle_compl;
18 else if (resetFlag == 150)
19     IMU1_kneeYawOffset = IMU1_kneeYawOffset / 99.0;
20 else if (resetFlag > 150)
21     IMU1_kneeYaw = IMU1_angle_compl - IMU1_kneeYawOffset;
22
23 ... // similar for IMU2
24 IMU2_angle_acc = atan2(-IMU2_accCal[1], IMU2_accCal[0]); // accelerations on the xy-plane
25 ...
26
27 kneeYaw = (IMU2_kneeYaw + IMU1_kneeYaw) * 180 / 3.14159265;
28 resetFlag++;
29 }

```

---

The firmware to be loaded on the microcontroller of the electronic board is written using ARM MBED online compiler. It is an open source IoT operating system that provides a well-defined API to develop C++ application and thousands of code examples and libraries for common components.

The flowchart is reported in Appendix E. At the beginning, libraries for the embedded components are loaded and the pins are initialized as analog/digital inputs or outputs. The system controller ODROID-C2 opens the Bluetooth serial port and sends a starting packet to the electronic board to detect problems in the transmission. If the char is correctly received by the electronic board, then, an interrupt that recall a specific function every 20 ms is started. This function verifies that all data have been sent in the previous sampling period and starts a new data acquisition and transmission. The recurring interrupt stops whenever the Bluetooth serial port is closed at the ODROID-C2 side.



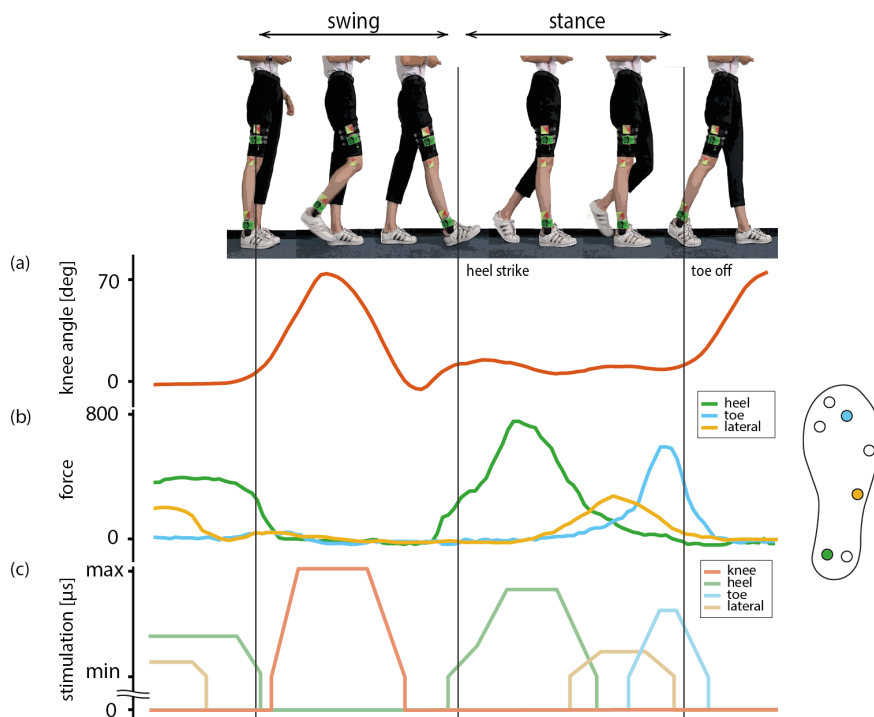
# Validation

---

This chapter aims at describing all the tests that have been performed to assess the functionality of MYLEG device and its accuracy in predicting both the force distribution and the joint angle while walking in different conditions.

Before starting with the validation itself, it is important to have a look at the collected data that are used to drive the stimulation. Figure 4.1(a) shows the trends of the knee angle during an entire walking cycle, Figure 4.1(b) shows the forces applied over the 3 sensors that are usually selected to stimulate the patient (one at the heel, one in the middle and one in the front) while Figure 4.1(c) represents the corresponding levels of stimulation. Different levels of stimulation are obtained modulating the pulsewidth of the current provided by the TENS stimulator using superficial electrodes, while current amplitude is kept constant. Predefined lower threshold for angles and forces have to be overcome in order to activate the stimulation and then the pulsewidth does not increase above a maximum value to avoid hurting the patient. The constant amplitude value, the minimum and maximum value of pulsewidth and the corresponding minimum and maximum value of forces and angle are determined during an initial phase of calibration of the device. Different thresholds are selected for each channel. Imposing a sufficiently high lower threshold for the knee angle, it is possible to remove unwanted oscillations of the joint angle during the stance phase which are associated to inaccuracy of the system such as, for example, vibrations of the boards due to the

impact with the ground. A linear mapping of the measured forces and angles is used to determine the stimulation parameters, hence, the 4 channels of stimulation exactly reassemble the trends of the collected data. Primary requirement of the system is, therefore, the ability of MYLEG system to accurately replicate these trends more than their actual absolute values. In fact, the maximum value of the knee angle is associated to the maximum threshold of the stimulation despite their absolute values. However, it could be interesting to assess the range of motion of the joint to extend the usage of MYLEG system to monitoring of daily activities.



**Figure 4.1:** (a) Knee angle, (b) force distribution and (c) corresponding stimulation calculated by MYLEG system during one entire walking cycle

## 4.1 Assessment of MYLEG functioning

No specific instruments were at disposal for assessing IMU functionality. Therefore, the correctness of the acquired data was assessed by aligning one axis at a time with Earth gravity and keeping the electronic board still in order to only measure gravitational acceleration. An example of the collected data is shown in Table 4.1 in which the raw



values as they are collected from the electronic board are listed. However, a calibration process is required to convert the linear acceleration in Gauss [g] and the angular rate in radian per second [rad/s] using Formulas 4.1 and 4.2 respectively.

$$acc_{CAL} = acc \cdot \frac{4}{32768} [g] \quad (4.1)$$

$$gyr_{CAL} = gyr \cdot \frac{500}{32768} \cdot \frac{\pi}{180} [rad/s] \quad (4.2)$$

1 g corresponds to a raw value of approximately 8200 which matches what has been calculated along the axis aligned with Earth gravity. Non-zero values have been obtained along the other axes, but this can be associated to the inaccuracy of the IMU due to its reduced dimensions and low cost. In fact, angular rates of 0.01 - 0.02 rad/s and linear accelerations smaller than 0.08 g fit in the offset ranges that are reported in the datasheet of the component (see Table 3.7).

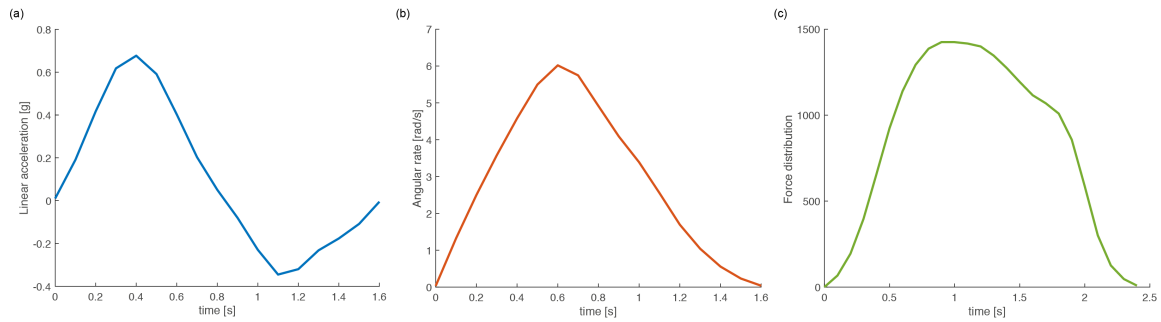
cnt	GirX	GirY	GirZ	AccX	AccY	AccZ
0	87	126	-89	-677	17	-8188
0.02	84	119	-90	-666	16	-8193
0.04	88	125	-97	-677	7	-8191
0.06	78	137	-100	-681	5	-8199
0.08	87	121	-93	-667	11	-8191
0.1	78	125	-88	-670	21	-8195

cnt	GirX	GirY	GirZ	AccX	AccY	AccZ
4.22	80	74	-79	-8266	-11	359
4.24	83	51	-77	-8277	-11	365
4.26	74	43	-80	-8269	-4	358
4.28	88	53	-91	-8263	-3	351
4.3	94	56	-83	-8277	-5	347
4.32	94	78	-86	-8271	-5	340

cnt	GirX	GirY	GirZ	AccX	AccY	AccZ
9.22	76	136	-97	-403	8112	278
9.24	70	141	-88	-406	8119	278
9.26	56	127	-96	-409	8116	269
9.28	66	126	-96	-415	8111	224
9.3	93	126	-96	-413	8119	218
9.32	142	147	-101	-405	8112	224

**Table 4.1:** Raw data collected when aligning the IMU with z-, x- and y-axis respectively.

Other tests have been performed with the PCB in motion. The board was moved along each axis, imposing an acceleration and a deceleration along the direction of movement and around each axis in order to measure the angular velocity. Moreover, the analog circuit functioning was assessed by recording the variation in the collected data when applying a pressure over each force sensor. Data collected from the sensorized insole are expressed in digital values as they are generated as output of the ADC integrated in the microcontroller. Examples of acquired trends during the described tests are shown in Figure 4.2 and perfectly correspond to what was expected.



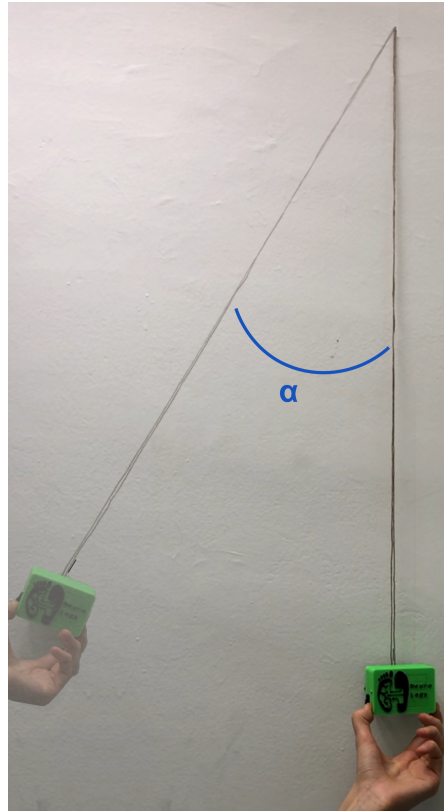
**Figure 4.2:** Collected data when moving the electronic board (a) along the  $y$ -axis, (b) around the  $z$ -axis and (c) pressing one force sensor of the sensorized insole

## 4.2 Assessment of MYLEG repeatability

Repeatability refers to the variation in subsequent measurements taken by a single instrument under the same conditions. IMU data repeatability has been assessed in order to evaluate the reliability of the device in estimating joint angles and guarantee the quality of the outcome. To do so, the electronic board has been repeatedly moved between two fixed points that create an angle of 30 degrees as shown in Figure 4.3 and the angle measured by the electronic circuit has been then compared to the real value.

Figure 4.4 shows the results of the first 3 trials conducted at 3 different velocities. It can be clearly stated that the variability of the instrument in such condition does not allow to get reliable angle measurements. In particular, the noise affecting the data at high speed can be associated to an excessive reliability of the algorithm that calculates the angle on the accelerometer as described in Section 3.3.1. To reduce this noise, the coefficient of the complementary filter has been increased in order to rely more on gyroscope data but paying attention not to introduce an excessive drift over time.

Figure 4.5 shows the results of identical experiments to that described above after imposing a more appropriate filter coefficient value. 30 oscillations have been performed and the repeatability is shown in Figure 4.5 (d-f) by superimposing all the curves obtained at the same velocity. Mean and standard deviation are shown in the table in Figure 4.6. Despite a significant increase ( $p < 0.001$ ) in the error have been measured for higher velocities, standard deviation value remains similar in all the three conditions (Figure 4.6). It is important to notice that the experiment has been performed



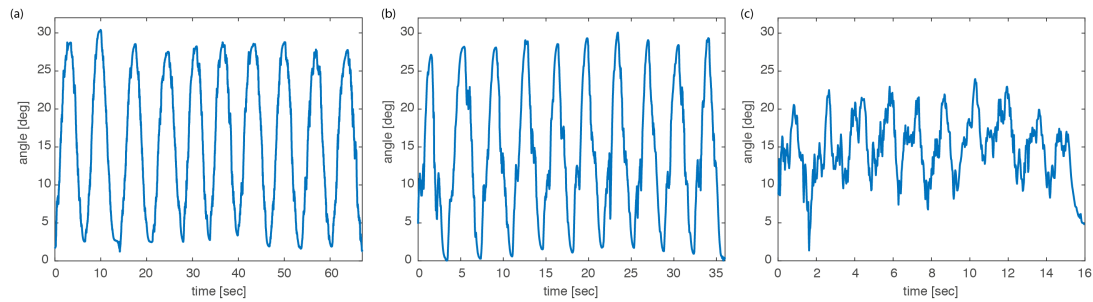
**Figure 4.3:** *Assessment of IMU repeatability moving the electronic board between two known points*

manually so same variability could have been introduced by the operator. In particular, it is reasonable to consider a reduced precision in performing the experiment by the operator at higher speed and this is consistent to the results.

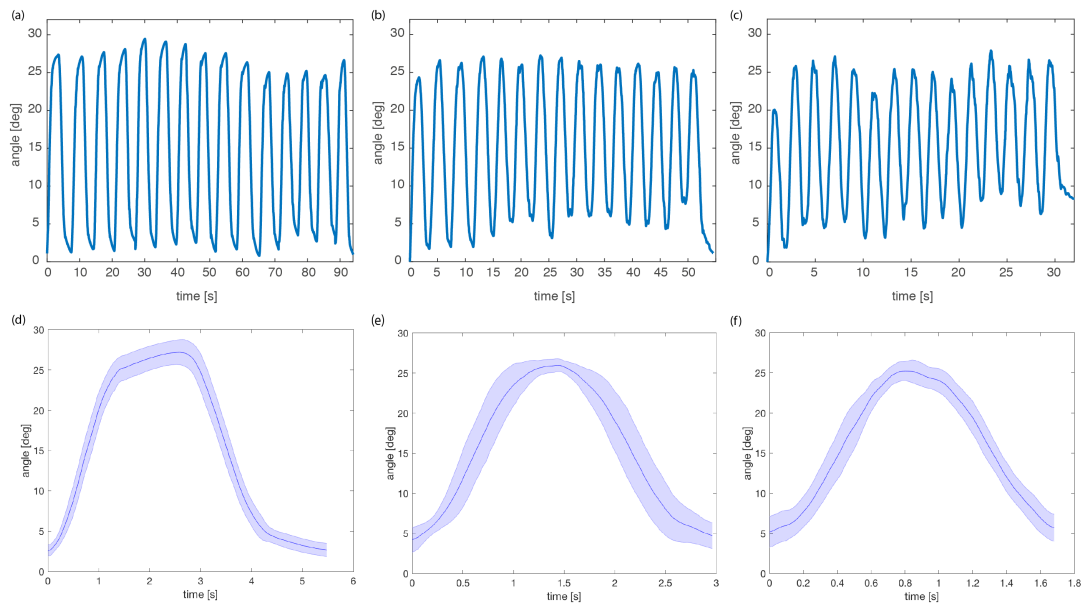
### 4.3 Assessment of MYLEG accuracy

In order to assess the accuracy of the device, the estimated trends are compared to those obtained using a 3D capture motion system that is able to measure joint angles by tracking over time the position of the markers applied over the leg of the patient. The real trends of the joint angle have been obtained in two different ways:

- (a) recording with a single camera (iPhone X, 1080p HD at 60 fps) placed frontally and parallel to the direction of walking and, then, video post processing with Kinovea software to extract the coordinates of the markers over time;
- (b) recording with GRAIL system at Balgrist University Hospital in Zürich which



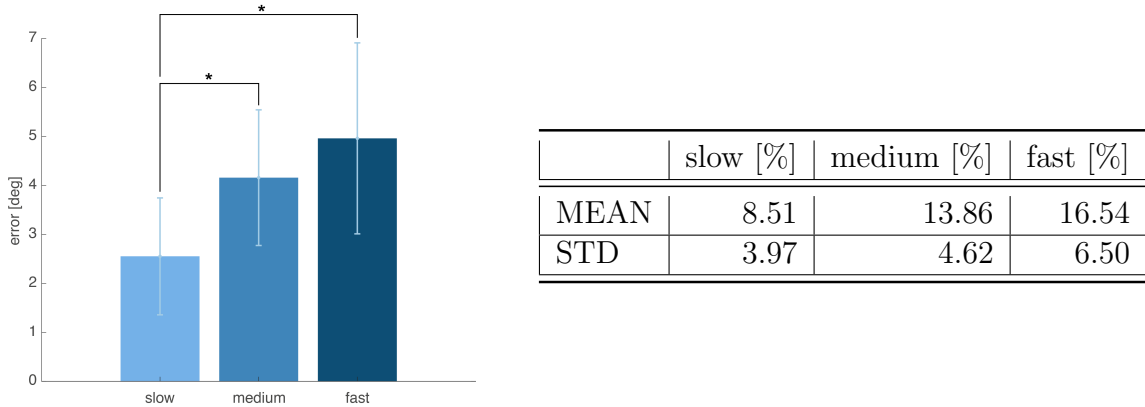
**Figure 4.4:** Assessment of IMU repeatability at 3 different velocities using the complementary filter coefficient of the original board



**Figure 4.5:** Assessment of IMU repeatability at 3 different velocities after increasing the complementary filter coefficient to remove the excessive noise

includes a Vicon based 3D capture motion system with 10 cameras and 2 force plates.

The former method is very easy to set up and has been performed directly in the Neuroengineering Laboratory at ETH Zürich. It just requires 1 camera, 1 tripod and at least 3 markers (home-made markers made of cardboard); it gives the possibility to record light stimuli reproduced in front of the camera, allowing for the synchronisation of the camera and the electronic board (see Section 4.3.1) but it does not allow to obtain any information about the force distribution. Moreover, the real trends could be affected by small error due to some inaccuracies of the Kinovea software in following the trajectories described by the markers. On the other hand, the GRAIL system requires a much longer and complicated set up but produces a much more accurate

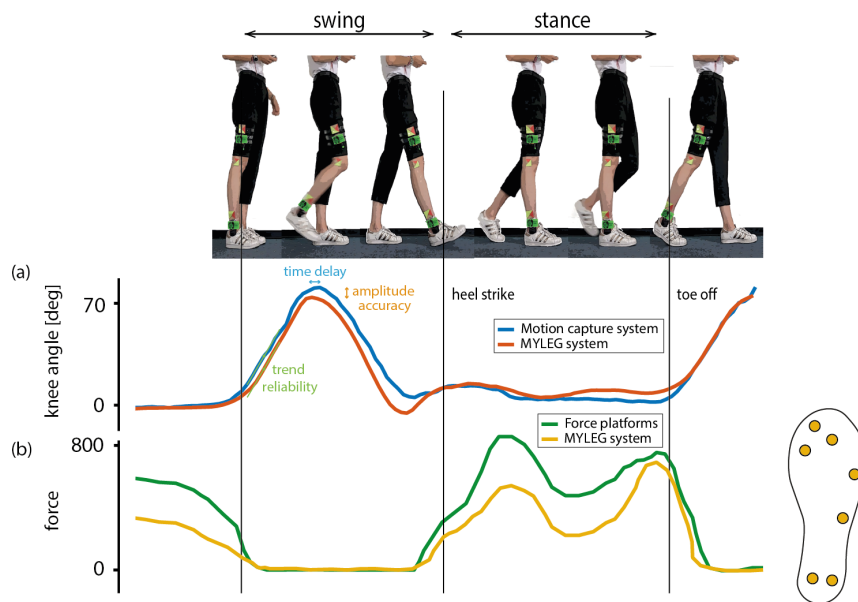


**Figure 4.6:** Percentage error in angle estimation while assessing repeatability

result. It allows to precisely measure the force applied by the subject on the treadmill while walking and to set a known and constant walking speed but it does not permit to synchronize the electronic board with the GRAIL system. Because all these pros and cons, both the methods have been used to study different features of MYLEG system. In particular, the parameters that have been taken into account while assessing the accuracy of MYLEG system are:

- time delay: delay in time between the real (motion capture system) and the estimated (MYLEG system) knee angle curves. It has been calculated as the difference in time between the peak of the two curves which is reached during the swing phase. The time delay should be as small as possible to assert that the subject perceives a real-time stimulation;
- trend reliability: percentage over the entire walking cycle in which the real and the estimated knee angle curves have the same derivative sign. It gives an idea on how well MYLEG estimated angle follows the real trends and this is extremely important since the subject is provided with a stimulation that has the same shape of that of the measured variables;
- amplitude accuracy: difference in absolute value between the real and the estimated knee angle curves. It can be calculated as the amplitude difference at the peak or over the entire walking cycle. It gives an idea on how accurate the system is in replicating the range of motion of the patient's joint.

The comparison between real and estimated trends and a graphical representation of the parameters of interest are shown in Figure 4.7.



**Figure 4.7:** Comparison between motion capture system measured and MYLEG system estimated trends for (a) knee angle and (b) force distribution. Graphical representation of the parameters used for validation.

In the following chapters different scenarios are analysed. In particular, the improvement in estimating the shank angle using the new MYLEG system with respect to the original board has been investigated. Subsequently, the benefit of adding one more PCB on the thigh of the subject is shown and, finally, the assessment of the accuracy of the entire system is described in different conditions.

### 4.3.1 Comparison with the original board

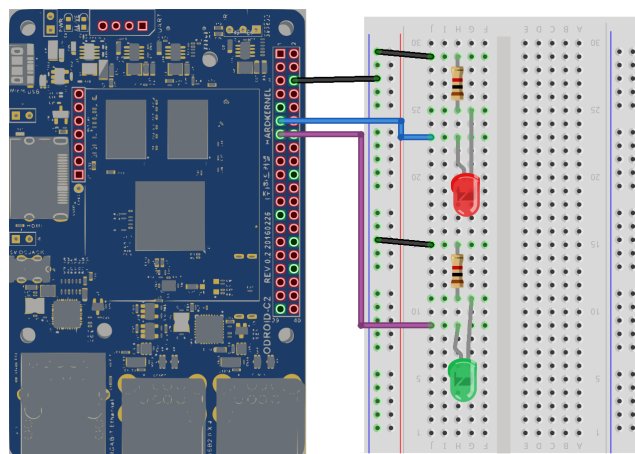
In order to compare the new MYLEG system to the original one, only the ankle board has been considered and the accuracy of the two devices in estimating the shank angle has been assessed. Figure 4.8 shows the experiment setup; both systems have been wrapped around the subject's ankle and 3 markers have been placed over his leg in order to subsequently extract their trajectories using Kinovea software.

As already explained before, using a single camera in the laboratory room gives the possibility to synchronize the real trends with the collected data. This has been done controlling 2 LEDs with ODROID-C2 (see Figure 4.9): meanwhile force and angle data



**Figure 4.8:** Comparison of the new MYLEG system and the original board in estimating the shank angle: experimental setup

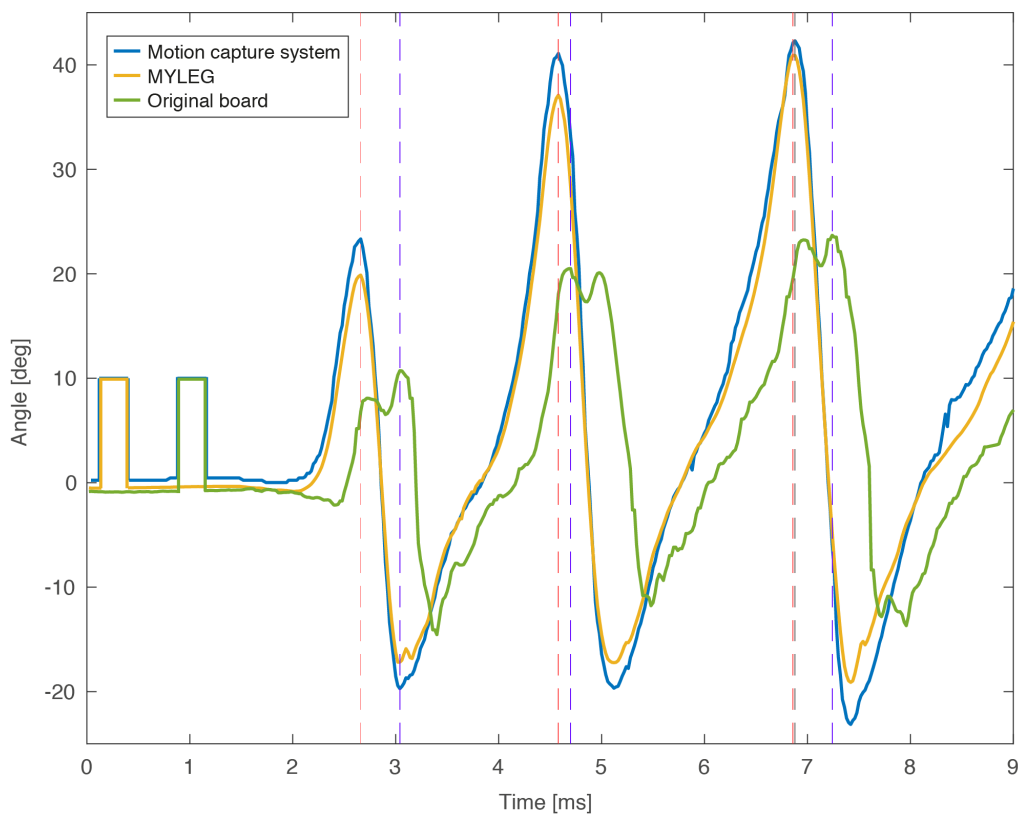
are collected, the status of the LEDs (pins 11 and 12 of ODROID-C2) is saved by the system controller in correspondence to each sample; moreover, while post-processing the data with Kinovea software, it is possible to keep track of the video frames during which the light is ON. Lining up the two signals allows to align the collected data for a more accurate comparison.



**Figure 4.9:** Schematic of the circuit implemented on ODROID-C2 to synchronize the real trend from a motion capture system with the collected data from MYLEG system

In Figure 4.10, the real shank angle (blue line) is compared to the one estimated by

the new system in yellow and that of the original box in green. The three curves have been already aligned in time so it can be first of all inferred that MYLEG system has a reduced time delay with respect to the original circuit. Since the same system controller is used to process the data from both the boards, the higher time precision is attributed to the higher data rate of the new Bluetooth module that allows a faster communication. Looking at the absolute value of the predicted angle, a much higher amplitude accuracy can be observed in MYLEG estimate as well as an increased trend reliability. In fact, the shape of the curve predicted by the original circuit does not reproduce that of the real angle during the maximum flexion of the knee, providing the subject with a misleading stimulation. The improved behaviour of MYLEG is associated to a grater quality of the algorithm that calculates the angle and a more careful choice of the filter coefficient which allows to remove unwanted oscillations.



**Figure 4.10:** Comparison of the shank angle estimation between a motion capture system (blue line), the new MYLEG system (yellow line) and the original board (green line).

Previous analysis of the original circuit over approximately 140 steps have demonstrated a time delay greater than 120 ms and a trend reliability around 70 %. These



values are taken from granted and can be compared to those of the new MYLEG system discussed in Section 4.3.3

To sum up, it is possible to state that the new MYLEG system is able to provide already more accurate results both in time and in amplitude with respect to the original board just considering one board.

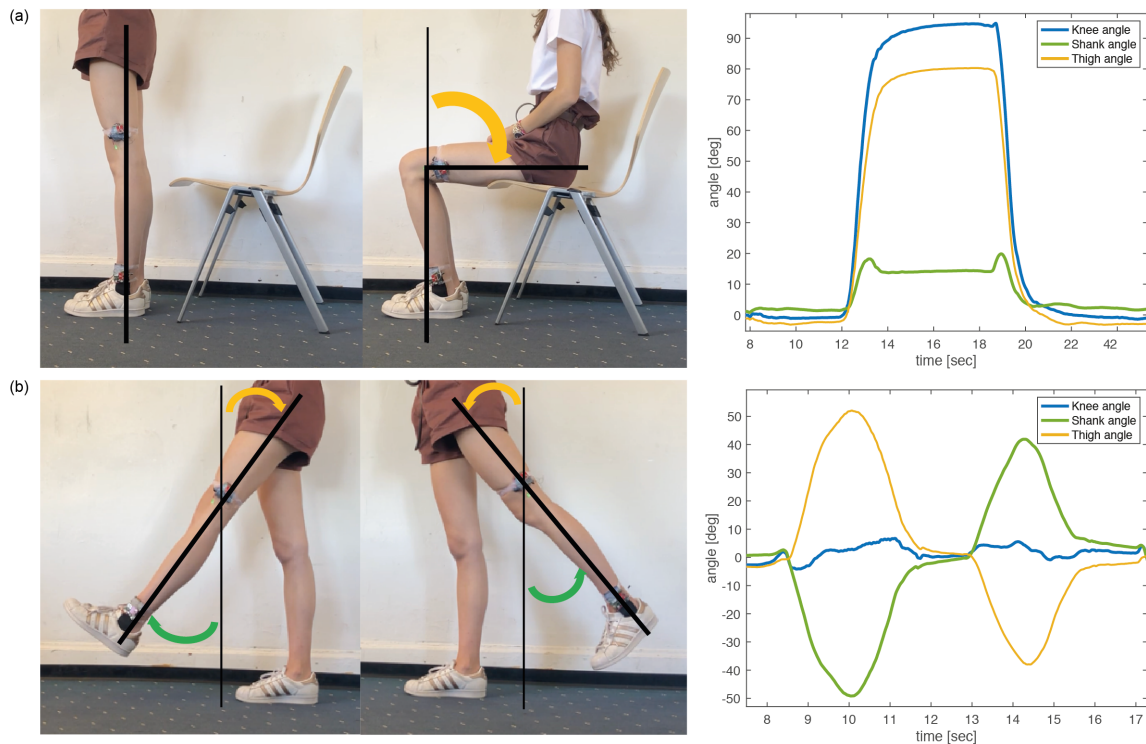
### 4.3.2 Two IMUs angle estimation

In the previous chapter, the improvement introduced by the new system in estimating the joint angle with respect to the original circuit has been demonstrated. For convenience in experiments, the ankle PCB of the new MYLEG system is from now on considered as representative of the original board.

In this chapter, the real need of the second IMU is investigated comparing the angle obtained with only the ankle PCB (as it was with the original circuit) to the one measured by the entire system.

Firstly, the presence of the second board placed over the thigh of the subject allows to detect and correct false positive and false negative in the patient's stimulation. For example, during sit to stand activity, the original board does not provide any stimulation to the patient since the ankle remains still and the circuit does not record any variation in the angle. This variation is instead measured by the thigh PCB which provides the feedback to the subject. On the contrary, when oscillating the leg in the sagittal plane, the original box does stimulate the subject even if his knee is kept straight. Considering the upper board, an angle which is equal but opposite to that of the ankle is recorded and the stimulation is cancelled out. These different scenarios are graphically explained in Figure 4.11. In particular, the green line is indicative of the feedback provided to the subject in case only the ankle IMU is used; the blue line corresponds to a stimulation in which both the boards are considered while the yellow curve represents the thigh contribution.

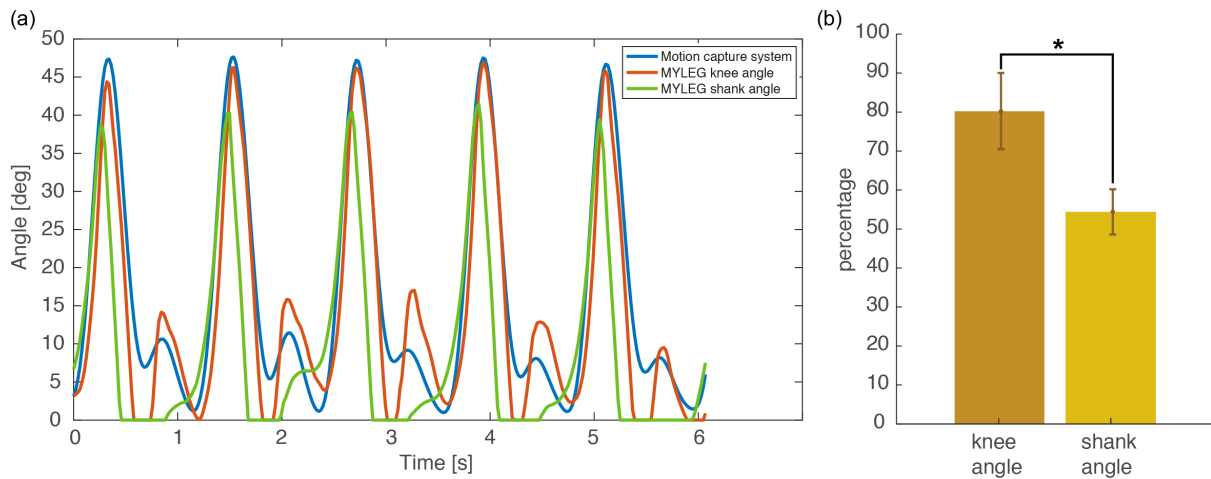
Keeping in mind that the aim is to provide the subject with a feedback on his knee proprioception, the real knee angle obtained with a 3D motion capture system (blue line in Figure 4.12 (a)) is compared with the knee angle (red line) and the shank angle (green



**Figure 4.11:** Daily-activities in which the presence of the thigh IMU removes (a) false negatives (the patient is not stimulated even if the knee angle is changing) and (b) false positive (the patient is stimulated although his knee is straight). The green line is considered representative of the behaviour of the original circuit while the blue line represents the angle calculated by the new MYLEG system.

line) estimated by MYLEG. The knee angle is obtained by the combination of data from the 2 boards while the shank angle only considers the PCB attached to the ankle of the subject (as it was in the original circuit). Figure 4.12 (a) highlights a higher accuracy in providing knee joint feedback both in time and amplitude. However, the more interesting aspect is the significantly increased trend reliability of the red curve with respect to the green one ( $p < 0.001$ ) as shown in Figure 4.12 (b). When considering only the bottom part of the system, the subject is provided with a misleading stimulation. In fact, in the second part of the swing phase, the shank is already moving forward while the knee angle is still flexing due to the contribution of the thigh. Moreover, the shank starts to be pushed backwards during the stance phase when the knee is actually straight.

To sum up, the entire MYLEG system gives an even more accurate result both in time delay, amplitude accuracy and trend reliability if the second IMU is included.

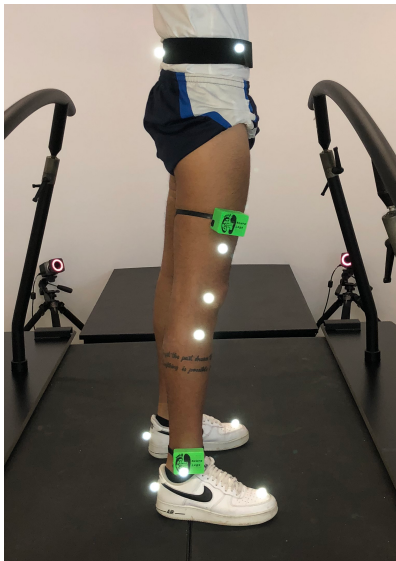


**Figure 4.12:** (a) comparison of the knee (red line) and shank (green line) angles estimated by MYLEG system with the knee flexion recorded by a 3D motion capture system (blue line); (b) increased trend reliability of the knee angle with compared to the shank one

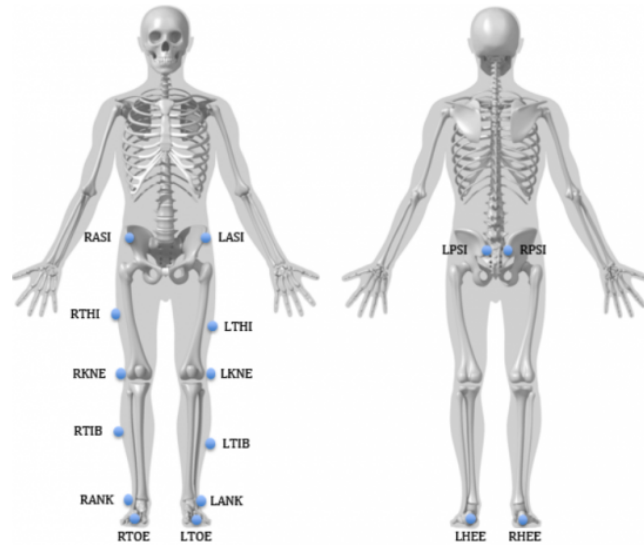
### 4.3.3 Accuracy of the entire system

During a one-day trial at Balgrist University Hospital in Zürich, the accuracy of the entire MYLEG system in estimating the knee angle and predicting the exerted force has been measured. Data was recorded in the so-called GRAIL room which comprises the highly sophisticated Vicon Nexus Motion Capture system and one treadmill with two force plates that can be controlled independently. For this analysis, one 23-years-old male healthy subject was recruited and equipped with both the thigh box and the ankle box on his right leg as in Figure 4.13. 16 markers have been placed on both legs and on the hip according to the Plug-In Gait configuration shown in Figure 4.14.

The experimental protocol consists of 2 over ground walking tasks (level walking and inclined walking). Level walking was conducted on the treadmill at 4 different velocities and 3 repetitions were performed for each velocity. Each repetition consists of a 1.5 minutes walking trial during which the velocity has been kept constant. Initially, the comfortable walking speed (100 %) was found according to subject vocal reports and then, one slower (75 %) and two faster (125 % and 150 %) velocities were considered. Inclined walking was conducted on the treadmill at 2 different inclinations. The maximum upward inclination (+ 15 %) and the maximum downward inclination (- 15 %) were considered. Due to lack of time, the subject performed only 1 repetition for each inclination and each repetition consists of a 1.5 minutes walking trial. The



**Figure 4.13:** *Experimental setup*



**Figure 4.14:** *Vicon Plug-In Gait marker configuration for calculating lower limb joint kinematics and kinetics*

inclination is kept the same during the entire repetition and the velocity is maintained constant at the subject's self-selected speed.

Before the analysis, the collected data was post-processed using Vicon Nexus software which requires to fit the Plug-In gait Lower Limb model to the markers and fill gaps in marker trajectories. Subsequently, the parameters of interest, namely the coordinates on the sagittal plane (YZ plane) of markers RTIB, RKNE and RTHI and the ground reaction forces on the right plate, were extracted and exported as a c3d file for each trial.

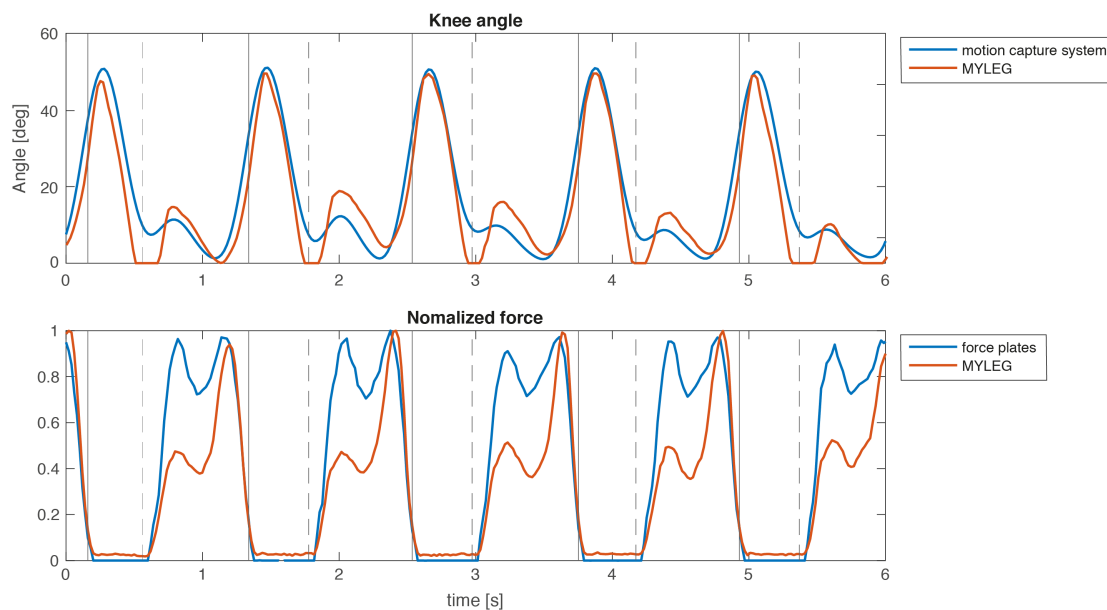
Data analysis was conducted in MATLAB after converting the c3d file in .mat extension. For each trial, the trend over time of the knee angle has been calculated from the markers coordinates according to Formula 4.3.

$$\theta = \begin{cases} \arccos\left(\frac{SHI \cdot FEM}{|SHI| |FEM|}\right), & \text{if } (SHI \times FEM)_z > 0 \\ 2\pi - \arccos\left(\frac{SHI \cdot FEM}{|SHI| |FEM|}\right), & \text{if } (SHI \times FEM)_z \leq 0 \end{cases} \quad (4.3)$$

where  $FEM = RTHI - RKNE$  and  $SHI = RTIB - RKNE$  being RTHI, RKNE and RTIB the (y,z) coordinates of the corresponding markers. The so obtained trend is compared to that estimated by MYLEG system.

Subject's force distribution was analysed by isolating the z-component of the ground reaction force recorded by the GRAIL room's force plates and comparing it to the sum of the forces measured by each sensor of the MYLEG's insole. The absolute values in Newton cannot be directly compared because of a huge difference in the area over which the force is calculated. In fact, the treadmill records the force exerted by the subject over his entire foot sole while MYLEG system's area of measure is limited to that of the 7 sensors. Because of this, the normalized trends are analysed to compare the force distributions.

Figure 4.15 shows the comparison between the data obtained using a gold standard 3D capture motion system integrated with force plates and the MYLEG device both for the knee angle and the force distribution over 5 steps.



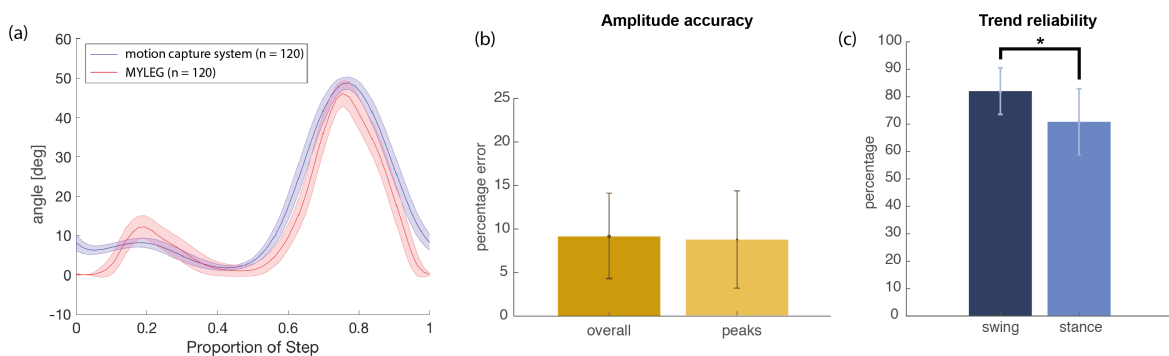
**Figure 4.15:** Comparison between the data obtained using a gold standard 3D capture motion system integrated with force plates (blue line) and the MYLEG device (red line) both for the knee angle and the force distribution over 5 steps

For each trial, 40 steps were extracted in order to have a total of 120 steps for each velocity and 40 steps for each inclination. In order to perform force and joint angle analysis, each full trial has been segmented into steps. For doing this, heel strike and toe off events were identified by determining when the reaction force exceeds and drops

below a certain threshold, respectively. Two subsequent heel strikes are used to identify each gait cycle; samples between heel strike and toe off represent the stance phase while the swing phase goes from the toe off to the heel strike. For better comparison, all the steps for a certain velocity or inclination were superimposed by normalizing the length of each cycle. Value sets for each parameter of interest were extracted and each distribution was tested for normality with Single sample Kolmogorov-Smirnov goodness-of-fit hypothesis test. Since all the distributions were found to be not normal, a non-parametric one-way ANOVA or Kruskal–Wallis test was performed to test whether samples originate from distributions with equal medians. In fact, the Kruskal–Wallis test allows to compare more than two independent groups of equal or different sample sizes.

### MYLEG accuracy during self-selected speed walking

The first analysis that has been conducted concerns the comparison of the knee angle measured by Vicon 3D capture motion system and the knee angle estimated by MYLEG system. After aligning and superimposing all the 120 steps, the mean and standard deviation has been calculated over the entire walking cycle for both trends and shown in Figure 4.16 (a).



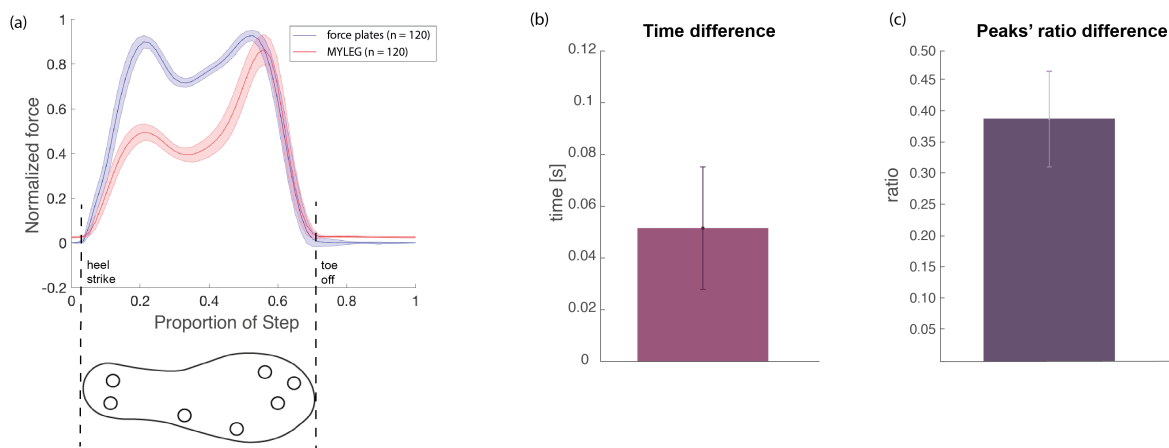
**Figure 4.16:** (a) Knee angle comparison between the data obtained using a gold standard 3D capture motion system (blue line) and the MYLEG device (red line) during comfortable walking; (b) amplitude difference and (c) trend reliability during self-selected speed walking

A high accuracy of MYLEG system in predicting the knee angle can be directly infer from the graph. In particular, an error of approximately 10 % has been measured in the amplitude accuracy but no significant difference has been found is considering the

differences between only the peak values or over the entire walking cycle (Figure 4.16 (b)) confirming that the inaccuracy of MYLEG system is distributed over the entire step and not only at the peaks level. This is particularly important for driving the stimulation meaning that the almost equally distributed error does not affect the different levels of the perceived sensation. Considering the trend reliability (Figure 4.16 (c)), stance and swing phase have been analysed separately. A significant difference has been demonstrated between the two distributions ( $p \ll 0.001$ ) being the trend reliability of the swing phase 10 % higher than that of the stance phase. A reduced accuracy during the stance phase could be associated to the impact of the foot on the treadmill at the heel strike that causes the vibration of the electronic boards. In fact, a more pronounced peak in the stance phase is measured at the beginning of the stance. However, as already mentioned before, a high accuracy in the swing phase represents the priority for driving the stimulation. Error and oscillations of the angle during the stance phase can be removed by increasing the lower threshold at which the stimulation starts. In fact, assuming that the subject's knee is kept straight during the stance phase, a sufficiently high threshold could be set so that no stimulation is provided during this portion of the gait.

As far as the force distribution is concerned, a high accuracy in the timing of the two predicted peaks has been demonstrated. In fact, an mean error smaller than 50 ms has been measured and it cannot be perceived by the subject (Figure 4.17 (b)). However, a bigger difference in the ratio between the two peaks of MYLEG system with respect to the one measure using the force plates can be clearly inferred from the graph in Figure 4.17 (a). Precisely, the difference between MYLEG system's peaks is 40 % higher than that of the GRAIL system 4.17 (c).

This can be associated to an uneven distribution of the force sensors over the foot sole. In fact, a greater number of sensors are concentrated in the frontal part of the insole and thus the sum of the forces during the toe off turns out to be greater than that at the heel strike when only 2 sensors are activated. However, this does not affect the stimulation provided to the subject since the force from each sensor is considered



**Figure 4.17:** (a) Force distribution comparison between the data obtained using force plates (blue line) and the MYLEG device (red line) during comfortable walking, (b) time difference between peaks and (c) difference in peaks' amplitude ratio during self-selected speed walking

individually. In fact, the level of stimulation provided for one sensor only depends on the thresholds that have been set during the calibration phase for that specific sensor.

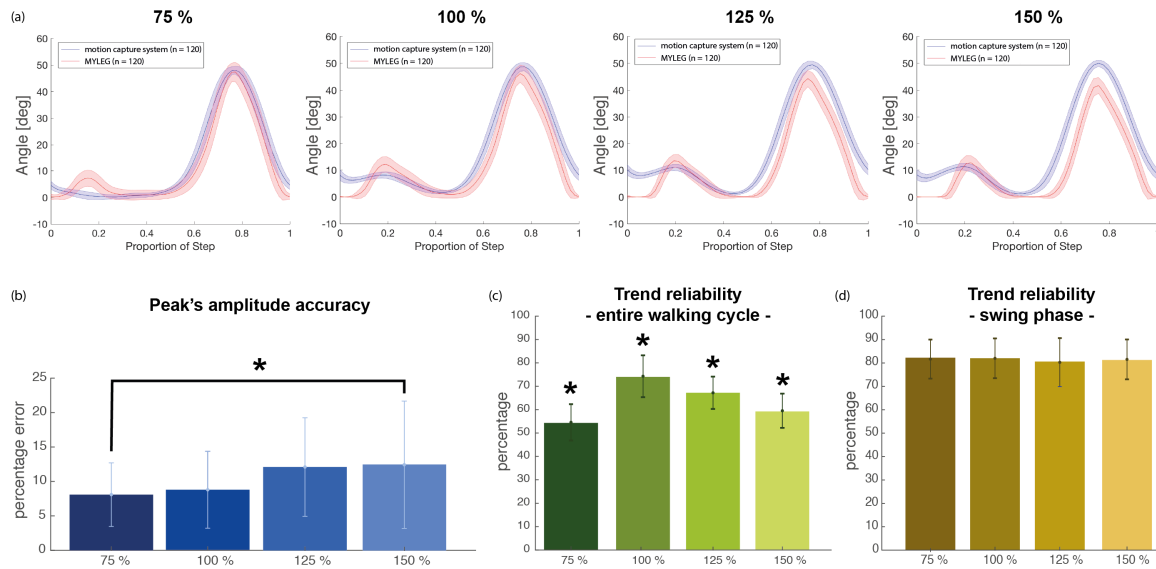
#### MYLEG accuracy during level walking at 4 different velocities

The results obtained for the subject's self-selected comfortable walking speed have been compared to that of the other 3 tested velocities. Figure 4.18 shows the main findings related to the analysis of the knee angle trends.

A slight increase in the amplitude difference between the peaks of the real and the estimated knee angle curves have been measured as velocity increases however being only the slower and the faster trends significantly different ( $p < 0.05$ ) (Figure 4.18 (b)). The mean percentage error remains small for all the 4 speeds never overcoming the 15%. Moreover, slightly greater standard deviations are associated to higher velocities. Such behaviour could be associated to a reduced number of samples describing the movement at higher velocities as well as a higher noise in the accelerometer and the gyroscope data that affects the algorithm performance.

If considering the trend reliability over the entire walking cycle, a significant difference between all the 4 considered velocities has been demonstrated ( $p \ll 0.001$ ) (Figure 4.18 (c)). However, this result does not hold any longer if only the swing phase is





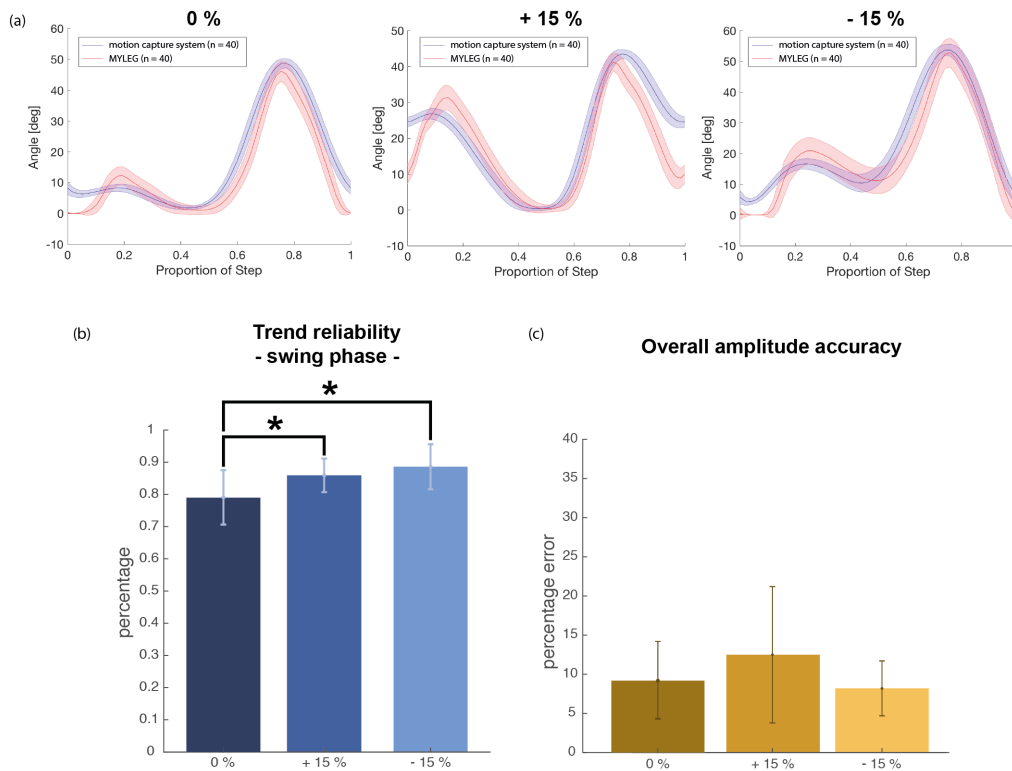
**Figure 4.18:** (a) Knee angle comparison between the data obtained using a gold standard 3D capture motion system (blue line) and the MYLEG device (red line) at 4 different velocities (100 % corresponds to the subject's self-selected comfortable walking speed); (b) amplitude difference between the peaks of the two trends at different velocities; (c - d) trend reliability between knee angle data at different velocities during the entire walking cycle and the swing phase respectively.

considered (Figure 4.18 (d)) in which an accuracy of approximately 80 % is reached for each velocity. This result confirms that the higher inaccuracy in the knee angle estimate occurs during the stance phase when the foot hits the treadmill causing the vibration of the electronic boards. Increasing the velocity, the impact on the floor becomes stronger causing a drop in the trend reliability during the stance phase. A reduced reliability at velocity 75 % could be explained by the fact that the walking pattern results unnatural when the subject is required to slow down with respect to the comfortable self-selected speed. The high accuracy in the swing phase is a very promising result considering that it corresponds to the step's portion in which the subject is provided with the stimulation. In fact, as already discussed in previous section, unwanted oscillations during the stance phase can be removed increasing the lower threshold at which the stimulation starts.

### MYLEG accuracy during inclined walking

In order to assess MYLEG accuracy in as many different scenarios as possible, inclined (+ 15 %) and declined (- 15 %) walking has been compared to ground level walking (0 %). Figures 4.19 and 4.20 show the main findings regarding the knee angle and the

force distribution, respectively. Only one trial has been performed for each task and 40 steps have been extracted and compared both for MYLEG system and the 3D motion capture and force plates system.

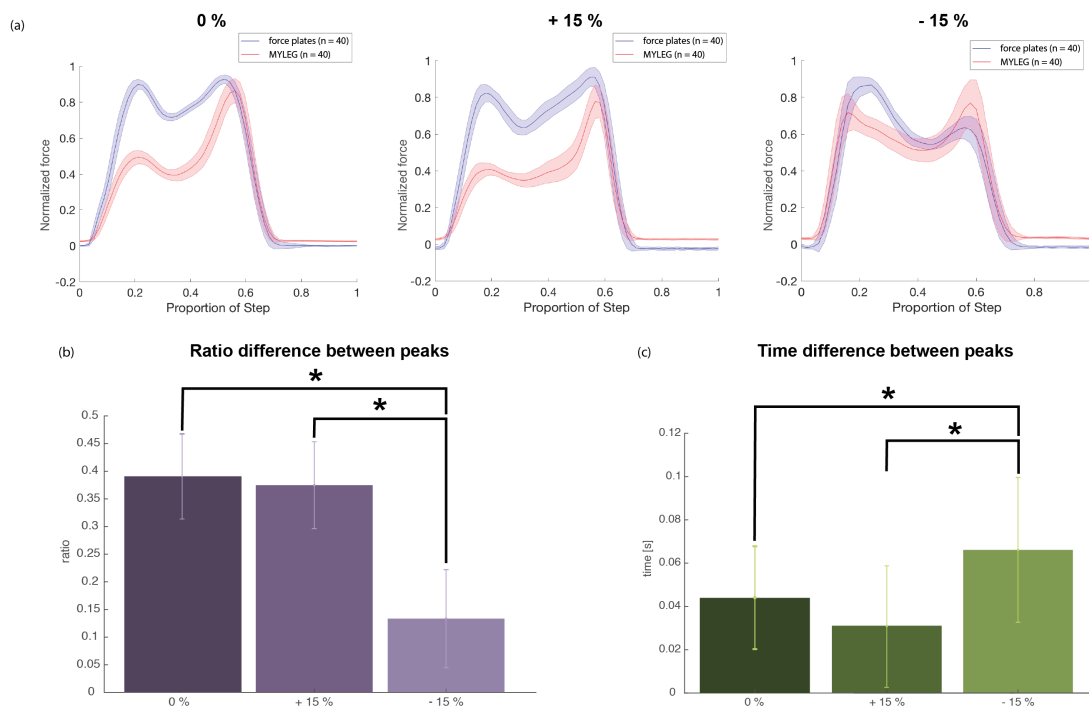


**Figure 4.19:** (a) Knee angle comparison between the data obtained using a gold standard 3D capture motion system (blue line) and the MYLEG device (red line) at 3 different inclinations (0 % = ground level walking, + 15 % = inclined walking, - 15 % = declined walking); (b) trend reliability between the knee angle data at different inclinations during the swing phase; (c) amplitude difference of the overall trends at different inclinations.

As far as the joint angle is concerned, a significantly higher trend reliability has been demonstrated both for the inclined and the declined task. Reliability of approximately 90 % in reproducing the shape of the angle are reached in the two considered cases during the swing phase, allowing for a stimulation that perfectly matches the subject's movement. In particular, it is possible to assert that the joint angle algorithm is also able to precisely follow patterns that are extremely different from that of the normal ground level walking, as per the inclined trial. A non-significantly different percentage error in the amplitude accuracy has been obtained for all the 3 tasks. The mean amplitude difference remains lower than the 15 % and the slightly higher error in the

inclined trial could be associated to a bigger range of motion of the knee joint when walking uphill.

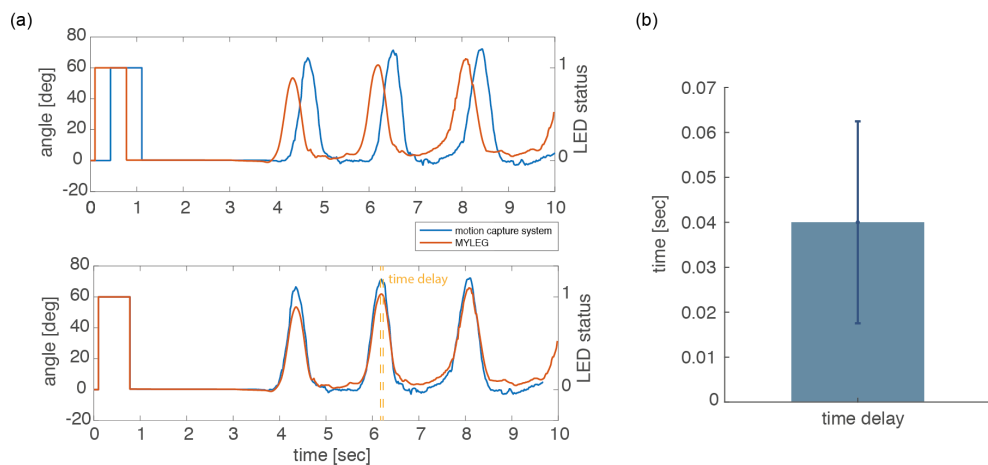
Looking at the force distribution in the 3 different scenarios, the most important finding to be noticed is the reduction in the difference of the ratio between the peaks during declined walking. This result is consistent with what was expected since, when walking downhill, in order not to get out of balance, the subject shifts his weight backwards applying a greater pressure on the heel. In this case, even if the number of sensors measuring the force applied on the heel are fewer, two activated sensors in the back of the insole measure approximately the same pressure that is calculated by the 3 sensors under the toes. This is also consistent with the higher peak measured by the force plates after heel strike.



**Figure 4.20:** (a) Force distribution comparison between the data obtained using force plates (blue line) and the MYLEG device (red line) at 3 different inclinations (0 % = ground level walking, + 15 % = inclined walking, - 15 % = declined walking); (b) difference in the peaks' ratio between knee angle trends at different inclinations; (c) time difference between the peaks at different inclinations.

## MYLEG time delay

Up to now, time delay has not been considered in the analysis for assessing the system accuracy. In fact, there was not possibility to synchronize the electronic board and the GRAIL system and get timing information from the trials performed in the GRAIL room at Balgrist University Hospital. Therefore, in order to investigate the time delay introduced by MYLEG system, single camera recordings and data post-processing using Kinovea software have been performed. The synchronization method used for aligning real and estimated trends is identical to that described in Section 4.3.1. The status of one LED was recorded by the system controller and aligned with the video frames in which the light is ON. Figure 4.21 shows a 3 steps trial before and after the synchronization process. Time delay has been calculated over 30 steps as the difference in time between the real and the estimated knee angle peak and a mean value of 40 ms is obtained. This result demonstrates that the time required for the system to send the packets from the electronic board to the system controller and process the received data is almost negligible and not perceivable by the subject which receives a stimulation in real-time which perfectly matches every movement of his prosthetic leg.



**Figure 4.21:** (a) Synchronization process between 3D motion capture system and MYLEG system; (b) time delay between the knee angle data obtained using a gold standard 3D capture motion system and the MYLEG device

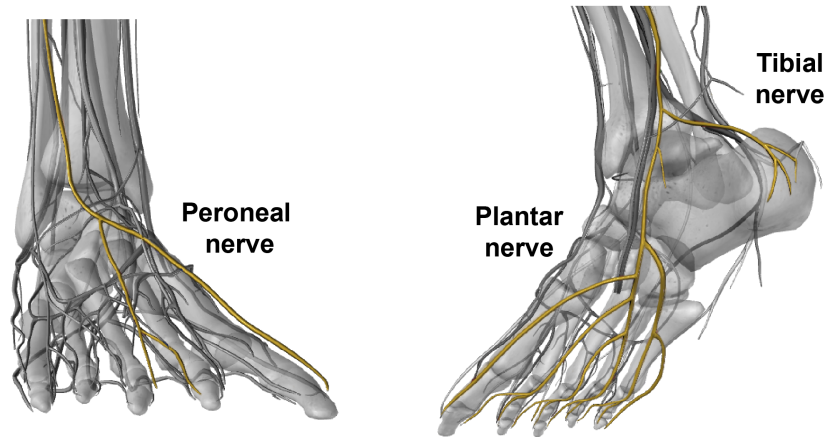
# Exploitation

---

As explained in Chapter 1, amputees do not represent the only pathological population that could benefit from MYLEG system. In fact, also people suffering from peripheral neuropathy and diabetes report problems while walking due to a lack of sensations in their feet. In fact, the nerves that carry the information from the periphery to the Central Nervous System are damaged or diseased. This condition is different to that of an amputee in the sense that diabetic patients are not missing their limb and the nerves are still present. This gives the possibility to stimulate the nerves with superficial electrodes imposing a sufficiently high current so to allow the patient to regain the sensation in the same part of the foot as it would be in presence of a natural stimulus.

Ideally, the nerves to be targeted are shown in Figure 5.1. However, the most appropriate position of the electrodes to obtain a somatotopic sensation is highly subject dependant and influenced by the severity of the nerve damage. Since most of the time the injury affects the extremities, moving the electrodes proximally above the ankle level should help the patient in feeling the stimulation however reducing the somatotopic effect.

Plantar and tibial nerves allows to generate a sensation under the toes and on the heel, respectively and they are associated to a pressure applied in the frontal part and on the back of the foot. Instead, electrodes over the peroneal nerve stimulate the dorsum



**Figure 5.1:** *Peroneal, plantar and tibial nerve to be targeted to obtain a somatotopic sensation on the dorsum, under the toes and on the heel respectively*

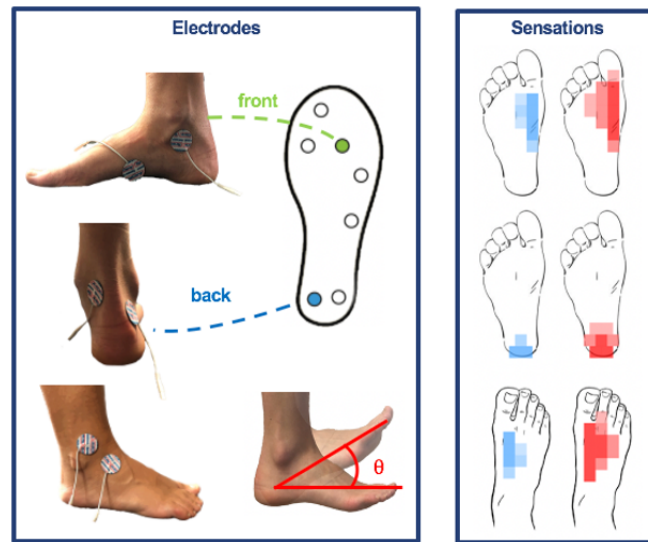
of the foot. This sensation is considered to be the closest to the feeling associated to ankle dorsiflexion and it is therefore used to restore feedback on the ankle joint providing a stimulation which is proportional to the angle of the ankle. In fact, diabetes and PN related problems in walking are usually associated to muscle weakness at the ankle [45], reduced ankle mobility [46] and decreased ankle proprioception sense [47]. Because of this, restoring information about the proprioception of the ankle to diabetic patients was considered more appropriate than giving back the knee angle values.

Figure 5.2 shows the placement of the electronic boards in case of diabetic patient. In order to provide the angle of the ankle, the algorithm that calculate the joint angle has been slightly modified considering the change in the axis orientation due to a rotation of the box that was previously attached to the thigh.



**Figure 5.2:** *Two electronic boards placed over the foot of a diabetic subject to measure the exerted forces and the ankle joint angle.*

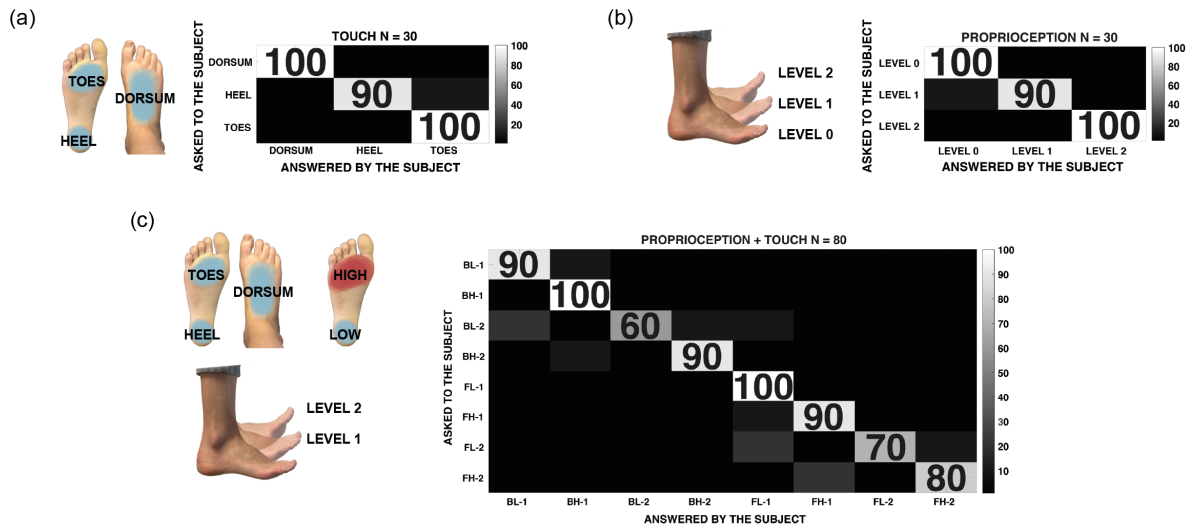
Electrode placement and the corresponding elicited sensations are shown in Figure 5.3 and represent the ideal stimulation that should be achieved during the calibration. The blue and red spots depict the location of the stimulation reported by the subject when asked for a LOW and a HIGH sensation.



**Figure 5.3:** *Electrode placement and corresponding sensations when stimulating plantar, tibial and peroneal nerve.*

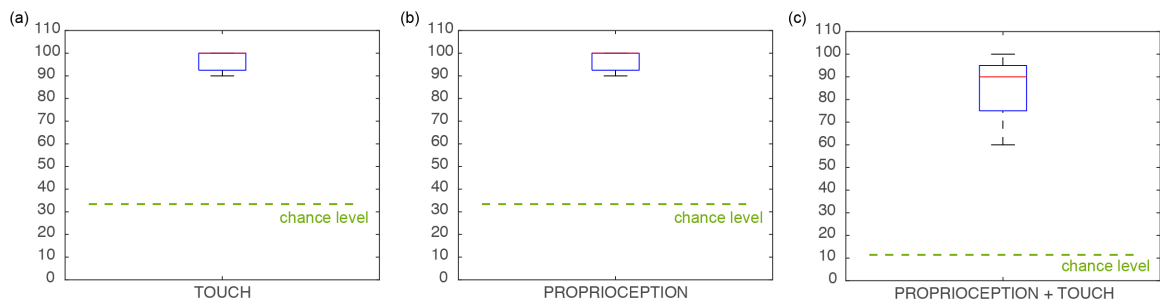
While stimulation on diabetic subjects had already been performed for other experiments in the Neuroengineering Laboratory and electrodes were successfully placed over the foot of the subject to elicit a somatotopic sensation, no subject could be recruited for testing MYLEG device. Thus, in order to assess its functionality and feasibility in the new context, the ability of a healthy subject to discriminate different locations and different levels of stimulation has been evaluated. The subject was blindfolded and acoustically isolated and asked to distinguish between different sensations.

The different scenarios and the corresponding results are shown in figure 5.4. In the first trial the subject was asked to distinguish between the 3 different locations; in the second trial 3 different levels of ankle proprioception were provided to the subject; in the third trial, the two conditions were bound together requiring the subject to also discriminate the intensity of the pressure on the insole.



**Figure 5.4:** Capability of a healthy subject to distinguish between (a) different locations, (b) different stimulation intensities and (c) different locations and intensities combined together.

In all cases, the obtained answers are much higher with respect to the chance level, ruling out the possibility that the subject was guessing the answer and firmly confirm his capability to discriminate location and level of stimulation.



**Figure 5.5:** Exploitation results for (a) touch, (b) proprioception and (c) the combination of the two.



# Conclusions

This chapter presents final considerations on the project as well as an insight in the possible applications, future developments and current limitations.

The objectives defined as aim of the project in Chapter 2.3 have been totally fulfilled. Two functioning PCBs have been designed, printed, assembled and tested in many different scenarios encountering no problems related to the electronics. Moreover, the main issues associated with the original board has been overcome obtaining a lighter, smaller, faster and longer-lasting device. A comparison of the main aspects of the two circuits is listed in Table 6.1.

**Table 6.1:** Comparison between original and new electronic circuit characteristics

Parameters	Original board	New MYLEG circuit
Dimensions	78 x 65 x 41 mm	69 x 49 x 38 mm
Weight	800 g	100 g
Battery duration	4 hours	> 12 hours
Temperature	N/A	20 - 25 °C (*)
Bluetooth	10 seconds to connect 16 packets lost in 15 minutes	1.6 seconds to connect 0 packets lost in 15 minutes
Time delay	120 ms	40 ms
Reprogramming	✗	✓
Synchronization	✗	✓
Splash water	✓	✓

(\*) after 12 hours of continuous usage

A fully portable, light and comfortable design has been achieved allowing for the real-time restoration of sensory feedback in different pathological populations. Amputees and diabetic patients have been considered due to the lack of sensation in the extremities, but the usage of MYLEG system could be in general extended to all pathological conditions that cause abnormalities in the walking pattern, such as stroke and Parkinson's disease. In fact, receiving a feedback proportional to the force applied over the feet or to the degree of enclosure of the knee could help in restoring a more symmetric walking pattern. The enlargement of the target population is made possible by the new implementation of a two-leg simultaneous stimulation which were not considered for amputees but could be extremely useful for diabetic or stroke patients whose legs are both impaired.

The main limitation that still persists in the new MYLEG system is related to the stability of the Bluetooth connection between the electronic board and the system controller. In fact, sudden disconnections between the two devices seldomly but unexpectedly happen. This problem could be solved by reducing the number of transmitted packets or by replacing the Bluetooth dongle (Mediatek Ralink RT5370N) that integrates Bluetooth feature into ODROID-C2 with a newer version to increase the data rate of the receiver. In order to improve the quality of the collected data, a better way to tighten the electronic board to the patient's leg should be investigated, probably changing the 3D printed box design to add more Velcro straps. Finally, a higher number of sensors should be embedded in the sensorized insole for obtaining a more accurate force distribution. The underestimate of the first peak of the force distribution has been solved in the literature by applying a least square method to assign specific weight to the contribution of each sensor [48]. However, this calibration process is highly time consuming since it has to be repeated for every subject every time the insole is worn and requires force plates to measure the real applied force. Therefore, it is inapplicable to clinical and experimental use scenario. Moreover, it is important to remember that a lower estimated force peak at the heel strike does not affect in any way the accuracy of the stimulation perceived by the subject while walking.

At the present stage of development, the higher priority of the system is to finalize the product for home-usage in the everyday life. For achieving this goal, more prototypes have to be printed and tested and a more user-friendly Graphical User Interface has to be developed providing the patient with the possibility to easily activate and control the system and adjust the simulation parameters.

In fact, the highly promising results described in Section 4.3.3 not only allows to restore accurately and in real-time sensory feedback to the patient but also gives the possibility to use MYLEG device for clinical monitoring and data collection during everyday life activities. Using MYLEG system, the clinician could extract many parameters of interest in describing the walking patter of the patient. In particular, MYLEG system provides the exact number of steps performed by the subject and an extremely precise information about the timing of each steps and the duration of each swing and stance phase. No precise information about the load applied on the leg can be directly inferred from the system but a comparison between the output of two systems applied to each of the patient's legs could provide an accurate overview of the main features of the gait, discriminating between symmetric and asymmetric walking patterns. Similar information is obtained by comparing the knee angle traces of the two legs. Finally, by analysing the trace for one leg over time is possible to investigate improvements in the walking pattern, studying the variability of the joint angle traces to infer an increased or decreased confidence and proprioceptive awareness of the patient while walking.

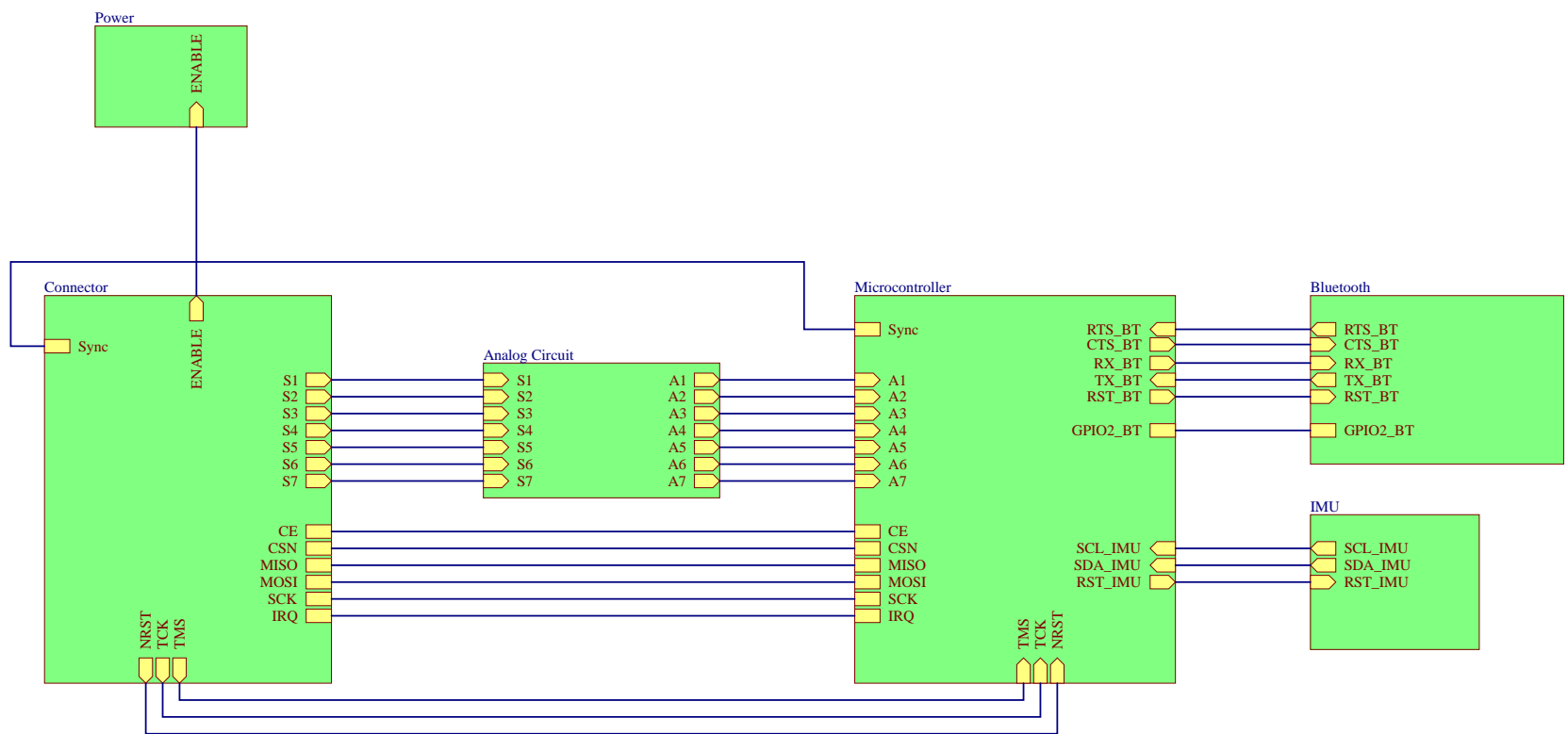
Thanks to its highly innovative technology and with the aim of pushing research in the leg prosthesis field to the next level, MYLEG system will participate in CYBATHLON 2020, an international competition in which disabled people compete against each other to complete daily-life activities wearing advanced robotics and cutting-edge assistive technologies.




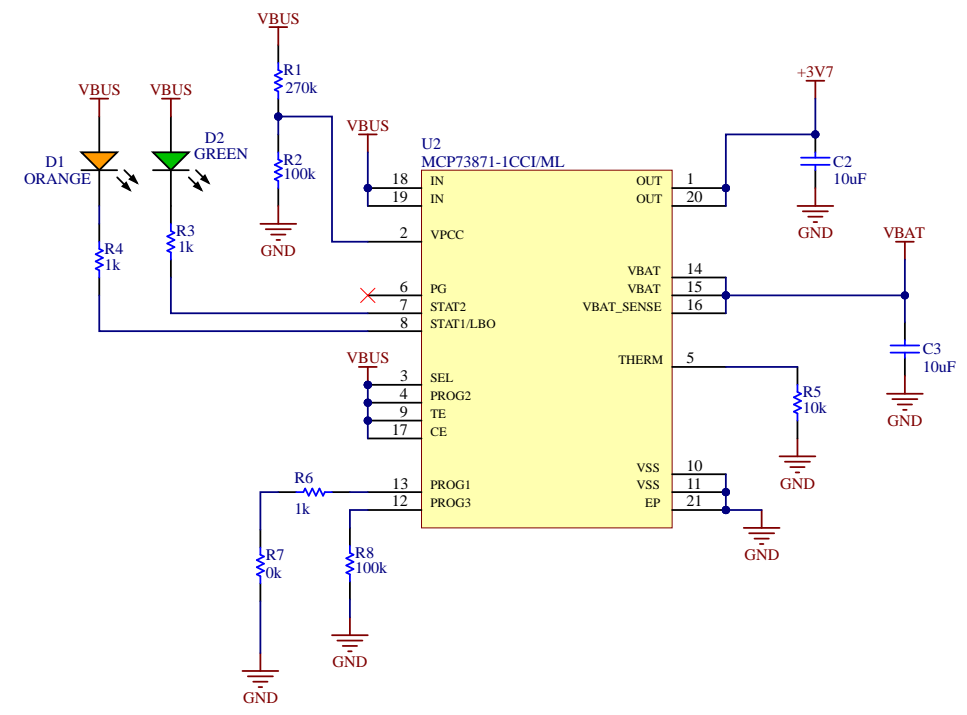
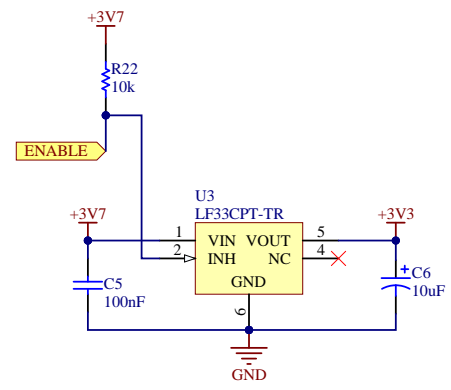
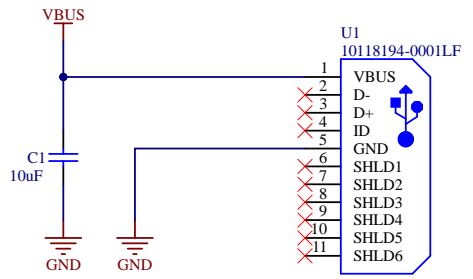
# PCB schematic


---

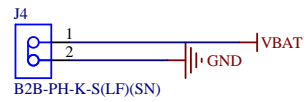
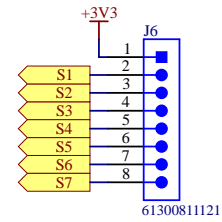
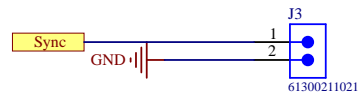
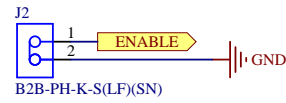
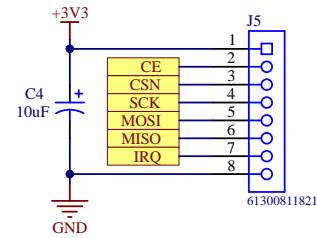
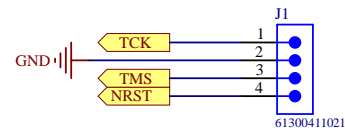
The PCB schematics have been exported from Altium Designer. The name of the PCB the schematic refers to is reported in the title block at the bottom right. The first page of each schematic shows the general connection between components and the connected PIN name are labelled. Then, the components are classified into Power, Connectors, Analogic circuit (only in ankle PCB), Microcontroller, Bluetooth (only in ankle PCB) and IMU. Each sheet highlights the connections and the additional parts (e.g. resistors, capacitors, LEDs, crystal, etc.) that the main components need to properly function.



 <b>Eidgenössische Technische Hochschule Zürich</b> <b>Swiss Federal Institute of Technology Zurich</b>		Drawing title: <h1 style="color: red; text-align: center;">Ankle PCB</h1>	
Drawing part: Schematic	Rev: V1.1	Format: A4	Institute: NeuroEng Lab
Date: 10/19/2020 5:20:42 PM		Creator: Chiara Basla	Project: Schematic.SchDoc
File: C:\Users\Chiara\Desktop\Sensorised insole\Ankle PCB\Schematic.SchDoc		Sheet 1 of 7	



		Drawing title:	
Eidgenössische Technische Hochschule Zürich Swiss Federal Institute of Technology Zurich		<h1>Ankle PCB</h1>	
Drawing part: Power	Rev: V1.1	Format: A4	Institute: NeuroEng Lab
Date: 10/19/2020 5:20:42 PM		Creator: Chiara Basla	Project: Power.SchDoc
File: C:\Users\Chiara\Desktop\Sensorised insole\Ankle PCB\Power.SchDoc		Sheet 2	of 7



**ETH**

Eidgenössische Technische Hochschule Zürich  
Swiss Federal Institute of Technology Zurich

Drawing title:

**Ankle PCB**

Drawing part: Connectors

Rev: V1.1

Format:

Institute: NeuroEng Lab

Project: Connector.SchDoc

Date: 10/19/2020 5:20:42 PM

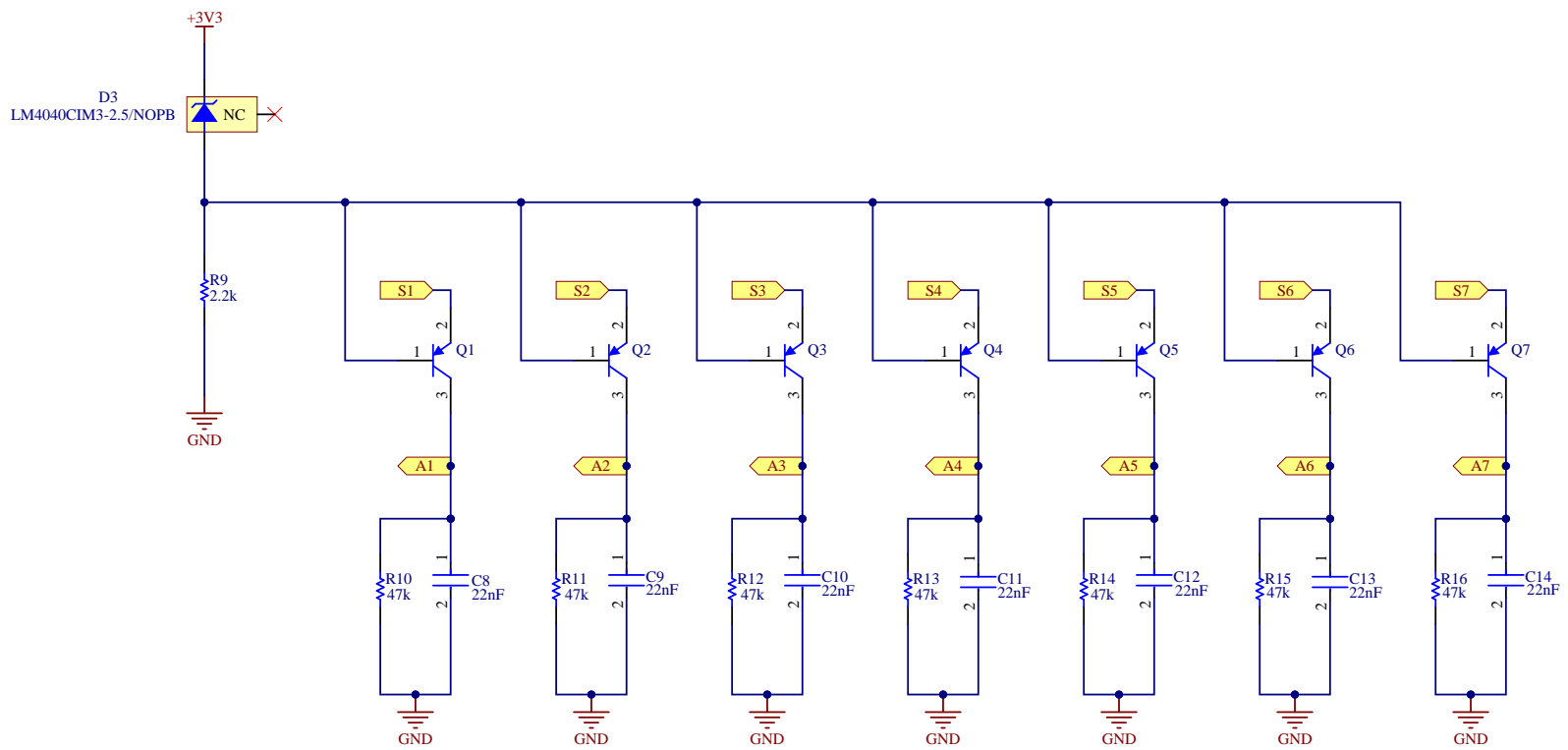
A4

Creator: Chiara Basla

Sheet 3 of 7

File: C:\Users\Chiara\Desktop\Sensorised insole\Ankle PCB\Connector.SchDoc





**ETH**  
 Eidgenössische Technische Hochschule Zürich  
 Swiss Federal Institute of Technology Zurich

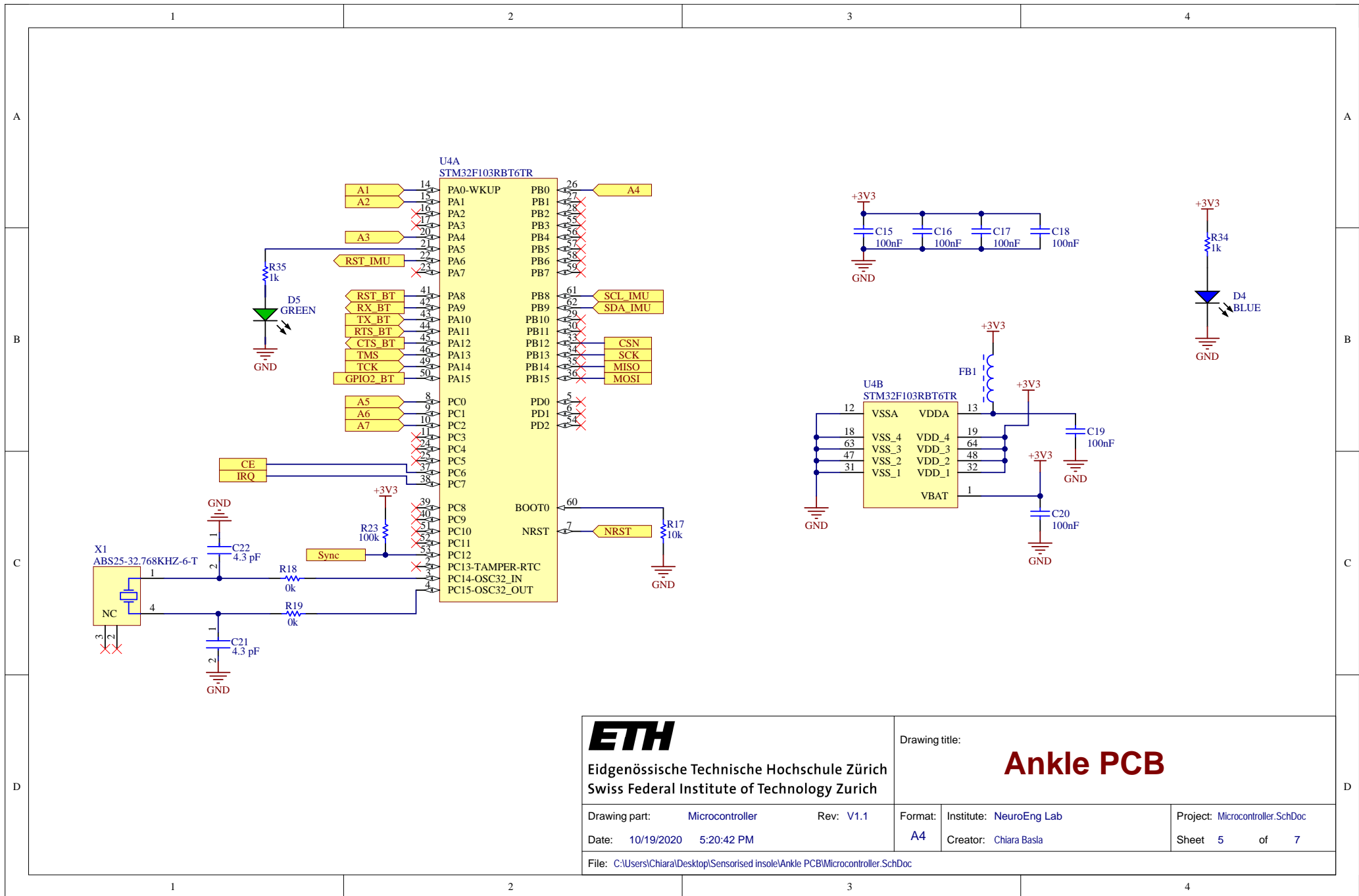
Drawing title:  
**Ankle PCB**

Drawing part: Analog circuit      Rev: V1.1  
 Date: 10/19/2020 5:20:42 PM

Format: A4  
 Institute: NeuroEng Lab  
 Creator: Chiara Basla

Project: Analog Circuit.SchDoc  
 Sheet 4 of 7

File: C:\Users\Chiara\Desktop\Sensorised insole\Ankle PCB\Analog Circuit.SchDoc



**ETH**  
 Eidgenössische Technische Hochschule Zürich  
 Swiss Federal Institute of Technology Zurich

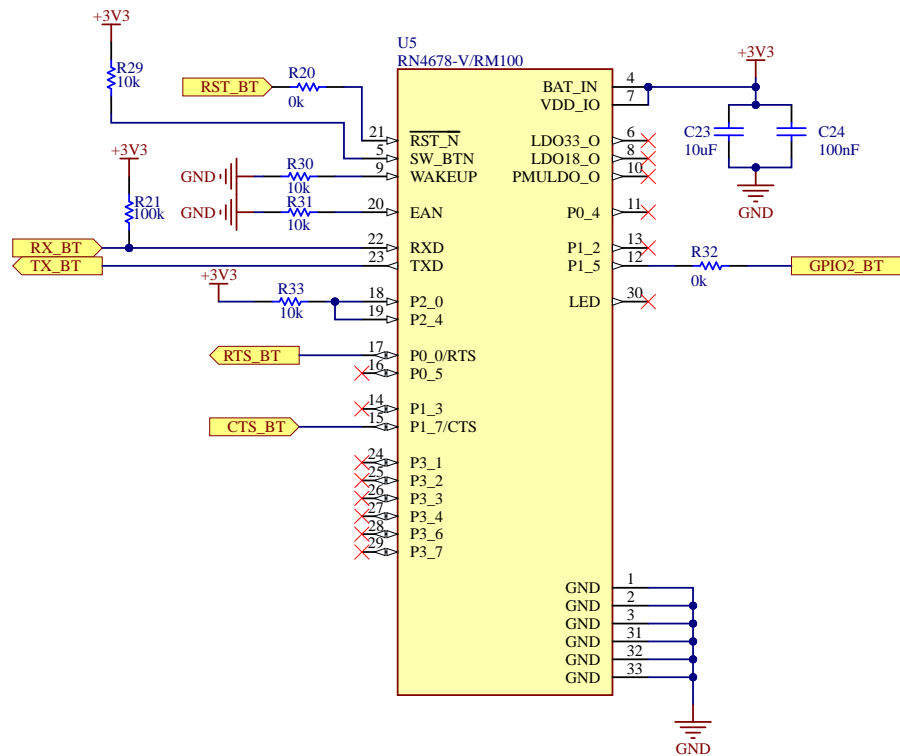
Drawing title:  
**Ankle PCB**

Drawing part: Microcontroller Rev: V1.1  
 Date: 10/19/2020 5:20:42 PM

Format: A4  
 Institute: NeuroEng Lab  
 Creator: Chiara Basla

Project: Microcontroller.SchDoc  
 Sheet 5 of 7

File: C:\Users\Chiara\Desktop\Sensorised insole\Ankle PCB\Microcontroller.SchDoc



**ETH**

Eidgenössische Technische Hochschule Zürich  
Swiss Federal Institute of Technology Zurich

Drawing title:

**Ankle PCB**

Drawing part: Bluetooth

Rev: V1.1

Format:

Institute: NeuroEng Lab

Project: Bluetooth.SchDoc

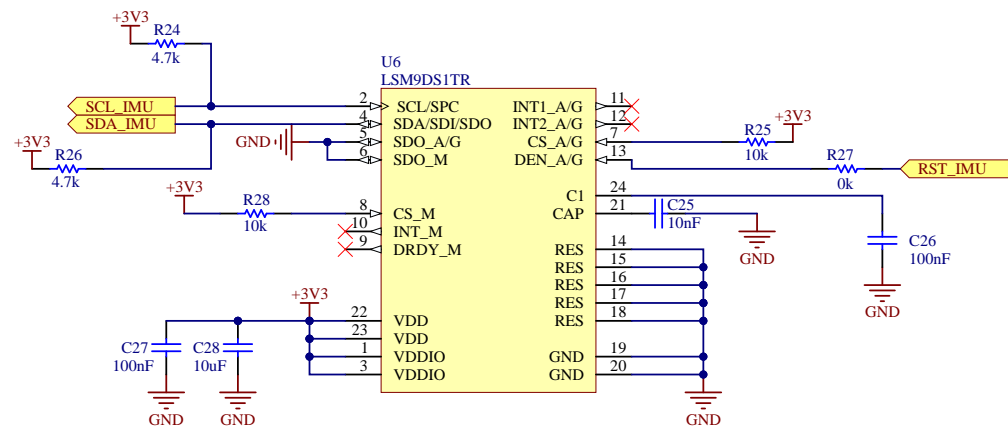
Date: 10/19/2020 5:20:42 PM

A4

Creator: Chiara Basla

Sheet 6 of 7

File: C:\Users\Chiara\Desktop\Sensorised insole\Ankle PCB\Bluetooth.SchDoc



**ETH**

Eidgenössische Technische Hochschule Zürich  
Swiss Federal Institute of Technology Zurich

Drawing title:

**Ankle PCB**

Drawing part: IMU

Rev: V1.1

Format:

Institute: NeuroEng Lab

Project: IMU.SchDoc

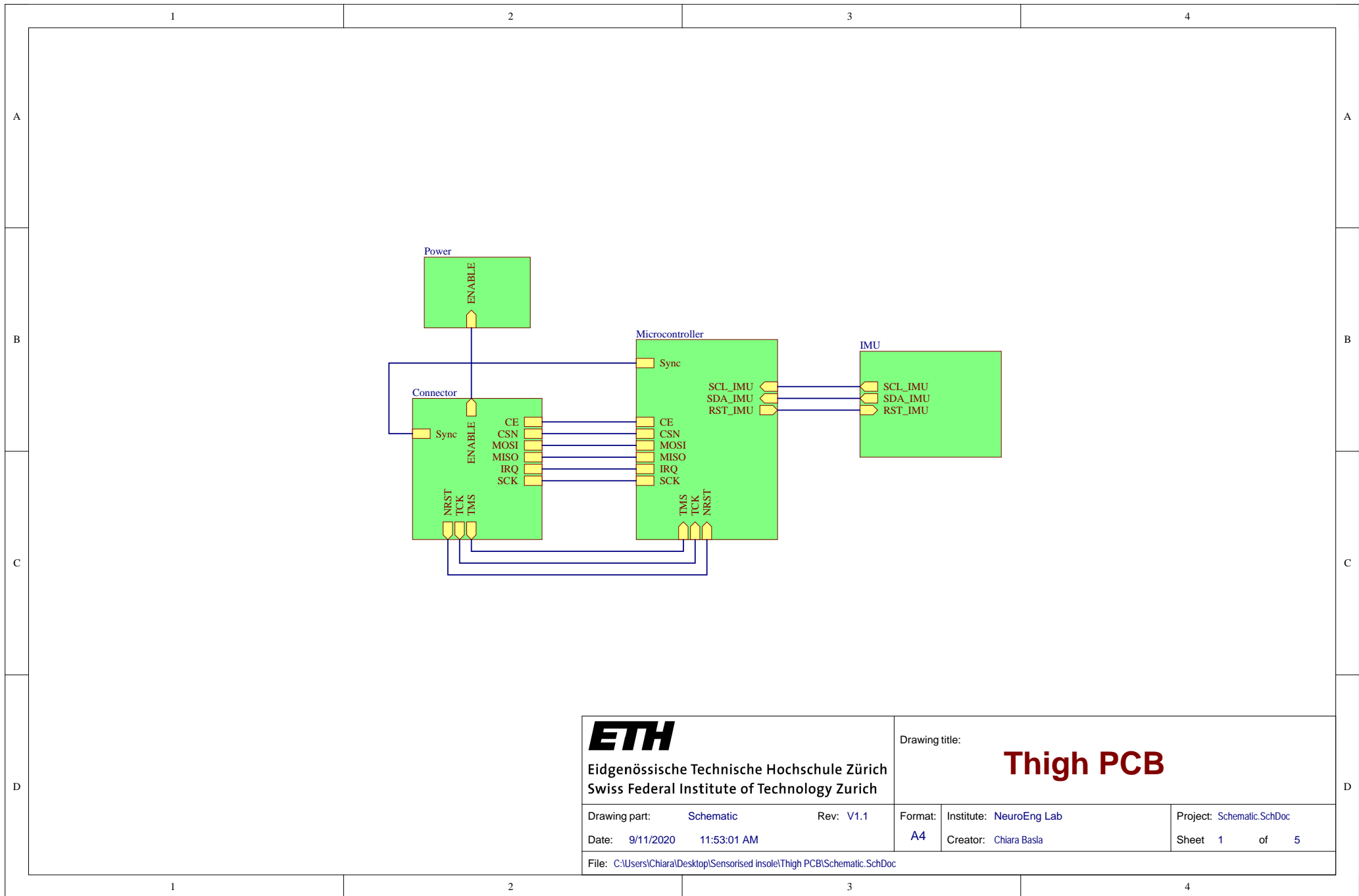
Date: 10/19/2020 5:20:42 PM

A4

Creator: Chiara Basla

Sheet 7 of 7

File: C:\Users\Chiara\Desktop\Sensorised insole\Ankle PCB\IMU.SchDoc



Eidgenössische Technische Hochschule Zürich  
 Swiss Federal Institute of Technology Zurich

Drawing title:

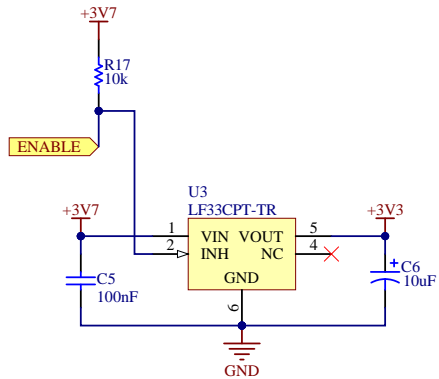
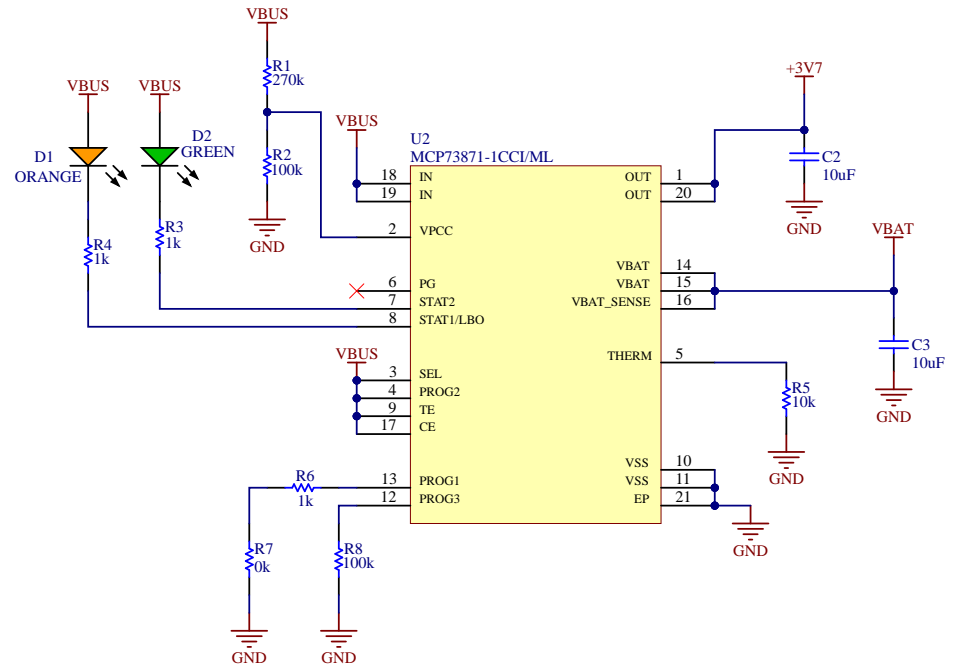
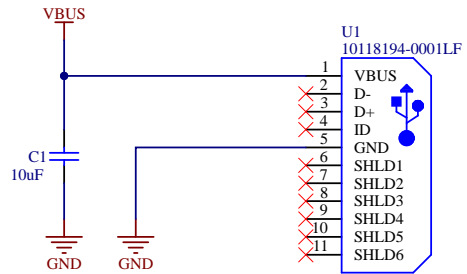
**Thigh PCB**

Drawing part: Schematic Rev: V1.1  
 Date: 9/11/2020 11:53:01 AM

Format: A4  
 Institute: NeuroEng Lab  
 Creator: Chiara Basla

Project: Schematic.SchDoc  
 Sheet 1 of 5

File: C:\Users\Chiara\Desktop\Sensorised insole\Thigh PCB\Schematic.SchDoc



**ETH**

Eidgenössische Technische Hochschule Zürich  
Swiss Federal Institute of Technology Zurich

Drawing title:

**Thigh PCB**

Drawing part: Power

Rev: V1.1

Format:

Institute: NeuroEng Lab

Project: Power.SchDoc

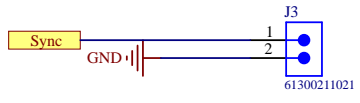
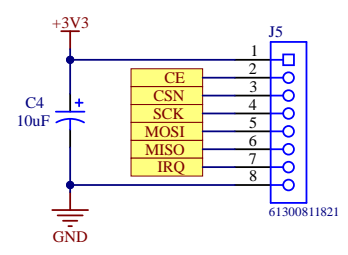
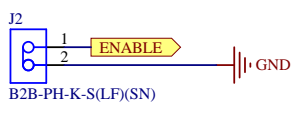
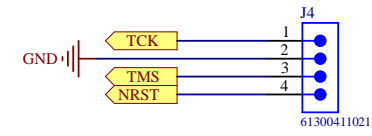
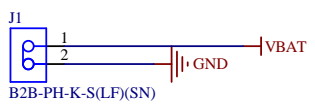
Date: 9/11/2020 11:53:01 AM

A4

Creator: Chiara Basla

Sheet 2 of 5

File: C:\Users\Chiara\Desktop\Sensorised insole\Thigh PCB\Power.SchDoc



**ETH**  
Eidgenössische Technische Hochschule Zürich  
Swiss Federal Institute of Technology Zurich

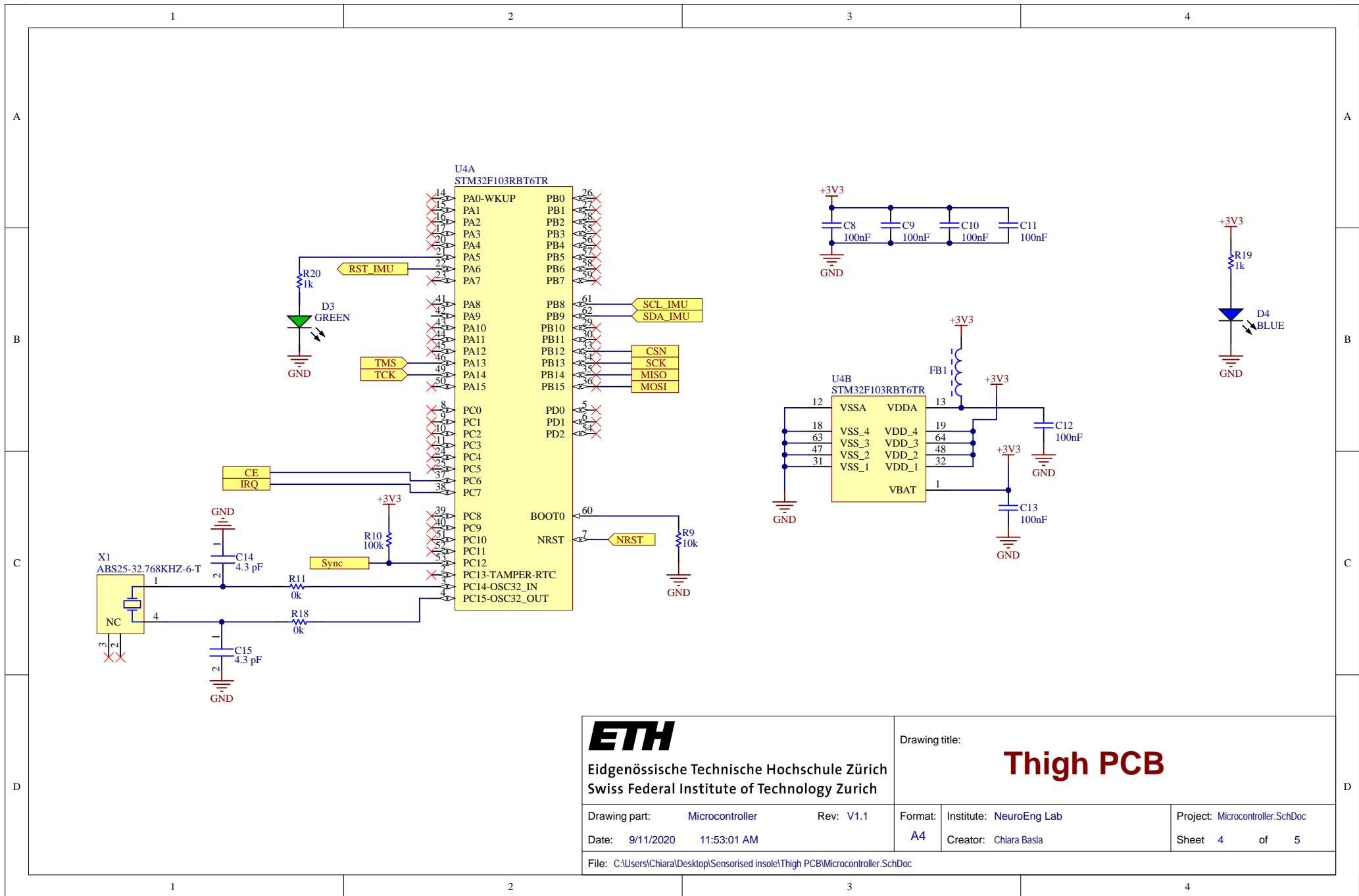
Drawing title:  
**Thigh PCB**

Drawing part: Connector Rev: V1.1  
Date: 9/11/2020 11:53:01 AM

Format: A4  
Institute: NeuroEng Lab  
Creator: Chiara Basla

Project: Connector.SchDoc  
Sheet 3 of 5

File: C:\Users\Chiara\Desktop\Sensorised insole\Thigh PCB\Connector.SchDoc



**ETH**  
 Eidgenössische Technische Hochschule Zürich  
 Swiss Federal Institute of Technology Zurich

Drawing title:  
**Thigh PCB**

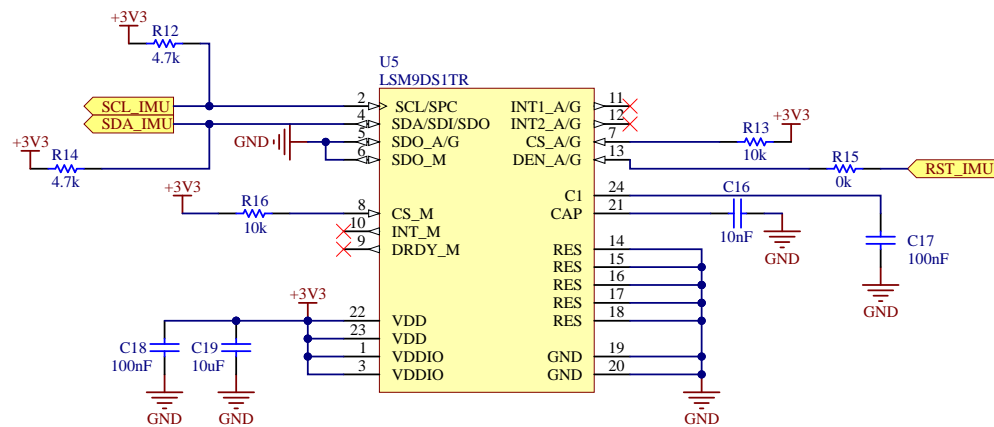
Drawing part: Microcontroller  
 Date: 9/11/2020 11:53:01 AM

Rev: V1.1  
 Format: A4  
 Institute: NeuroEng Lab  
 Creator: Chiara Basla

Project: Microcontroller.SchDoc  
 Sheet 4 of 5

File: C:\Users\Chiara\Desktop\Sensorised insole\Thigh PCB\Microcontroller.SchDoc





**ETH**

Eidgenössische Technische Hochschule Zürich  
Swiss Federal Institute of Technology Zurich

Drawing title:

**Thigh PCB**

Drawing part: IMU Rev: V1.1  
Date: 9/11/2020 11:53:01 AM

Format: A4  
Institute: NeuroEng Lab  
Creator: Chiara Basla

Project: IMU.SchDoc  
Sheet 5 of 5

File: C:\Users\Chiara\Desktop\Sensorised insole\Thigh PCB\IMU.SchDoc



# Bill of materials

---

The bill of materials (BOM) is a comprehensive inventory of all the components needed to manufacture the PCBs. The list comprises the designator as per the Altium schematic (see Appendix A), the part number, the footprint and the quantity of each component.

## B.1 Ankle box

Designator	Part number	Description	Footprint	Quantity
C1, C2, C3, C23, C28	CC0805KKX5R6BB106	Chip Capacitor, 10 uF, +/- 10%, 10 V, -55 to 85 degC, 0805 (2012 Metric), RoHS, Tape and Reel	CAPC2013X145X50LL20T25	5
C5, C15, C16, C17, C18, C19, C20, C24, C26, C27	CC0603KRX7R9BB104	Chip Capacitor, 100 nF, +/- 10%, 50 V, -55 to 125 degC, 0603 (1608 Metric), RoHS, Tape and Reel	CAPC1608X90X40NL10T20	10
C4, C6	50SVF10M	10µF 50V Aluminum - Polymer Capacitors Radial, Can - SMD 40mOhm 1000 Hrs @ 125°C	CAPAE660X600N	2
C8, C9, C10, C11, C12, C13, C14	C0603C223K5RACTU	Ceramic Capacitor 0.022uF 50V, X7R, 10%, 0603, Full Reel	FP-C0603C-CF-MFG	7
C21, C22	C0603C439D5GAC7867	CAP CER 4.3PF 50V NP0 0603	FP-C0603C-CF-MFG	2
C25	GRM155R71C103KA01D	Chip Capacitor, 10 nF, 16 V, 10%, -55 to 125 degC, 0402 (1005 Metric), RoHS, Tape and Reel	CAPC1005X55X25LL05T10	1
D1	APG1608SEKC/T	LED, SMT, 0603(1608), 0.25mm Thickness, Super Bright Orange	KING-LED0603-25-ORANGE_V	1
D2, D5	APG1608CGKC/T	LED, SMT, 0603(1608), 0.25mm Thickness, Green	KING-LED0603-25-GREEN_V	2
D3	LM4040CIM3-2.5/NOPB	Precision Micropower Shunt Voltage Reference, 3-pin SOT-23, Pb-Free	MF03A_N	1
D4	APT1608QBC/D	Chip LED Lamp, Blue, 5 V, 30 mA, -40 to 85 degC, 2-Pin SMD, RoHS, Tape and Reel	KING-APT1608QBCD_V	1
FB1	BLM18EG601SN1D	Chip Ferrite Bead for GHz Band General Use (Low DC Resistance Type), 600 Ohm, 500 mA, -55 to 125 degC, 1.6 x 0.8 x 0.95 mm SMD, Tape and Reel	MURA-BLM18-RF-H4-CHIP-2_V	1
J1	61300411021	WR-PHD Pin Header, THT, pitch 2.54mm, Single Row, Angled, 4pin	61300411021	1
J2, J4	B2B-PH-K-S(LF)(SN)	Male Header, Pitch 2 mm, 1 x 2 Position, Height 6 mm, Tail Length 3.4 mm, -25 to 85 degC, RoHS, Bulk	JST-B2B-PH-K-S_V	2
J3	61300211021	WR-PHD Pin Header, THT, pitch 2.54mm, Single Row, Angled, 2pin	61300211021	1
J5	61300811821	THT Vertical Socket Header WR-PHD, Pitch 2.54 mm, Single Row, 8 pins	61300811821	1
J6	61300811121	THT Vertical Pin Header WR-PHD, Pitch 2.54 mm, Single Row, 8 pins	61300811121	1
Q1, Q2, Q3, Q4, Q5, Q6, Q7	MMBT3906LT1G	General Purpose Transistor, PNP Silicon, 3-Pin SOT-23, Pb-Free, Tape and Reel	ONSC-SOT-23-3-318-08_V	7
R1	ERJ-3EKF2703V		RESC1608X55X30NL15T15	1
R2, R8, R21, R23	RC0603FR-07100KL	Chip Resistor, 100 KOhm, +/- 1%, 0.1 W, -55 to 155 degC, 0603 (1608 Metric), RoHS, Tape and Reel	RESC1608X55X25ML10T15	4
R3, R4, R6, R34, R35	RC0603FR-071KL	Chip Resistor, 1 KOhm, +/-1%, 0.1 W, -55 to 155 degC, 0603 (1608 Metric), RoHS, Tape and Reel	RESC1608X55X25NL10T15	5
R5, R17, R22, R25, R28, R29, R30, R31, R33	AC0603FR-0710KL		RESC1608X55X25LL10T15	9
R7, R18, R19, R20, R27, R32	RC0603JR-070RL	Chip Resistor, 0 Ohm, +/- 5%, 0.1 W, -55 to 155 degC, 0603 (1608 Metric), RoHS, Tape and Reel	RESC1608X55X25ML10T15	6
R9	CRCW06032K20FKEA		RESC1609X50X30NL10T20	1
R10, R11, R12, R13, R14, R15, R16	RC0805FR-0747KL	Chip Resistor, 47 KOhm, +/- 1%, 0.125 W, -55 to 155 degC, 0805 (2012 Metric), RoHS, Tape and Reel	RESC2013X60X35NL10T20	7
R24, R26	RC0603JR-074K7L	Chip Resistor, 4.7 KOhm, +/- 5%, 100 mW, -55 to 155 degC, 0603 (1608 Metric), RoHS, Tape and Reel	RESC1608X55X25ML10T15	2
U1	10118194-0001LF	Micro USB B Type Receptacle, 1.8 A, -55 to 85 degC, 5-Pin SMD, RoHS, Tape and Reel	FCI-10118194-0001LF-5_V	1
U2	MCP73871-ICCI/ML		MY BATTERY CHARGER	1
U3	LF33CPT-TR	500mA, Very Low Drop (0.45V) Voltage Regulator, 3.3V, 5-Pin PPAK, Tape and Reel	PPAK_L	1
U4	STM32F103RBT6TR	ARM Cortex-M3 32-bit MCU, 128 KB Flash, 20 KB Internal RAM, 51 I/Os, 64-pin LQFP, -40 to 85 degC, Tape and Reel	STM-LQFP64_V	1
U5	RN4678-V/RM100	Bluetooth Bluetooth v5.0 Transceiver Module 2.4GHz Integrated, Chip Surface Mount	MODULE_RN4678-V/RM100	1
U6	LSM9DS1TR	iNEMO Inertial Module: 3D Accelerometer, 3D Gyroscope, 3D Magnetometer, 1.9 to 3.6 V, -40 to 85 degC, 24-Pin LGA, RoHS, Tape and Reel	STM-LGA-24_3500X3000X1000	1
X1	ABS25-32.768KHZ-6-T	Low Frequency Crystal, 32.768 KHz, 6 pF, +/- 20 ppm, -40 to 85 degC, 4-Pin SMD, RoHS, Tape and Reel	ABRA-ABS25-4_V	1

## B.2 Thigh box

Designator	Part number	Description	Footprint	Quantity
C1, C2, C3, C19	CC0805KXX5R6BB106	Chip Capacitor, 10 uF, +/- 10%, 10 V, -55 to 85 degC, 0805 (2012 Metric), RoHS, Tape and Reel	CAPC2013X145X50LL20T25	4
C4, C6	50SVF10M	10µF 50V Aluminum - Polymer Capacitors Radial, Can - SMD 40mOhm 1000 Hrs @ 125°C	*CAPAE660X600N	2
C5, C8, C9, C10, C11, C12, C13, C17, C18	CC0603KRX7R9BB104	Chip Capacitor, 100 nF, +/- 10%, 50 V, -55 to 125 degC, 0603 (1608 Metric), RoHS, Tape and Reel	CAPC1608X90X40NL10T20	9
C14, C15	C0603C439D5GAC7867	CAP CER 4.3PF 50V NP0 0603	FP-C0603C-CF-MFG	2
C16	CL05B103KB5VPNC		CAPC0603X33X15ML03T05	1
D1	APG1608SEKC/T	LED, SMT, 0603(1608), 0.25mm Thickness, Super Bright Orange	KING-LED0603-25-ORANGE_V	1
D2, D3	APG1608CGKC/T	LED, SMT, 0603(1608), 0.25mm Thickness, Green	KING-LED0603-25-GREEN_V	2
D4	APT1608QBC/D	Chip LED Lamp, Blue, 5 V, 30 mA, -40 to 85 degC, 2-Pin SMD, RoHS, Tape and Reel	KING-APT1608QBCD_V	1
FB1	BLM18EG601SN1D	Chip Ferrite Bead for GHz Band General Use (Low DC Resistance Type), 600 Ohm, 500 mA, -55 to 125 degC, 1.6 x 0.8 x 0.95 mm SMD, Tape and Reel	MURA-BLM18-RF-H4-CHIP-2_V	1
J1, J2	B2B-PH-K-S(LF)(SN)	Male Header, Pitch 2 mm, 1 x 2 Position, Height 6 mm, Tail Length 3.4 mm, -25 to 85 degC, RoHS, Bulk	JST-B2B-PH-K-S_V	2
J3	61300211021	WR-PHD Pin Header, THT, pitch 2.54mm, Single Row, Angled, 2pin	61300211021	1
J4	61300411021	WR-PHD Pin Header, THT, pitch 2.54mm, Single Row, Angled, 4pin	61300411021	1
J5	61300811821	THT Vertical Socket Header WR-PHD, Pitch 2.54 mm, Single Row, 8 pins	61300811821	1
R1	ERJ-3EKF2703V		RESC1608X55X30NL15T15	1
R2, R8, R10	RC0603FR-07100KL	Chip Resistor, 100 KOhm, +/- 1%, 0.1 W, -55 to 155 degC, 0603 (1608 Metric), RoHS, Tape and Reel	RESC1608X55X25ML10T15	3
R3, R4, R6, R19, R20	RC0603FR-071KL	Chip Resistor, 1 KOhm, +/-1%, 0.1 W, -55 to 155 degC, 0603 (1608 Metric), RoHS, Tape and Reel	RESC1608X55X25NL10T15	5
R5, R9, R13, R16, R17	AC0603FR-0710KL		RESC1608X55X25LL10T15	5
R7, R11, R15, R18	RC0603JR-070RL	Chip Resistor, 0 Ohm, +/- 5%, 0.1 W, -55 to 155 degC, 0603 (1608 Metric), RoHS, Tape and Reel	RESC1608X55X25ML10T15	4
R12, R14	RC0603JR-074K7L	Chip Resistor, 4.7 KOhm, +/- 5%, 100 mW, -55 to 155 degC, 0603 (1608 Metric), RoHS, Tape and Reel	RESC1608X55X25ML10T15	2
U1	10118194-0001LF	Micro USB B Type Receptacle, 1.8 A, -55 to 85 degC, 5-Pin SMD, RoHS, Tape and Reel	FCI-10118194-0001LF-5_V	1
U2	MCP73871-1CCI/ML		MY BATTERY CHARGER	1
U3	LF33CPT-TR	500mA, Very Low Drop (0.45V) Voltage Regulator, 3.3V, 5-Pin PPAK, Tape and Reel	PPAK_L	1
U4	STM32F103RBT6TR	ARM Cortex-M3 32-bit MCU, 128 KB Flash, 20 KB Internal RAM, 51 I/Os, 64-pin LQFP, -40 to 85 degC, Tape and Reel	STM-LQFP64_V	1
U5	LSM9DS1TR	iNEMO Inertial Module: 3D Accelerometer, 3D Gyroscope, 3D Magnetometer, 1.9 to 3.6 V, -40 to 85 degC, 24-Pin LGA, RoHS, Tape and Reel	STM-LGA-24_3500X3000X1000	1
X1	ABS25-32.768KHZ-6-T	Low Frequency Crystal, 32.768 KHz, 6 pF, +/- 20 ppm, -40 to 85 degC, 4-Pin SMD, RoHS, Tape and Reel	ABRA-ABS25-4_V	1



# Technical Checklist

## C.1 General Safety Measures

Description	Status		
	OK	NOT OK	N/A
<p><b>No exposure to harmful substances/materials?</b> No materials that might cause allergies are in contact with the pilot. The skin electrodes are already tested with our pilot and they don't create discomfort.</p>	✓		
<p><b>Emergency stops can be identified and reached easily?</b> The RehaMove3 is attached to the belt that surrounds the pilot's hip, and therefore of easy access. The electrodes' cables can be quickly detached either by the pilot or by the experimenter. Moreover, the power-off buttons of both the stimulator and the portable processor are easily accessible to both the team and the pilot.</p>	✓		
<p><b>No loose wires and cables?</b> The cables are properly arranged so that they cannot represent a hazard for the pilot.</p>	✓		
<p><b>Moving/rotating components cannot be touched?</b> No moving or rotating components are present.</p>	✓		
<p><b>No potential snag hazards?</b> There are no components that could potentially become a snag hazard.</p>	✓		
<p><b>No risks arising from excessive noise emitted?</b> No noise is emitted from the device during operation.</p>	✓		
<p><b>Peripheral components cannot be lost?</b> No components can be lost during operation if they have been properly attached before the starting of the experiment.</p>	✓		
<p><b>Safety equipment does not impose any restrictions?</b> No safety equipment such as helmet is not needed and, therefore, does not restrict the user during operation.</p>	✓		
<p><b>Is it safe to touch/interfere with the device during operation?</b> The device is built in a way, so that surrounding safety personal can safely interfere and touch the device in case of emergency. Touching or interfering with the device do not cause a dangerous state.</p>	✓		

## C.2 Requirements Related to Energy Storage and Electric Components

Description	Status		
	OK	NOT OK	N/A
<p><b>Battery state is displayed?</b> Battery state is indicated to avoid deeply discharged batteries or overloaded batteries. In the portable processor, a blue LED signals the device is playing; an orange LED signals the battery is charging and a green LED turn on when the battery is fully charged. Rehamove3 contains its battery and a red led displays the battery status to the operator and the pilot. The status of the external battery that powers the ODROID-C2 is displayed on the battery itself using five LEDs (5 fully charged – 0 empty charge).</p>	✓		
<p><b>Batteries are stored securely?</b> Batteries are properly secured, cannot move in their casing and are protected from potential impacts and collisions.</p>	✓		
<p><b>Batteries do not touch the pilot?</b> Battery casing is not in direct contact with the pilot or any other person.</p>	✓		
<p><b>Live battery terminals cannot be touched?</b> Contact with live battery terminals is not possible.</p>	✓		
<p><b>Electric components are covered/insulated sufficiently?</b> All electric components are covered/insulated so that electric shocks or burnings are avoided (harmful contact with high electrical energy sources and live components).</p>	✓		
<p><b>Energy sources can be identified easily?</b> All hazardous energy sources are clearly identified/labelled, and the isolators are firmly connected, and thus are not removable.</p>	✓		
<p><b>Heat dissipating components cannot be touched?</b> Heat dissipating components are not in contact with the pilot.</p>	✓		
<p><b>Splash water protection is implemented?</b> Splashing water/ spray water cannot lead to an unsafe device state in any case.</p>	✓		



### C.3 Requirements Related to Start-up and Shut-down

Description	Status		
	OK	NOT OK	N/A
<b>Power failure does not cause a potentially dangerous state?</b> Power failure or unintended shutdown and subsequent re-application of power does not lead to unacceptable risk in terms of robot stability. If any of the device stops working, the subject stops receiving the stimulation from RehaMove3 with no negative impact on pilot's safety.	✓		

## C.4 Requirements Related to the Device Shape

Description	Status		
	OK	NOT OK	N/A
<p><b>Stability of the device is guaranteed even if not powered?</b> Stability is guaranteed by the prosthesis manufacturer also in case of internal power discharged. The basic functions of the prosthetic leg are preserved.</p>	✓		
<p><b>Collisions do not cause an unsafe state of the device?</b> Safety-related objects are protected from hazardous movements after or during a collision; collision cannot cause instability of the system. The hard-plastic covers of all the components protect the technology from collisions.</p>	✓		
<p><b>Mounting/attachment equipment is ergonomic?</b> Straps and any mounting/attachment equipment are designed not to cause injuries, e.g. cutting or abrasion.</p>	✓		
<p><b>No sharp edges and points?</b> Sharp edges and points are avoided; in the design of the device, all angles have been smoothed out.</p>	✓		
<p><b>Insertion of any part of the human body is prevented?</b> No holes or gaps in the accessible part of the robot allow the insertion of any part of the human body.</p>	✓		
<p><b>Moving parts and detachments do not cause injuries?</b> No moving parts are present. Detachment of any part does not cause any injury.</p>	✓		
<p><b>The device's design is ergonomic?</b> The device is small in size and light so it does not cause any posture or usage hazards during operation.</p>	✓		
<p><b>The field of view is not limited?</b> The device does not limit the field of view or visibility of the pilot during operation.</p>	✓		

# Risk analysis

---

The current section illustrates specific risks the patient could be subject to in case of failure of any of the parts that constitute the device, their detection rate and all possible preventing measures to remove or minimize the possibility of injury.

The first important thing to notice is that a sudden shut down of the system does not cause any kind of injury to the patient; the stimulator RehaMove3 stops providing the stimulation to the subject that will, therefore, continue walking at his own natural gait without the sensory feedback. In case of an improper functioning of the electronic board and/or ODROID-C2 (e.g. erroneous acquisition of force or knee angle), the stimulation provided to the patient will never overcome a maximum threshold that is patient-dependent and is appropriately chosen before the start of the experiment as a stimulation that is well perceived by the subject but not painful at all.

S: Severity, O: Occurrence, D: Detection, RPN: Risk Priority Number.

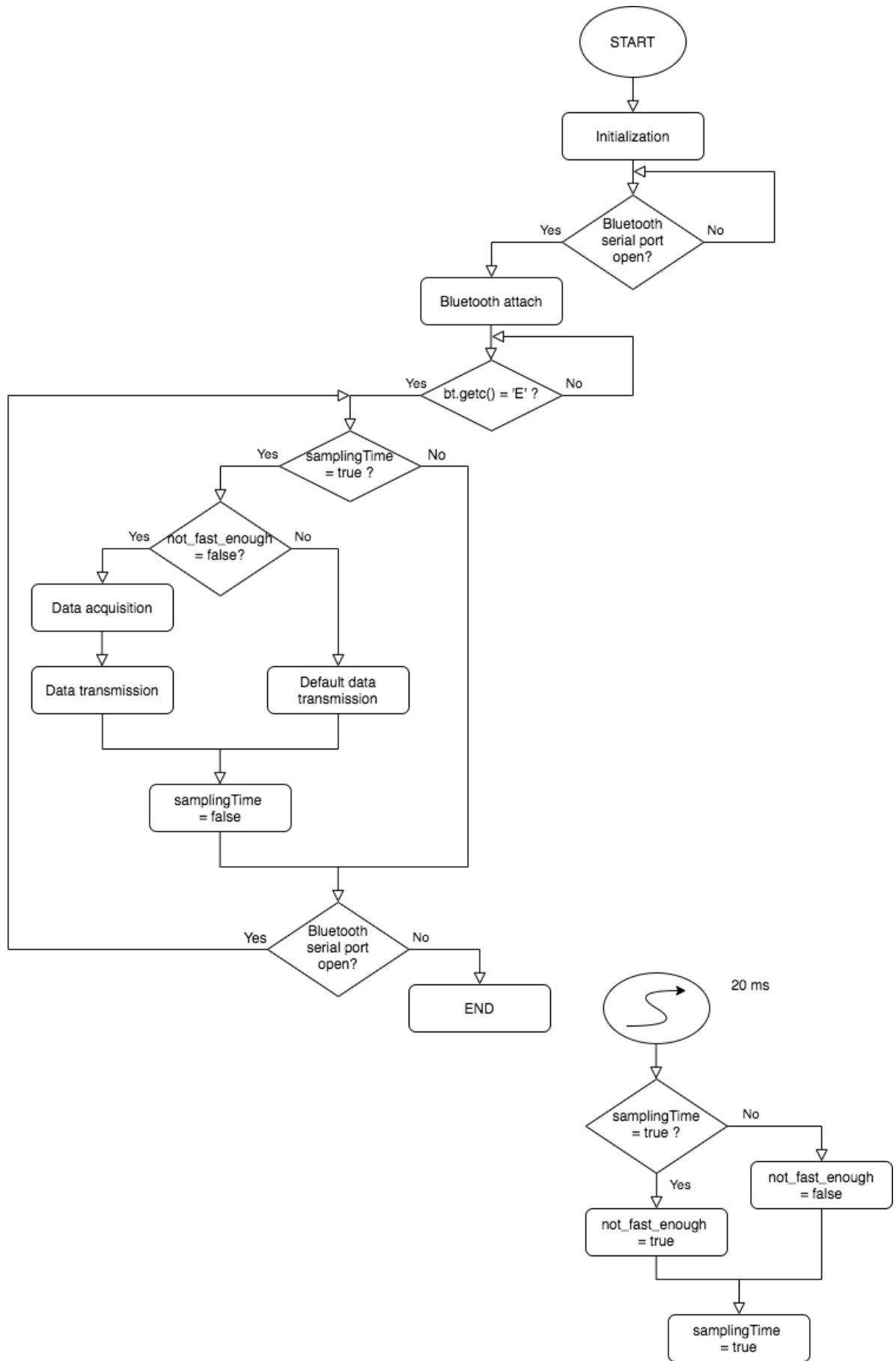
Assembly	Failure & Effect	S1	O1	D1	RPN before	Preventing measures	S2	O2	D2	RPN after
ODROID-C2	Getting an electric shock after touching the microcontroller due to shortcut on the board from damage.	2	3	2	12	Provide cover for the microcontroller, so that components cannot be touched. The cover should never be opened and, moreover, it is easily detectable if the subject tries to.	2	2	1	4
	CPU gets too hot and safety mechanism of ODROID-C2 does not work, causing the system to burn the pilot.	3	1	2	6	Mount the ODROID-C2 on a reasonable location where enough air flow is given, not overheating the system, and where is not in direct contact with the pilot.	2	1	2	4
	ODROID-C2 shuts down due to the disconnection of the USB cable that connects it to the external powerbank.	3	2	2	12	ODROID-C2 and the external powerbank are placed in a fanny bag and the cable are carefully folded inside it so to minimize the movements and the possibility to manually detach the cable.	2	1	2	4
Electronic board	Getting an electric shock after touching the microcontroller due to shortcut on the board from damage.	2	3	2	12	Provide cover for the PCB, so that components cannot be touched. The cover should never be opened and, moreover, it is easily detectable if the subject tries to.	2	2	1	4
	The PCB gets too hot, causing the system to stop working properly.	3	2	2	12	Place the circuit inside a perforated box that guarantees enough air flow, avoiding overheating the system, or cover the box with a material that allows heat dissipation.	3	1	2	6

Assembly	Failure & Effect	S1	O1	D1	RPN before	Preventing measures	S2	O2	D2	RPN after
	The splash/spray water could damage the circuits inside the box.	3	2	2	12	A silicon layer is placed inside the box to protect the electronics by the spray/splash water.	3	1	2	6
	The PCB stops working properly due to excessive vibration or movement.	2	3	2	12	The PCB is mounted on a plastic box that perfectly fits its dimensions and it is fixed with screws reducing the possibility of movements.	2	1	2	4
	The PCB components get damaged after a shock or a strong collision with an external obstacle while walking.	2	3	2	12	The internal components are placed inside a rigid plastic box to protect from any type of collision.	2	1	2	4
	The power-on LED stops working not signaling the status of the circuit.	2	2	2	8	An additional LED is connected to the microcontroller and blinks during the operation of the device to signal its correct functioning.	1	2	1	2
Sensorized insole	The sensors are not properly placed over the foot sole and the acquired force does not reflect the pressure distribution under the foot.	1	2	3	6	The insole replicates the exact shape of the shoe and different insole size are available to better fit the shoe of the participant and keep the sensors in the correct and fixed location.	1	1	2	2
RehaMove 3	Overheating because of lack of ventilation can cause fire, hurting the pilot with severe burns and/or permanent damages.	3	2	2	12	Mount the RehaMove 3 on a reasonable location where enough air flow is given, not overheating the system, and not in direct contact with the pilot.	3	1	2	6
	Hardware gets too hot and safety mechanism of RehaMove 3 does not work, causing the system to burn the pilot.	3	2	2	12	Mount the RehaMove 3 on a reasonable location where enough air flow is given,	3	1	2	6

Assembly	Failure & Effect	S1	O1	D1	RPN before	Preventing measures	S2	O2	D2	RPN after
						not overheating the system, and not in direct contact with the pilot.				
	The amplitude stimulation might be too high and lead to minor psychological damage due to pain.	2	2	3	12	The system has a forced limit on the maximum current for the stimuli (hardcoded), which is well below the maximum acceptance level from the pilot, and each command has a checksum code that prevents possible errors due to interference.	2	1	3	6
	The surface electrodes are detaching from the skin.	3	2	2	12	The electrodes are fixed to the skin using medical tape and placed under a silicon liner that presses the electrodes on the skin separating them from the prosthetic leg.	2	1	2	4
	The electrodes are not sterile causing the spread of infections.	3	2	2	12	Use new electrodes for each patient and apply electrode only to unbroken skin.	1	2	2	4
Batteries	Overheating causes the burning of the pilot.	3	2	1	6	The lithium battery has a protective circuit that avoids fire and explosion.	3	1	1	3
	Leaks, setting battery acid free, burning the skin of the pilot.	3	2	2	12	Place battery where it cannot be damaged mechanically, preventing damage of battery, covered and not in direct contact with the pilot.	2	1	2	4

# Firmware flowchart

---





---

# Bibliography

---

- [1] F. M. Petrini, M. Bumbasirevic, G. Valle, V. Ilic, P. Mijović, P. Čvančara, F. Barberi, N. Katic, D. Bortolotti, D. Andreu, *et al.*, “Sensory feedback restoration in leg amputees improves walking speed, metabolic cost and phantom pain,” *Nature medicine*, vol. 25, no. 9, pp. 1356–1363, 2019.
- [2] V. Aboyans, J.-B. Ricco, M.-L. E. Bartelink, M. Björck, M. Brodmann, T. Cohnert, J.-P. Collet, M. Czerny, M. De Carlo, S. Debus, *et al.*, “2017 esc guidelines on the diagnosis and treatment of peripheral arterial diseases, in collaboration with the european society for vascular surgery (esvs) document covering atherosclerotic disease of extracranial carotid and vertebral, mesenteric, renal, upper and lower extremity arteries endorsed by: the european stroke organization (eso) the task force for the diagnosis and treatment of peripheral arterial diseases of the european society of cardiology (esc) and of the european society for vascular surgery (esvs),” *European heart journal*, vol. 39, no. 9, pp. 763–816, 2018.
- [3] K. Ziegler-Graham, E. J. MacKenzie, P. L. Ephraim, T. G. Travison, and R. Brookmeyer, “Estimating the prevalence of limb loss in the united states: 2005 to 2050,” *Archives of physical medicine and rehabilitation*, vol. 89, no. 3, pp. 422–429, 2008.
- [4] L. Nolan, A. Wit, K. Dudziński, A. Lees, M. Lake, and M. Wychowański, “Adjustments in gait symmetry with walking speed in trans-femoral and trans-tibial amputees,” *Gait & posture*, vol. 17, no. 2, pp. 142–151, 2003.
- [5] W. C. Miller, M. Speechley, and B. Deathe, “The prevalence and risk factors of falling

- 
- and fear of falling among lower extremity amputees,” *Archives of physical medicine and rehabilitation*, vol. 82, no. 8, pp. 1031–1037, 2001.
- [6] H. Flor, L. Nikolajsen, and T. S. Jensen, “Phantom limb pain: a case of maladaptive cns plasticity?,” *Nature reviews neuroscience*, vol. 7, no. 11, pp. 873–881, 2006.
- [7] J. Naschitz and R. Lenger, “Why traumatic leg amputees are at increased risk for cardiovascular diseases,” *QJM: An International Journal of Medicine*, vol. 101, no. 4, pp. 251–259, 2008.
- [8] C. Gauthier-Gagnon, M.-C. Grisé, and D. Potvin, “Enabling factors related to prosthetic use by people with transtibial and transfemoral amputation,” *Archives of physical medicine and rehabilitation*, vol. 80, no. 6, pp. 706–713, 1999.
- [9] R. Waters, J. Perry, D. Antonelli, and H. Hislop, “Energy cost of walking of amputees: the influence of level of amputation,” *J Bone Joint Surg Am*, vol. 58, no. 1, pp. 42–46, 1976.
- [10] B. T. Rodrigues, V. N. Vangaveti, and U. H. Malabu, “Prevalence and risk factors for diabetic lower limb amputation: a clinic-based case control study,” *Journal of diabetes research*, vol. 2016, 2016.
- [11] M. Hakim, N. Kurniani, R. Pinzon, D. Tugasworo, B. M, H. H, P. P, A. Fithrie, and W. AD, “A review on prevalence and causes of peripheral neuropathy and treatment of different etiologic subgroups with neurotropic b vitamins,” vol. 9, 01 2019.
- [12] A. Pfannkuche, A. Alhajjar, A. Ming, I. Walter, C. Piehler, and P. R. Mertens, “Prevalence and risk factors of diabetic peripheral neuropathy in a diabetics cohort: Register initiative “diabetes and nerves”,” *Endocrine and Metabolic Science*, vol. 1, no. 1-2, p. 100053, 2020.
- [13] A. Gordois, P. Scuffham, A. Shearer, A. Oglesby, and J. A. Tobian, “The health care costs of diabetic peripheral neuropathy in the us,” *Diabetes care*, vol. 26, no. 6, pp. 1790–1795, 2003.
- [14] A. Raghav, Z. A. Khan, R. K. Labala, J. Ahmad, S. Noor, and B. K. Mishra, “Financial burden of diabetic foot ulcers to world: a progressive topic to discuss always,” *Therapeutic advances in endocrinology and metabolism*, vol. 9, no. 1, pp. 29–31, 2018.

- 
- [15] E. J. MacKenzie, R. C. Castillo, A. S. Jones, M. J. Bosse, J. F. Kellam, A. N. Pollak, L. X. Webb, M. F. Swiontkowski, D. G. Smith, R. W. Sanders, *et al.*, “Health-care costs associated with amputation or reconstruction of a limb-threatening injury,” *JBJS*, vol. 89, no. 8, pp. 1685–1692, 2007.
- [16] M. Windrich, M. Grimmer, O. Christ, S. Rinderknecht, and P. Beckerle, “Active lower limb prosthetics: a systematic review of design issues and solutions,” *Biomedical engineering online*, vol. 15, no. 3, p. 140, 2016.
- [17] L. J. Hargrove, A. J. Young, A. M. Simon, N. P. Fey, R. D. Lipschutz, S. B. Finucane, E. G. Halsne, K. A. Ingraham, and T. A. Kuiken, “Intuitive control of a powered prosthetic leg during ambulation: a randomized clinical trial,” *Jama*, vol. 313, no. 22, pp. 2244–2252, 2015.
- [18] F. M. Petrini, G. Valle, M. Bumbasirevic, F. Barberi, D. Bortolotti, P. Cvancara, A. Hiairassary, P. Mijovic, A. Ö. Sverrisson, A. Pedrocchi, *et al.*, “Enhancing functional abilities and cognitive integration of the lower limb prosthesis,” *Science translational medicine*, vol. 11, no. 512, p. eaav8939, 2019.
- [19] T. R. Clites, M. J. Carty, J. B. Ullauri, M. E. Carney, L. M. Mooney, J.-F. Duval, S. S. Srinivasan, and H. M. Herr, “Proprioception from a neurally controlled lower-extremity prosthesis,” *Science Translational Medicine*, vol. 10, no. 443, p. eaap8373, 2018.
- [20] B. Chen, Y. Feng, and Q. Wang, “Combining vibrotactile feedback with volitional myoelectric control for robotic transtibial prostheses,” *Frontiers in Neurorobotics*, vol. 10, p. 8, 2016.
- [21] D. Rusaw, K. Hagberg, L. Nolan, and N. Ramstrand, “Can vibratory feedback be used to improve postural stability in persons with transtibial limb loss?,” *Journal of rehabilitation research and development*, vol. 49, no. 8, pp. 1239–1254, 2012.
- [22] C. Dietrich, S. Nehrdich, S. Seifert, K. R. Blume, W. H. Miltner, G. O. Hofmann, and T. Weiss, “Leg prosthesis with somatosensory feedback reduces phantom limb pain and increases functionality,” *Frontiers in neurology*, vol. 9, p. 270, 2018.
- [23] T. R. Dillingham, L. E. Pezzin, and A. D. Shore, “Reamputation, mortality, and health care costs among persons with dysvascular lower-limb amputations,” *Archives of physical medicine and rehabilitation*, vol. 86, no. 3, pp. 480–486, 2005.

- 
- [24] C.-A. Behrendt, B. Sigvant, Z. Szeberin, B. Beiles, N. Eldrup, I. A. Thomson, M. Venermo, M. Altreuther, G. Menyhei, J. Nordanstig, *et al.*, “International variations in amputation practice: a vascunet report,” *European Journal of Vascular and Endovascular Surgery*, vol. 56, no. 3, pp. 391–399, 2018.
- [25] Y. Kim, C. Park, D. Kim, T. Kim, and J. Shin, “Statistical analysis of amputations and trends in korea,” *Prosthetics and orthotics international*, vol. 20, no. 2, pp. 88–95, 1996.
- [26] D. C. Morgenroth, A. C. Gellhorn, and P. Suri, “Osteoarthritis in the disabled population: a mechanical perspective,” *PM&R*, vol. 4, no. 5, pp. S20–S27, 2012.
- [27] R. M. Williams, A. P. Turner, M. Orendurff, A. D. Segal, G. K. Klute, J. Pecoraro, and J. Czerniecki, “Does having a computerized prosthetic knee influence cognitive performance during amputee walking?,” *Archives of physical medicine and rehabilitation*, vol. 87, no. 7, pp. 989–994, 2006.
- [28] C. E. Roffman, J. Buchanan, and G. T. Allison, “Predictors of non-use of prostheses by people with lower limb amputation after discharge from rehabilitation: development and validation of clinical prediction rules,” *Journal of physiotherapy*, vol. 60, no. 4, pp. 224–231, 2014.
- [29] B. Christensen, B. Ellegaard, U. Bretler, and E. Østrup, “The effect of prosthetic rehabilitation in lower limb amputees,” *Prosthetics and Orthotics International*, vol. 19, no. 1, pp. 46–52, 1995.
- [30] A. Houghton, A. Allen, R. Luff, and I. McColl, “Rehabilitation after lower limb amputation: A comparative study of above-knee, through-knee and gritti—stokes amputations,” *British journal of surgery*, vol. 76, no. 6, pp. 622–624, 1989.
- [31] B. C. Callaghan, R. S. Price, and E. L. Feldman, “Distal symmetric polyneuropathy: a review,” *Jama*, vol. 314, no. 20, pp. 2172–2181, 2015.
- [32] M. CLINIC, “Peripheral neuropathy.”
- [33] T. Julian, N. Glasgow, R. Syeed, and P. Zis, “Alcohol-related peripheral neuropathy: a systematic review and meta-analysis,” *Journal of Neurology*, vol. 266, no. 12, pp. 2907–2919, 2019.

- 
- [34] U. Alam, D. R. Riley, R. S. Jugdey, S. Azmi, S. Rajbhandari, K. D’Août, and R. A. Malik, “Diabetic neuropathy and gait: a review,” *Diabetes therapy*, vol. 8, no. 6, pp. 1253–1264, 2017.
- [35] P. Lalli, A. Chan, A. Garven, N. Midha, C. Chan, S. Brady, E. Block, B. Hu, and C. Toth, “Increased gait variability in diabetes mellitus patients with neuropathic pain,” *Journal of Diabetes and its Complications*, vol. 27, no. 3, pp. 248–254, 2013.
- [36] A. I. Faisal, *Development of a Low-Cost and Easy-to-Use Wearable Knee Joint Monitoring System*. PhD thesis, 2020.
- [37] T. Seel, J. Raisch, and T. Schauer, “Imu-based joint angle measurement for gait analysis,” *Sensors*, vol. 14, no. 4, pp. 6891–6909, 2014.
- [38] F. Feldhege, A. Mau-Moeller, T. Lindner, A. Hein, A. Marksches, U. K. Zettl, and R. Bader, “Accuracy of a custom physical activity and knee angle measurement sensor system for patients with neuromuscular disorders and gait abnormalities,” *Sensors*, vol. 15, no. 5, pp. 10734–10752, 2015.
- [39] P. Gui, L. Tang, and S. Mukhopadhyay, “Mems based imu for tilting measurement: Comparison of complementary and kalman filter based data fusion,” in *2015 IEEE 10th conference on Industrial Electronics and Applications (ICIEA)*, pp. 2004–2009, IEEE, 2015.
- [40] O. O. Akintade and L. O. Kehinde, “Comparison of data fusion techniques for human knee joint range-of-motion measurement using inertial sensors,” *Int. J. Electron. Electr. Eng*, pp. 127–134, 2017.
- [41] “Nucleo-f103rb user manual,” 2015.
- [42] A. R. Swain and R. Hansdah, “A model for the classification and survey of clock synchronization protocols in wsns,” *Ad Hoc Networks*, vol. 27, pp. 219–241, 2015.
- [43] T. Sheng, K. Jing, L. Zunzun, and D. Pengfei, “Design and implementation of time synchronization experimental system for wireless sensor networks,” *International Journal of Online and Biomedical Engineering (iJOE)*, vol. 14, no. 06, pp. 212–222, 2018.

- 
- [44] R. Casas, H. J. Gracia, A. Marco, and J. L. Falco, "Synchronization in wireless sensor networks using bluetooth," in *Third International Workshop on Intelligent Solutions in Embedded Systems, 2005.*, pp. 79–88, IEEE, 2005.
- [45] H. Andersen, S. Nielsen, C. E. Mogensen, and J. Jakobsen, "Muscle strength in type 2 diabetes," *Diabetes*, vol. 53, no. 6, pp. 1543–1548, 2004.
- [46] C. Giacomozzi, E. D'Ambrogi, S. Cesinaro, V. Macellari, and L. Uccioli, "Muscle performance and ankle joint mobility in long-term patients with diabetes," *BMC musculoskeletal disorders*, vol. 9, no. 1, p. 99, 2008.
- [47] R. W. M. Van Deursen and G. G. Simoneau, "Foot and ankle sensory neuropathy, proprioception, and postural stability," *Journal of orthopaedic & sports physical therapy*, vol. 29, no. 12, pp. 718–726, 1999.
- [48] J. Park, Y. Na, G. Gu, and J. Kim, "Flexible insole ground reaction force measurement shoes for jumping and running," *2016 6th IEEE International Conference on Biomedical Robotics and Biomechatronics (BioRob)*, pp. 1062–1067, 2016.